Stoner magnetism and Berry phase in quantum materials

by

Zhiyu Dong

B.S., Fudan University (2018)

Submitted to the Department of Physics
in partial fulfillment of the requirements for the degree of

Doctor of Philosophy

at the

MASSACHUSETTS INSTITUTE OF TECHNOLOGY

June 2023

Author .....
Department of Physics
May 19, 2023

Certified by .....
Leonid Levitov
Professor of Physics
Thesis Supervisor

Accepted by .....
Lindley Winslow
Associate Department Head of Physics

Stoner magnetism and Berry phase in quantum materials

by

Zhiyu Dong

Submitted to the Department of Physics
on May 19, 2023, in partial fulfillment of the
requirements for the degree of
Doctor of Philosophy

Abstract

Two-dimensional solids often exhibit carrier bands with Berry phase in k space, resulting in carriers behaving like spinning objects and generating orbital magnetization in position space. This thesis explores the impact of orbital magnetization arising in this way on the correlated electron phases. The effect of Berry phase is particularly interesting for magnetic phases with spin and valley polarization originating from Stoner instability, such as those seen in moiré graphene and other narrow-band systems. Despite recent advances in the field, these questions remain largely unexplored, and this thesis aims to address this gap in research. Interesting physics arises due to an interplay between two distinct effects: geometric phases in k space due to band Berry curvature and geometric phases in position space arising for spin-polarized carriers traversing a spin texture. This results in an interaction that we term the "chiral interaction," a form of an emergent spin-orbital interaction that arises solely from electron exchange, in the absence of microscopic spin-orbit couplings. The chiral interaction, in contrast to microscopic spin-orbit coupling, respects the SU(2) spin rotation symmetry and exhibits other interesting characteristics. In this thesis, we establish the existence of this interaction through a general symmetry argument and microscopic calculations, and investigate its consequences. Specifically, we explore the emergence of chiral edges that support spin excitations propagating without back-scattering and the occurrence of skyrmions, the topologically protected particle-like objects stabilized by the chiral interaction in the ground state of the system.

Thesis Supervisor: Leonid Levitov
Title: Professor of Physics

Acknowledgments

First and foremost, I owe a debt of immense gratitude to my advisor, Leonid Levitov, for his invaluable guidance and support over the past five years. I consider it an honor and a privilege to have learned physics from him. I benefit and learned a lot from his thought-provoking questions and unique angles of thinking. I am extremely grateful for his encouragement and patience throughout our discussions, which have helped me overcome many obstacles, and for his generous devotion of time and effort, especially during the pandemic. Without his guidance and mentorship, I would not have been able to complete this journey. Thank you, Leonid.

I want to thank Patrick A. Lee and Andrey Chubukov for their advice and collaboration on various projects. Working with them has been a true delight, and I like our papers very much, even though they are not included in this thesis. I am sincerely grateful for their patience which has allowed me to learn a lot from our discussions. I thank Patrick for serving as a member of my thesis defense committee. Furthermore, I want to take this opportunity to express my deepest appreciation to both Patrick and Andrey for their support in my job application process.

I also thank the experimentalists who have greatly benefited my work. Special thanks go to Eli Zeldov, Matan Borcarsly, Raymond Ashoori, Andrea Young, Thomas Weitz, and Anna Seiler for insightful discussions. I especially appreciate Eli and Matan for sharing and discussing unpublished data, which inspired some of the work presented in this thesis. I would like to thank Ray for enlightening discussions and for being a member of my thesis committee.

I am grateful to many friends who helped me during my time at MIT. Thank you to Cyprian Lewandowski for his encouragement and for generously sharing his experience which saved me from many detours in my journey. Thank you to Ali Fahimniya for working together on my first project. Thank you to Margarita Davydova and Olumakinde Ogunnaike for working together on the projects presented in Chapter 2 and 4 of this Thesis. I also thank other friends in Condensed Matter Theory and Condensed Matter Experiment groups, Adarsh S. Patri, Achisman Panigrahi,

Ali Ghorashi, Ethan Lake, Seth Musser, Taige Wang, Tonghang Han, Zhengyan Darius Shi, and especially my office mates Robert Jones and Changnan Peng for their friendship, kindness and helpful discussions.

I am indebted to Catherine Modica and Sydney Miller from the Academic Programs Office for the kindness and the assistance they offered whenever I needed it.

I am grateful for the support of the people who have been an important part of my journey before my PhD study, especially Si-Tong Guan, Jun Hong, and Mei-Fang Wang, who initiated me into physics. I thank them for their immense care during my high school years. I would also like to express my sincere gratitude to Gang Chen and Yan Chen, my undergraduate advisors at Fudan University, for providing me with research training and supporting me in my academic pursuits. Without their guidance and mentorship, my journey in physics would not have been possible.

I thank my parents for their support in my pursuit of physics, and for providing me with all kinds of resources, both moral and practical. Thank you to my brother, Zhihuan Dong, for his support and insightful discussions, both physical and non-physical. And, thank you to my grandparents for their love.

I am immensely grateful for the moral support from my heroes — those brave individuals who sacrificed their lives to protect my country in the war almost a century ago. Their dedication, perseverance, and commitment, even in the face of unimaginable hardship and despair, continue to serve as a timeless inspiration for me. They remain a constant reminder of the strength and resilience that reside within us, empowering me to confront challenges head-on.

Lastly, I thank the Spirit of Physics for a guiding role in my life. Despite some pains and struggles, physics has always been a source of constant inspiration, wonder and delight. I sincerely hope that this pattern is set to continue.

Cambridge, Massachusetts

May 17, 2023

Contents

Chapter 1

Introduction

1.1 Overview

Stoner instability [165, 166, 167], explains ferromagnetism in itinerant electron systems through exchange interaction between band electrons that originatinges from fermion exclusion. The instability arises when the exchange interaction exceeds the carrier kinetic energy set by the conduction band dispersion and the carrier density. Stoner magnetism is a broad framework that, over the years, has been applied to a variety of different systems[32]. Unlike other forms of magnetism, Stoner magnetism occurs in a Fermi sea. As a result, it is uniquely sensitive to the details of the conduction band and is tunable by carrier doping [32].

Recently a new class of materials was introduced, known as "quantum materials", which are a few atomic layers thin and host strongly interacting electrons [57]. The recent addition to this family is twisted bilayers graphene [3], a system in which band dispersion can be flattened to the point of kinetic energy becoming negligible compared to the interaction energy. This favors Stoner magnetism, yielding a a variety of magnetic phases that feature valley and spin polarization of different kinds[202, 203, 201, 35, 150].

A salient feature of quantum materials is Berry phase in k space[187], a quantity that describes the geometry of the bands and can be present in bands with non-trivial topology as well as in topologically trivial bands that are lacking inversion

symmetry or time-reversal symmetry. While the Berry phase is ubiquitous in quantum materials, so far its role in Stoner physics escaped the attention of researchers in the field. This motivates us to ask whether the Stoner magnetism is altered or enriched if a conduction band is equipped with Berry curvature. Specifically, can Berry curvature give rise to new interactions and generate new orders and new types of low-energy excitations in Stoner magnets? These questions, besides being of fundamental interest for many-body theory, are further motivated by recent developments in two-dimensional materials that allow engineering the band dispersion and tuning the Berry curvature[202, 203, 201, 35, 150].

In this thesis, we will answer these questions in the affirmative. We will demonstrate that the Berry curvature of the electron bands gives rise to a new chiral interaction in Stoner-polarized bands, which couples the orbital and spin degrees of freedom. This interaction can be viewed as an exotic form of spin-orbit interaction that arises in Stoner bands equipped with Berry phase in the absence of a microscopic spin-orbital interaction and can lead to a number of interesting effects. This thesis establishes the chiral interactions microscopically as well as on general symmetry grounds and explores their implications. In particular, it predicts that the chiral interaction gives rise to unusual skyrmion ground states and leads to exotic excitations—spin waves that propagate unidirectionally along the edge.

To provide context for the discussion, we will begin by reviewing Stoner magnetism in Section 1.2. We will describe the development of the theory of itinerant ferromagnetism and introduce the conventional theoretical framework that explains this physics. In Section 1.3, we will review the concept of the Berry phase and discuss its properties in position and momentum space. Finally, in Sec. 1.4, we will introduce multilayer graphene, a family of materials that host bands with non-zero Berry curvature and exhibit Stoner magnetism. We will discuss their fundamental properties and review recent experiments that observe Stoner magnetism in these systems. This will set the stage for the discussion in the main part of the thesis.

1.2 Stoner magnetism without Berry curvature

This section provides an overview of Stoner magnetism, starting with a brief review of the theory of itinerant magnetism in Sec. 1.2.1, drawing from various sources such as Refs. [179, 69, 2, 32]. Following this, we will proceed to review the mean-field framework that describes Stoner magnetism in Sec. 1.2.2. Throughout these discussions, we temporarily neglect the impact of Berry curvature. However, in chapter3, we will utilize this framework to analyze Stoner magnetism in bands endowed with Berry curvature.

1.2.1 A historical overview

The origin of ferromagnetism, a phenomenon familiar from every-day experience with materials such as iron, cobalt, or nickel, puzzled people for quite some time. Despite being known for ages, it was understood only after quantum theory came on stage. It was not until 1906 that Pierre Weiss observed magnetic domains when examining ferromagnets on a microscopic scale. This discovery led him to propose the first mean-field theory, which introduced the concept of a molecular contribution to the effective internal magnetic field[181, 182]:

$$H = H_0 + \Delta\sigma_z \tag{1.1}$$

where H_0 is the noninteracting Hamiltonian, Δ is the Weiss field. However, the origin of the Weiss field has not been understood at the time. Moreover, classical mechanics failed to explain spontaneous magnetism due to the Bohr-van Leeuwen theorem, independently proven by Niels Bohr and Hendrika van Leeuwen [18, 177]. This theorem showed that classical electrons without spin at thermal equilibrium would have zero magnetization, even in a magnetic field [178]. The main argument can be summarized as follows[32]: the magnetic field couples to charges through the Peierls substitution $p \to p + eA(x)$, but because a classical system lacks a non-commutation relation between x and p, such substitution amounts to a local shift of

p, and therefore does not impact the partition function.

A comprehensive understanding of magnetism came with the development of quantum theory. Edmund Stoner and John Slater's contributions in the 1930s paved the way for the theory of itinerant ferromagnetism in metals, which is now referred to as Stoner magnetism [165, 166, 167, 159]. This theory explains itinerant magnetism by competition between the kinetic energy of itinerant electrons and their exchange interactions. Specifically, the kinetic energy favors equal occupation of spin-up and spin-down states, tending to suppress ferromagnetism. In contrast, spin-independent electron-electron repulsion gives rise to an exchange interaction due to fermionic quantum statistics and results in a spontaneously spin-polarized Fermi sea.

In essence, the physical picture of Stoner magnetism is in many ways similar to that of Hund's rule in atomic physics, which predicts that electrons in an atom, when filling the shell with a fixed angular momentum, preferentially occupy different orbitals with the same spin rather than occupying the same orbital with opposite spins. Both Stoner magnetism and Hund's rule arise from the exchange interaction between electrons, which favors the alignment of electrons' spins.

1.2.2 Mean-field framework for Stoner magnetism

This section provides an overview of the mean-field approach for describing Stoner magnetism. Specifically, we will primarily focus on the derivation of the Stoner criterion[32, 2], the threshold for Stoner instability, within this framework. The following discussion serves as a crucial preparation for our analysis in Chapter 3. In that chapter, we will expand upon this framework to study the central question of our interest: Stoner magnetism in bands that possess Berry curvature.

To begin, we consider a metal in which carriers interact through a short-range interactions:

$$H = \sum_{k} \epsilon_k \psi^{\dagger}_{\alpha,k} \psi_{\alpha,k} + \frac{U}{2} \sum_{kk'q} \psi^{\dagger}_{\alpha,k} \psi^{\dagger}_{\beta,k'} \psi_{\beta,k'+q} \psi_{\alpha,k-q} \tag{1.2}$$

where α, β are spin indices, taking values $\uparrow$ or $\downarrow$. Here ϵ_k is the band dispersion. Here and below, unless stated otherwise, repeated indices are summed over. To describe

ordering we decouple the quartic term by introducing an auxiliary field $O_{\alpha\beta}$. After carrying out a Hubbard-Stratonovich transform[2] our problem becomes:

$$-\frac{U}{2}\sum_{kk'q}\bar{\psi}_{\alpha,k}\psi_{\beta,k-q}\bar{\psi}_{\beta,k'}\psi_{\alpha,k'+q} \rightarrow -\sum_{k,q}O_{\alpha\beta}(q)\bar{\psi}_{\beta,k+q}\psi_{\alpha,k}+\sum_{q}\frac{|O_{\alpha\beta}(q)|^2}{2U} \tag{1.3}$$

where the matrix $O_{\alpha\beta}$ has a nonzero expectation value describing order. As a result, the partition function is given by

$$\begin{aligned} Z &= \int \mathcal{D}O\mathcal{D}\bar{\psi}\mathcal{D}\psi e^{-S}, \\ S &= \int d\tau \sum_{k}\bar{\psi}_{\alpha,k}(\partial_\tau+\epsilon_k)\psi_{\alpha,k}-\sum_{k,q}O_{\alpha\beta}(q)\bar{\psi}_{\beta,k}\psi_{\alpha,k+q}+\sum_{q}\frac{|O_{\alpha\beta}(q)|^2}{2U} \end{aligned} \tag{1.4}$$

To investigate the instability towards spatially-uniform spin-polarized order, we focus only on the $q=0$ harmonic and neglect all finite-q contributions, e.g. such as those responsible for the spin-density wave order. Furthermore, the SU(2) spin rotation symmetry allows us to choose $O_{\alpha\beta}(0)=\Delta\sigma_{z,\alpha\beta}$ without loss of generality, which corresponds to a uniform spin polarization along the z direction. By using the expression $F=-T\ln Z$, we obtain:

$$F=\sum_{k}\sum_{\pm}(\tilde{\epsilon}_k\pm\Delta)f(\tilde{\epsilon}_k\pm\Delta)+\frac{\Delta^2}{U} \tag{1.5}$$

where tilde denotes energy measured relative to the Fermi level, $\tilde{\epsilon}_k=\epsilon_k-\mu$. Accordingly, $f(\tilde{\epsilon})$ is the Fermi-Dirac distribution function, $f(\tilde{\epsilon})=1$ for $\tilde{\epsilon}<0$, $f(\tilde{\epsilon})=0$ for $\tilde{\epsilon}\geq 0$. The instability of the spin-unpolarized state towards a spin-polarized state occurs when

$$\frac{\delta^2 F}{\delta\Delta^2}|_{\Delta=0}<0. \tag{1.6}$$

Plugging Eq.(1.5) into Eq.(1.6) yields the Stoner criterion

$$U\nu_0>1 \tag{1.7}$$

where ν_0 represents the density of states in each spin species at the Fermi level.

The nature of the Stoner phase transition (first-order or second-order) in the mean-field framework is determined by the sign of the quartic term ($O(\Delta^4)$) in the free energy, which depends on the details of the band dispersion. Specifically, when ignoring the change of chemical potential due to the spin polarization, one finds a quartic term coefficient of $-\frac{1}{24}\nu''(0)$, where $\nu''(0)$ is the second-order derivative of the density of states at Fermi level [32]. When accounting for the change of chemical potential, one obtains a quartic term coefficient of $\frac{1}{8}\left(\frac{\nu'(0)^2}{\nu(0)} - \frac{1}{3}\nu''(0)\right)$[5]. For most transition metal ferromagnets, such as iron and cobalt, the quartic term coefficient is positive, and the mean-field framework predicts a second-order phase transition occurring at the Stoner threshold. In contrast, quasi-two-dimensional systems, such as graphene multilayers—a class of materials that will be the primary focus in the following sections and chapters—typically exhibit a negative quartic term coefficient[32]. As a result, Stoner magnetism in these systems emerges before reaching the Stoner threshold defined by Eq. (1.7), manifesting as a first-order phase transition.

1.3 Berry phase: definition, examples, and manifestations

This section reviews the concept of the Berry phase[147], which is an essential element in our study. We will begin by reviewing the origin and definition of the Berry phase in generic systems. Then we will describe two implications: position-space Berry phase and momentum-space Berry phase. These implications play a crucial role our analysis throughout the upcoming chapters, particularly in Chapter 3. In that chapter, we will illustrate how the momentum-space Berry curvature significantly enhances Stoner magnetism, ultimately giving rise to the emergence of a position-space Berry curvature.

The Berry phase[13] is a central concept in quantum mechanics, which describes the change in an eigenstate of a quantum system when it undergoes an adiabatic evolution in the parameter space. Namely, an eigenstate returns to its initial state

after this evolution while accumulating an extra phase factor of $e^{i\gamma_C}$. The phase γ_C is geometric: it depends on the path C the system is taking in the parameter space but not on how fast or how slow the system evolves over that path.

Below we derive the expression of Berry phase following Berry's original paper [13]. Here we keep the discussion generic: we consider a generic quantum system described by Hamiltonian $H(\boldsymbol{R})$, where $\boldsymbol{R}$ is a set of parameters. By taking $\boldsymbol{R} = \boldsymbol{r}$ or $\boldsymbol{R} = \boldsymbol{k}$, the result presented below can be directly translate to the Berry phase in position and momentum space — the two cases of our interest. For example, when applied to position space, as we will elaborate in Sec.1.3.1, it directly gives the Berry phase accumulated by an electron moving along a trajectory $\boldsymbol{r}(t)$ on a Stoner magnet background with a spin texture. Below, we keep using the language of a generic system, and we study the Berry phase gained by a state $|\psi\rangle$ when the system evolves along a path in parameter space $\boldsymbol{R}(t)$. The time evolution of state $|\psi\rangle$ is governed by the Schrodinger equation

$$i\hbar\frac{\partial}{\partial t}|\psi\rangle = H(\boldsymbol{R}(t))|\psi(t)\rangle \tag{1.8}$$

Consider the evolution of a state $|\psi_n\rangle$ which starts at $t = 0$ from the n-th eigenstate $|n\rangle$ which satisfies

$$H|n\rangle = \epsilon_n|n\rangle, \tag{1.9}$$

where ϵ_n represents the energy of state $|n\rangle$. Suppose this state is nondegenerate and evolves adiabatically; then the state at time t will still stay in the n-th eigenstate but acquires a phase factor:

$$|\psi_n(t)\rangle = e^{i\theta(t)+i\gamma(t)}|n(t)\rangle, \quad \theta(t) = -\frac{1}{\hbar}\int_0^t dt'\epsilon_n(t'). \tag{1.10}$$

Here, the first phase factor θ denotes the phase accumulation resulting from the system's dynamics, while the second phase factor, which is of main interest for us, arises solely from the geometry of eigenstates and is insensitive to the particulars of

the dynamics. Plugging Eq.(1.10) into the Schrodinger equation, one finds

$$\frac{d}{dt}|n(t)\rangle + i\dot{\gamma}|n(t)\rangle = 0 \tag{1.11}$$

This immediately yields

$$\gamma(T) = i\int_0^T dt\langle n(t)|\boldsymbol{\partial}_t|n(t)\rangle \tag{1.12}$$

This phase is gauge-dependent for $\boldsymbol{R}(T) \neq \boldsymbol{R}(0)$, since relative phase between $|n(\boldsymbol{R}(t))\rangle$ and $|n(\boldsymbol{R}(0))\rangle$ directly shifts $\gamma(T)$. However, if the system returns to its initial parameter at time T, i.e. $\boldsymbol{R}(T) = \boldsymbol{R}(0)$, then the geometrical phase $\gamma(T)$ becomes gauge invariant. We use subscript C to label the loop in parameter space along which the system evolves from time 0 to time T. Then the gauge-invariant phase γ_C, which is the Berry phase, can be written as an integral along the loop C in parameter space,

$$\gamma_C = \oint_C \mathcal{A}(\boldsymbol{R})d\boldsymbol{R}, \quad \mathcal{A}(\boldsymbol{R}) = i\langle n(\boldsymbol{R})|\boldsymbol{\nabla}_{\boldsymbol{R}}|n(\boldsymbol{R})\rangle \tag{1.13}$$

Here, the vector field $\mathcal{A}(\boldsymbol{R})$ is called the Berry connection. By Stokes' theorem, this loop integral can be rewritten as an integral over a surface enclosed by loop C:

$$\gamma = \int \Omega(\boldsymbol{R})d\boldsymbol{R}, \quad \Omega(k) = i\boldsymbol{\nabla}_{\boldsymbol{R}} \times \langle n(\boldsymbol{R})|\boldsymbol{\nabla}_{\boldsymbol{R}}|n(\boldsymbol{R})\rangle \tag{1.14}$$

The quantity Ω is called Berry curvature. This form demonstrates two basic properties of the Berry phase: first, this phase has the U(1) gauge invariance — it is independent of the choice of phase at each point in the parameter space. Therefore, this phase is physical and observable. Second, this phase is independent of the rate of change of the parameter. Therefore, this phase represents a robust geometrical property of the quantum system and is independent of the details of the system dynamics[187].

In the context of electrons in solids, the Berry phase has two primary origins. One is due to the motion of electrons in position space in the presence of coupling to position-dependent degrees of freedom (in what follows, our primary example will

be a spin texture due to position-dependent magnetic order). The other kind of Berry phase arises from the carrier band and momentum-space geometry of the system. These two Berry phases result in profoundly different physical effects. The position-space Berry phase induces an effective Aharonov-Bohm gauge field that electrons experience when traversing the crystal lattice [125, 122, 53, 171], while the momentum-space Berry phase impacts carrier dynamics in momentum space producing two important effects. The first one is the anomalous Hall effect, a Lorentz-like force resulting from an electric field that acts in momentum space instead of position space. The second effect is the gyration effect, which endows carriers with an orbital magnetization and transforms them into spinning objects [187]. Both the position-space and momentum-space effects are central to our discussion in this thesis. To provide context for our discussion, below we will explore these two examples of Berry phases in some detail.

1.3.1 Berry phase in position space

Next, we proceed to examine the Berry phase acquired by electrons as they move in position space in the presence of a textured spin background. Understanding this particular kind of Berry phase will be crucial for our analysis in Chapter 3.

The evolution of a single spin 1/2 in a time-dependent magnetic field was first analyzed in Berry's original work[13]. A generalization to the problem of spin moving through a position-dependent spin texture has been elaborated and reviewed in Ref.[125, 122, 53, 171]. This body of work describes the generation of an emergent electromagnetic field by a spin texture and the resulting nontrivial observable effects. Below we review this approach and main results.

To start, we consider an electron moving in a textured magnetic background characterized by a slow-varying local spin-polarization unit vector $\boldsymbol{n}(r)$. In this case, the moving electrons talk to the local magnetic texture through local exchange interaction, which is modeled by the following Hamiltonian:

$$H = -J\boldsymbol{n}(r) \cdot \boldsymbol{\sigma} \tag{1.15}$$

where J is the strength of the local exchange interaction, $\boldsymbol{\sigma}$ is the Pauli matrix describing the spin of the moving electron, $\boldsymbol{n}(r)$ is a unit vector describing a spatially dependent spin polarization.

Next, substituting $\boldsymbol{R}(t)$ in Eq.(1.13) with $n(\boldsymbol{r}(t))$, we obtain the Berry connection sensed by an itinerant electron moving along a trajectory $\boldsymbol{r}(t)$. Namely, for an electron in spin-up state, the Berry connection is given by[122, 125, 171, 53]

$$\mathcal{A} = i\langle\uparrow|\boldsymbol{\nabla}|\uparrow\rangle = \frac{1}{2}\cos\theta\nabla\phi \tag{1.16}$$

here, $|\uparrow\rangle = \left(\cos\frac{\theta}{2}e^{-i\phi/2}, \sin\frac{\theta}{2}e^{i\phi/2}\right)^T$, angles θ and ϕ are the polar and azimuthal angles of the spatially dependent spin orientation. The prefactor $1/2$ arises from the angular momentum of spin-up state $m_z = \hbar/2$. Consequently, the Berry phase acquired along a loop is nothing else but one-half of the solid angle wrapped by magnetic field texture $\boldsymbol{n}(r)$ on that loop. In this case, the Berry curvature, which is defined as the area density of the Berry phase, can be expressed through:

$$\Omega = 2\pi C(r), \quad C(r) = \frac{1}{4\pi}\boldsymbol{n}(r)\cdot(\partial_1\boldsymbol{n}(r)\times\partial_2\boldsymbol{n}(r)) \tag{1.17}$$

The quantity C is called spin chirality. This quantity has a clear physical meaning: the spatial integral of it represents how many times the magnetic texture wraps around the Bloch sphere. Therefore, in the periodic-boundary system, $\int dr^2 C(r)$ is quantized.

The Berry phase arising from real-space magnetic texture has a nontrivial impact on the behavior of electrons. For an electron moving inside a magnetic texture, the Berry curvature Ω mimics an emergent electromagnetic field since the latter also generates a geometrical phase for electrons moving in it, which is proportional to the magnetic flux enclosed by the path of electrons. The emergent magnetic field sensed by an itinerant electron is given by

$$B = \frac{\hbar c}{e}\Omega = \frac{\hbar c}{2e}\boldsymbol{n}(r)\cdot(\partial_1\boldsymbol{n}(r)\times\partial_2\boldsymbol{n}(r)) \tag{1.18}$$

Similarly, a time-dependent spin configuration gives rise to an emergent electric field

$$\boldsymbol{E} = -\frac{\partial \mathcal{A}}{\partial t} = -\frac{\hbar}{2e}\boldsymbol{n}(r) \cdot (\partial_t \boldsymbol{n}(r) \times \boldsymbol{\nabla}\boldsymbol{n}(r)) \tag{1.19}$$

The emergent electromagnetic fields generated by Berry phase effect of magnetic textures lead to observable signatures, which have been reported and reviewed in various studies[122, 125, 124]. Below we review these results.

Magnetic systems with non-collinear spin structures are one such example, where the solid angle subtended by spins generates a static emergent magnetic field Eq.(1.18), leading to the Hall effect [168] and [169]. The pyrochlore ferromagnet $NdMo_2O_7$ is a good example of this, as it exhibits a non-coplanar spin structure due to the strong single-spin anisotropy that enforces the rare-earth (Nd) moments to point outward or inward from the center of the tetrahedron (see Fig.1-1), coupled to the itinerant electrons of Mo atoms, as described in Ref.[170]. The itinerant electrons, therefore, experience the emergent magnetic field and exhibit the anomalous Hall effect. The magnetic ordering in this material does not alter the periodicity of the electronic state, and the band structure is well-defined with the original first Brillouin zone.

Another system demonstrating the spin-texture-induced gauge field is the skyrmion crystal discovered in magnets with B20 structure— a non-centrosymmetric cubic crystal structure— such as iron monogermanide (FeGe)[193] and manganese monosilicide (MnSi)[121]. The lack of inversion symmetry in these systems gives rise to a Dzyaloshinsky-Moriya interaction[44, 117] that favors spin textures, including skyrmion crystals. Here, the skyrmion is considered as the mapping from the two-dimensional space to the unit sphere, i.e. the direction of $\boldsymbol{n}$, and it wraps the sphere once, implying that the integral of the magnetic flux over one skyrmion is 2π. The effective magnetic field induced by the skyrmion is then estimated to be $\sim$ 4000T for a skyrmion size of $\xi = 1nm$. This fictitious magnetic field acts on the conduction electrons in MnSi, (Fe, Co)Si, and MnGe, giving rise to the Hall effect due to the Lorentz force, with B replacing the external magnetic field B_0. This scenario [79] is confirmed by recent experiments.

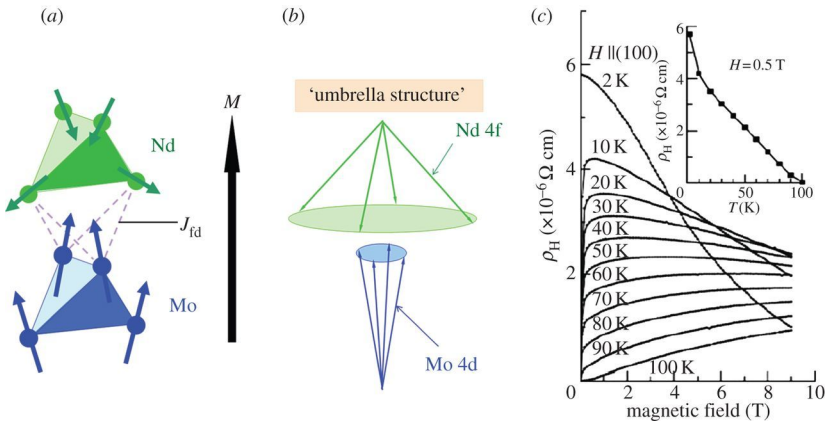

Figure 1-1: Anomalous Hall effect in $Nd_2Mo_2O_7$. FIgure adapted from Refs. [122] and [169]. (a) The atomic structure of $Nd_2Mo_2O_7$ where Nd and Mo atoms are coupled antiferromagnetically through J_{fd}, forming two interpenetrating networks of tetrahedrons. A non-coplanar configuration with spin chirality arises from the anisotropy of Nd spins. (b) The solid angle subtended by the Nd spins is partially transferred to that of Mo conduction electrons. (c) The Hall resistivity sets in at a low temperature when the applied magnetic field that suppresses the spin chirality decreases.

In addition to the $\boldsymbol{B}$ field, the effect of $\boldsymbol{E}$ is also observable in realistic settings. According to Faraday's law, E can be induced by dB/dt, and hence, the effect of E can be seen in the dynamics of skyrmions. These dynamics are relevant for realistic systems such as MnSi, where experiments revealed that the motion of the skyrmion crystal could be triggered by a low current density[77]. A theoretical framework on the coupled dynamics of the skyrmions and conduction electrons[195] has been developed. The skyrmion's effective magnetic flux induces dB/dt, and hence, $\boldsymbol{E}$ due to the electromagnetic induction. This $\boldsymbol{E}$ field leads to an additional Hall effect to the topological AHE due to static $\boldsymbol{B}$ discussed above. Many other effects are predicted from Eq.(1.18) and Eq.(1.19), such as a new mechanism for damping the skyrmion motion and the motion of the skyrmion transverse to the current (skyrmion Hall effect).

1.3.2 Berry phase in momentum space

Next, we proceed to review the concept of momentum-space Berry phase for electron bands[194, 187], which is a primary focus of this thesis. By exploring this topic, we

aim to elucidate how the k-space Berry phase leads to a distinctive gyration behavior of electrons, ultimately resulting in an orbital magnetization that holds paramount significance for our subsequent discussions.

Electrons in solids can be described by Hamiltonian $H_0 = -\frac{\nabla^2}{2m} + V(r)$ where V is a periodical potential. Using Bloch theorem[6], the eigenstates of the Hamiltonian H can be expressed as the following form:

$$\psi_{n\boldsymbol{k}}(\boldsymbol{r}) = u_{n\boldsymbol{k}}(\boldsymbol{r})e^{i\boldsymbol{k}\cdot\boldsymbol{r}} \tag{1.20}$$

where $\boldsymbol{k}$ is the crystal momentum, n labels the band. Here we have ignored the spin part of the wavefunction since two spin states (spin-up and spin-down) are degenerate. The function $u_{n\boldsymbol{k}}(\boldsymbol{r})$ is a cell-periodic function satisfying $u_{n\boldsymbol{k}}(\boldsymbol{r}) = u_{n\boldsymbol{k}}(\boldsymbol{r}+\boldsymbol{a})$, where $\boldsymbol{a}$ is an arbitrary lattice vector.From Eq.(1.20), it is straightforward to show that functions u_{nk} is the eigenstate of the transformed Hamiltonian

$$H_k = e^{-ikr}H_0e^{ikr} = \frac{(-i\nabla + k)^2}{2m} + V(r). \tag{1.21}$$

Using function u_{nk} we can define a Berry connection $\mathcal{A}$ as follows:

$$\mathcal{A}(k) = i\langle u_{n\boldsymbol{k}}|\boldsymbol{\nabla}_{\boldsymbol{k}}|u_{n\boldsymbol{k}}\rangle \tag{1.22}$$

whereas the momentum-space Berry curvature in this band is defined as

$$\boldsymbol{\Omega}(k) = i\boldsymbol{\nabla}_{\boldsymbol{k}} \times \langle u_{n\boldsymbol{k}}|\boldsymbol{\nabla}_{\boldsymbol{k}}|u_{n\boldsymbol{k}}\rangle \tag{1.23}$$

This Berry curvature characterizes the geometry of the band. As we will see below, this band geometry leads to observable effects that will be crucial for our discussion in this thesis.

One prominent outcome of the momentum-space Berry curvature is the electrons' gyration motion in real space. This motion results in an orbital magnetization M. This effect is studied in Ref.[172, 188, 155] and is reviewed in [187]. Indeed, as

shown in Ref.[187], the orbital magnetization of electrons consists of two parts: The first contribution M_C arises from the cyclotron motion of the electron wavepacket's center of mass. The second contribution M_{SR} arises from the electron wavepacket's self-rotation — rotation around its center of mass. Their expressions are given by

$$M_C = \frac{e\epsilon_{\alpha\beta}}{\hbar c} i \sum_k (\mu - \epsilon_k) \langle \partial_{k_\alpha} u_k | \partial_{k_\beta} u_k \rangle f_k = \frac{e}{\hbar c} \sum_k (\mu - \epsilon_k) \Omega_k f_k \tag{1.24}$$

$$M_{\mathrm{SR}} = \frac{-e\epsilon_{\alpha\beta}}{2\hbar c} \sum_k i \langle \partial_{k_\alpha} u_k | H_k - \epsilon_k | \partial_{k_\beta} u_k \rangle f_k \tag{1.25}$$

where f_k represents the occupation number of state k: $f_k = \Theta(\mu - \epsilon_k)$, ϵ_k is the energy The sum of these two contributions yields the total orbital magnetization:

$$M = M_C + M_{\mathrm{SR}} = \frac{-e\epsilon_{\alpha\beta}}{2\hbar c} \sum_k i \langle \partial_{k_\alpha} u_k | \tilde{H}_k + \epsilon_k - 2\mu | \partial_{k_\beta} u_k \rangle f_k \tag{1.26}$$

Interestingly, the center-of-mass contribution to orbital magnetization M_C is explicitly proportional to the Berry curvature of the band. To understand this result, below, we give a pedagogical derivation of M_C based on the discussion presented in Ref. [187]. The derivation of the self-rotation part of the magnetization M_{SR}, which is derived in Ref.[28] and [188], is more technical and involved. We will not repeat this derivation here. However, in Sec.1.4, we will derivate M_{SR} under a special setting — a two-band model with particle-hole symmetry, which is the case of our interest. In this setting, we will see that the derivation is greatly simplified, and the expression of M_{SR} will be directly related to the Berry curvature.

The center-of-mass motion of the electron wavepacket contributes to orbital magnetization in the form of a loop current. Namely, local electrons move around a cyclotron center. Therefore, to calculate M_C, we need to know the local current density. However, the current density generated by this motion vanishes inside the bulk since the opposite motion of nearby cyclotrons cancels. Therefore, the easiest way to expose this current is by considering a finite system, where we expect a current to flow on the system's edge.

Here, we consider a disk. Let the trapping potential which defines the system be

$V(r)$, and we find that the current flowing along the edge of the disk is simply a Hall current generated by the gradient of V:

$$j_{\parallel}(r) = \frac{1}{e}\partial_r V(r)\sigma_{xy}(r) \tag{1.27}$$

Here $\sigma_{xy}(r)$ is the Hall conductivity at radius r. Using the relation between Hall conductivity and Berry curvature[187]: $\sigma_{xy} = \frac{e^2}{\hbar}\sum_k \Omega_k f(\epsilon_k - \mu + V)$, where f is the Fermi Dirac distribution function, and carrying out the integral along the radial direction, one finds the total current circulating around the disk is given by:

$$I = \int dr j_{\parallel}(r) = \frac{e}{\hbar}\int dr \partial_r V(r) \sum_k \Omega_k f(\epsilon_k - \mu + V(r)) = \frac{e}{\hbar}\sum_k (\mu - \epsilon_k)\,\Omega_k f_k \tag{1.28}$$

Here f_k is the Fermi Dirac distribution function. Using the definition of orbital magnetization, which is the magnetic dipole moment per unit area, we find $M_C = IA/A = I$, which gives the result in Eq.(1.24).

Although the derivation of M_C describes it through the current flowing along the system edge, the M_C is not an edge effect. Rather, it represents a uniform magnetization in the system bulk. The edge is only a tool to reflects M_C uniformly distributed in the bulk. Therefore, a magnetic flux ϕ threading the sample would sense M_C even if the flux ϕ is localized deep in the bulk where no net current exists. This situation will be important for our discussion later.

1.4 Stoner magnetism in the presence of Berry curvature: the case of multilayer graphene

In order to illustrate the impact of Berry curvature on Stoner magnetism, we will utilize untwisted graphene multilayers as a realistic platform[58]. These materials consist of stacked atomic layers of graphene which can be readily exfoliated from graphite[134]. Due to their two-dimensional nature, these materials offer the ability to tune various properties through electrical gates, including the band structure and

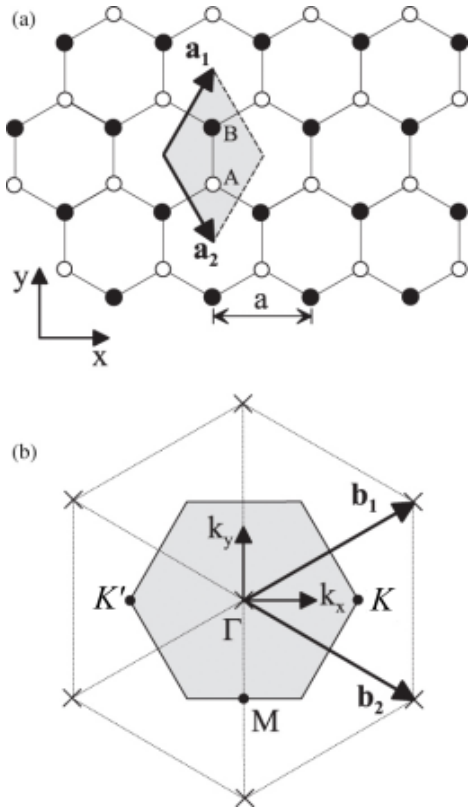

Figure 1-2: Crystal structure of monolayer graphene (adapted from Ref.[110])

carrier density. Consequently, they have garnered significant theoretical and experimental attention, making them an ideal subject for research.

Here we will focus on two materials in the family of graphene multilayers: Bernal bilayer graphene (BBG)[107, 110] and rhombohedral trilayer graphene (RTG)[101]. As we will show below, these systems naturally realize the two properties that are central to the physics discussed in this thesis: bands equipped with nonvanishing Berry curvature and Stoner magnetism. To understand the origin of these two properties, one needs to first understand the band structure of these materials. Therefore, below we will review the crystal structure, the tight binding model, and the low-energy effective model. Based on these preparations, we will derive explicitly the Berry curvature and the resulting orbital magnetization in these systems, and discuss the Stoner magnetism which is observed recently[202, 203, 201, 150, 35].

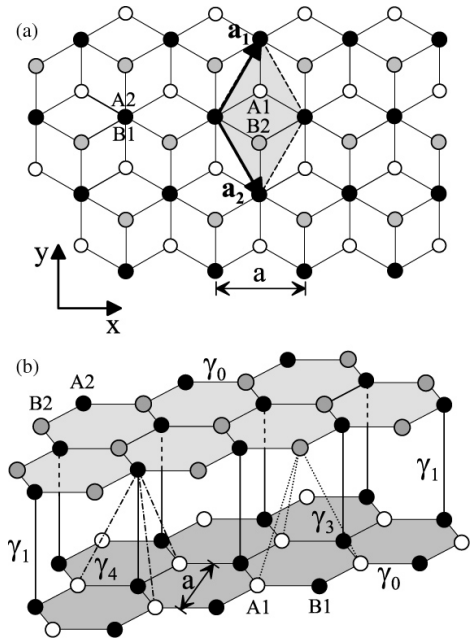

Figure 1-3: Crystal structure of BBG (adapted from Ref.[110]). a) the top view, b) a side view. The quantities γ_i $(i = 0, 1, 3, 4)$ in b) represent the hopping elements accounted by the tight-binding Hamiltonian.

1.4.1 Crystal structure and spatial symmetry in multilayer graphene

We begin by reviewing the crystal structure of multilayer graphene, which serves as a foundation for understanding the electron band structure in these materials. While our primary focus remains on BBG, we will briefly comment on the RTG when necessary, given the similarities between the two systems.

Bernal bilayer graphene is composed of two layers of graphene monolayers, each featuring a hexagonal crystal structure made up of carbon atoms arranged in a honeycomb lattice (as illustrated in Fig.1-2a)). Each unit cell of BBG consists of four carbon atoms, labeled A1, B1 on the lower layer, and A2, B2 on the upper layer (as depicted in Fig.1-3 a)). In this configuration, the B site from the lower layer (B1) is situated directly beneath the A site from the upper layer (A2) in each unit cell. These two atomic sites are referred to as "dimer" sites, owing to their relatively strong interlayer coupling. Conversely, the other two atoms, A1 and B2, are not positioned directly above or below any atoms in the other layer and are hence referred to as

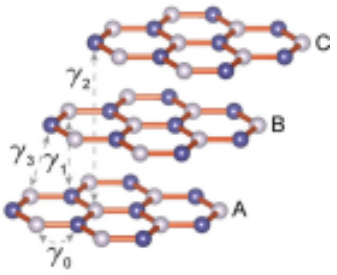

Figure 1-4: The crystal structure of RTG (adapted from Ref.[11]).

"non-dimer" sites. As we will see below, the orbitals on these two non-dimer sites predominantly form the two bands that are relevant for low-energy physics.

We note parenthetically that the atomic structure of RTG[202, 203] (See fig. 1-4) is similar to that in BBG. In RTG, the B site from the lowest layer (B1) is situated directly beneath the A site in the middle layer (A2), and the B site in the middle layer (B2) is directly beneath the A site in the top layer (A3). The other two sites in the unit cell (A1 and B2) are not aligned with any sites in the layers directly above or below.

Next, we proceed to analyze the crystalline symmetries in multilayer graphene, which will be important for our discussion of orbital magnetism and chiral interaction in the forthcoming sections. Notably, BBG and RTG have exactly the same symmetry group[110]. Namely, in the absence of any applied field, the point group of BBG and RTG is D_{3d} [110, 89, 104, 93], which consists of elements $\{E, 2C_3, 3C_2', i, 2S_6, 3\sigma_d\}$, and can be considered as a direct product of group D_3: $\{E, 2C_3, 3C_2'\}$ with the inversion group C_i ($\{E, i\}$). Thus, the lattice is symmetric with respect to spatial inversion symmetry $(x, y, z) \to (-x, -y, -z)$. In comparison, the symmetry is lowered upon applying a transverse electric field, which is the case of our interest throughout the thesis, as we will explain below. This field generates a voltage difference between two layers, breaking the inversion symmetry i and C_2', but preserves the mirror symmetries M that map K to K'. Consequently, the point group symmetry is lowered to C_{3v}, which consists of $\{E, 2C_3, 3M\}$.

1.4.2 Tight-binding description and band structure

In this section, we introduce the tight-binding description of multilayer graphene band structure[107, 110]. By examining the band structure, we demonstrate band flattening due to an applied transverse electric field, an effect that quenches the kinetic energy of electrons and drives the Stoner instability. We will also obtain the low-energy effective model which will be frequently used in the following chapters. As before, we will focus on the case of BBG [110] and will briefly comment on the case of RTG.

The low-energy theory of BBG can be described by a tight-binding model constructed from $2p_z$ orbitals on the four atomic sites in the unit cell, A1, B1, A2, and B2. The resulting tight-binding Hamiltonian takes the form of the following 4×4 matrix [110, 109, 62, 131, 140, 120, 119]

$$H_{BBG} = \begin{pmatrix} \epsilon_{A1} & -\gamma_0 f(k) & \gamma_4 f(k) & -\gamma_3 f^*(k) \\ -\gamma_0 f^*(k) & \epsilon_{B1} & \gamma_1 & \gamma_4 f(k) \\ \gamma_4 f^*(k) & \gamma_1 & \epsilon_{A2} & -\gamma_0 f(k) \\ -\gamma_3 f(k) & \gamma_4 f^*(k) & -\gamma_0 f^*(k) & \epsilon_{A1} \end{pmatrix} \tag{1.29}$$

Here, the hopping elements are shown in Fig.1-3, and are defined as follows[110]:

$$\gamma_0 = -\langle \phi_{A1}|H|\phi_{B1}\rangle = -\langle \phi_{A2}|H|\phi_{B2}\rangle \tag{1.30}$$

$$\gamma_1 = \langle \phi_{A2}|H|\phi_{B1}\rangle \tag{1.31}$$

$$\gamma_3 = -\langle \phi_{A1}|H|\phi_{B2}\rangle \tag{1.32}$$

$$\gamma_4 = \langle \phi_{A1}|H|\phi_{A2}\rangle = \langle \phi_{B1}|H|\phi_{B2}\rangle. \tag{1.33}$$

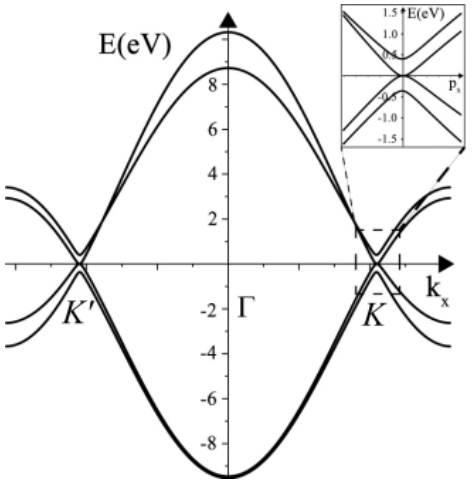

Figure 1-5: Low-energy bands of bilayer graphene arising from $2p_z$ orbitals (adapted from Ref.[110]). The inset shows the bands in the vicinity of the K point. Plots were made using Hamiltonian H, Eq.(1.29), with parameter values $\gamma_0 = 3.16$eV, $\gamma_1 = 0.381$eV, $\gamma_3 = 0.38$eV, $\gamma_4 = 0.14$eV, $\Delta' = 0.022$eV, and $U = \delta_{AB} = 0$ [92].

The quantities $\epsilon_{A1}, \epsilon_{B1}, \epsilon_{A2}, \epsilon_{B2}$ are onsite energies which are given by

$$\epsilon_{A1} = -D + \frac{1}{2}\delta_{AB} \tag{1.34}$$

$$\epsilon_{B1} = -D + \Delta' - \frac{1}{2}\delta_{AB} \tag{1.35}$$

$$\epsilon_{A2} = D + \Delta' + \frac{1}{2}\delta_{AB} \tag{1.36}$$

$$\epsilon_{A2} = D - \frac{1}{2}\delta_{AB} \tag{1.37}$$

Here U represents a bias between the two layers [109, 62, 137, 107, 139, 114, 26, 4, 110, 63, 108, 61, 56, 20], Δ' is the onsite energy difference between dimer and non-dimer sites [131, 197, 97, 43] , and δ_{AB} is the intralayer sublattice energy imbalance [119, 118].Among all these parameters, D is tunable by gate voltages, which provides a crucial knob for low-energy physics, as we will discuss shortly. Other parameters γ_0, γ_1, γ_3, γ_4, Δ', δ_{AB} are given and have been probed by various methods in experiments. We summarize several choices of realistic parameters in Table. In the absence of interlayer bias U, the band structure given by Eq.(1.29) is shown in Fig.1-5, which is plotted using one set of the parameter (see caption).

In the realistic doping regime where the carrier density is $n \sim 10^{12}\text{cm}^{-2}$, the

Fermi surfaces in BBG and RTG are small pockets around two valleys K and K', with a radius $k_F \ll K$. These two valleys are related by time-reversal symmetry, such that $K' = -K$. Consequently, the low-energy physics can be described by an effective model that only involves carriers near K and K'. To simplify the expression, we define momentum measured from K and K' as $p = \hbar(k - \xi K)$, where $\xi = \pm 1$ denotes the valley index. Expanding the function $f(\boldsymbol{k})$ in powers of p, we obtain $f(\boldsymbol{k}) \approx -\sqrt{3}a(\xi p_x - \mathrm{i}p_y)/2\hbar$. Plugging this expression into Eq.(1.29), we obtain the following four-band Hamiltonian in the basis $\left\{c^{\xi,s}_{A,1}, c^{\xi,s}_{B,1}, c^{\xi,s}_{A,2}, c^{\xi,s}_{B,2}\right\}$, where A and B denote the sublattice indices, 1 and 2 denote the layer indices, $\eta = \pm 1$ denotes the valley index, and s denotes the spin index [110]:

$$H^{(4)}_{\xi}(\boldsymbol{p}) = \begin{pmatrix} D & v\pi^{\dagger} & -v_4\pi^{\dagger} & v_3\pi \\ v\pi & D + \Delta' & \gamma_1 & -v_4\pi^{\dagger} \\ -v_4\pi & \gamma_1 & -D + \Delta' & v\pi^{\dagger} \\ v_3\pi^{\dagger} & -v_4\pi & v\pi & -D \end{pmatrix} \tag{1.38}$$

where $\pi = \hbar\,(\xi p_x + i p_y)$, Here v, v_3, v_4 are associated with the microscopic hopping amplitudes through $v = \frac{\sqrt{3}a\gamma_0}{2\hbar}$, $v_3 = \frac{\sqrt{3}a\gamma_3}{2\hbar}$, $v_4 = \frac{\sqrt{3}a\gamma_4}{2\hbar}$.

This four-band model can be simplified further into a two-band model in the realistic doping regime. This is because the top and bottom bands are sufficiently isolated from the two bands next to charge neutrality by a gap of ~ 400meV at K and K' points. This energy scale is much larger than the Fermi energy measured from the bottom of the second band, which is between 1meV and 10meV for a realistic carrier density ($n \sim 10^{12}\mathrm{cm}^{-2}$). Switching on the transverse field does not change the comparison of energy scales because the interlayer bias generated by a realistic transverse field is below 100meV[201, 150, 35], which is much smaller than γ_1. Therefore, in our analysis, we can safely focus on the top and bottom bands near charge neutrality. Thus, we project H_{BBG} to the two bands next to the charge neutrality while ignoring the subleading terms such as v_3, v_4, and Δ' in Eq.(1.38). The impacts of these subleading terms are interesting but inessential for the description here and will be accounted for later. This band projection directly yields a quadratic Dirac

model under the basis of $\{\psi_{A\xi\boldsymbol{p}}, \psi_{B\xi\boldsymbol{p}}\}$:

$$H_{\xi}^{(2)}(\boldsymbol{p}) = h_1(\boldsymbol{p})\sigma_1 + h_2(\boldsymbol{p})\xi\sigma_2 + D\sigma_3 \tag{1.39}$$

where $m = \frac{\gamma_1}{2v^2}$, $\sigma_{1,2,3}$ are the Pauli matrices acting on the sublattice (A, B) subspace. As a reminder, $\xi = \pm 1$ denotes valley K and K'. The quantity D is the interlayer bias generated by the transverse electric field. Here h_1 and h_2 are given by

$$h_1(\boldsymbol{p}) = -\frac{1}{2m}\left(p_1^2 - p_2^2\right), \quad h_2(\boldsymbol{p}) = -\frac{p_1 p_2}{m}. \tag{1.40}$$

This quadratic Dirac Hamiltonian yields the following dispersion

$$\epsilon_k = \pm\sqrt{D^2 + \left(\frac{p^2}{2m}\right)^2} \tag{1.41}$$

Throughout this thesis, we will frequently this quadratic Dirac model to describe electrons in BBG since it is a minimal model that captures the main properties of carriers. The only exception is in a few sections in Chapter 2 where the details, such as trigonal warpings of the band, become essential to the physics discussed there.

1.4.3 Berry curvature and orbital magnetization in multilayer graphene

Equipped with a comprehensive understanding of the band structure, we now proceed to demonstrate the presence of non-zero Berry curvature within the BBG bands through a direct calculation. Subsequently, we will compute the orbital magnetization that arises from the Berry curvature following the approac. This result will be utilized in our analysis of chiral interaction (see Chapter 3).

Specifically, we calculate the Berry curvature using the quadratic Dirac band model Eq.(1.39). To this end, we first compute the Berry phase for a circular trajectory with radius p centered at the K point. This phase is precisely equal to the solid

angle enclosed by the vector (h_1, h_2, D):

$$\gamma_p^{\pm} = \pm 2\pi \left(1 - \frac{D}{\sqrt{D^2 + (p^2/2m)^2}} \right) \tag{1.42}$$

Here $\pm$ corresponds to upper and lower Dirac bands, respectively. Then the Berry curvature at momentum p can be easily obtained using the definition of Berry curvature[196, 187]:

$$\Omega_p^{\pm} = \frac{\hbar^2}{2\pi p} \frac{\partial \gamma_p}{\partial p} = \pm \frac{\hbar^2}{2} \frac{Dp^2/m^2}{\left(D^2 + (p^2/2m)^2\right)^{3/2}} \tag{1.43}$$

Here we have used the U(1) rotation symmetry of the quadratic Dirac band Eq.(1.39), which requires $\Omega_p^{\pm}$ to be invariant when p is rotated around K point.

The nontrivial band geometry in BBG leads to a nonvanishing orbital magnetization for each valley, which is a property useful for the analysis in the following chapters. Therefore, below we calculate the orbital magnetization in each valley using Eq.(1.26). To simplify the calculation, we can utilize the following identity[189], which holds for a generic particle-hole symmetric two-band model:

$$\mathrm{Im}\, \langle \boldsymbol{\nabla}_{\boldsymbol{p}} u_p^n | \times H(p) | \boldsymbol{\nabla}_{\boldsymbol{p}} u_p^n \rangle = -\epsilon_p^n \,\mathrm{Im}\, \langle \boldsymbol{\nabla}_{\boldsymbol{k}} u_p^n | \times | \boldsymbol{\nabla}_{\boldsymbol{p}} u_p^n \rangle = -\epsilon_p^n \Omega_p^n. \tag{1.44}$$

Here $n = \pm$ represents the upper and lower bands. This identity can be derived by writing H as a sum of projections on upper and lower bands, namely, the left-hand side of Eq.(1.44) is equal to

$$\sum_{m=\pm} \epsilon_p^m \,\mathrm{Im}\, \left(\langle \boldsymbol{\nabla}_{\boldsymbol{p}} u_p^n | u_k^m \rangle \times \langle u_p^m | \boldsymbol{\nabla}_{\boldsymbol{p}} u_p^n \rangle \right) \tag{1.45}$$

Then, using particle-hole symmetry of the band dispersion $\epsilon_p^- = -\epsilon_p^+$, and the identity $\mathrm{Re}\, \langle \boldsymbol{\nabla}_{\boldsymbol{p}} u_p^n | u_p^n \rangle = 0$ one find Eq.(1.45)can be further reduced to:

$$-\epsilon_p^n \,\mathrm{Im}\, \left(\langle \boldsymbol{\nabla}_{\boldsymbol{p}} u_p^n | u_p^{-n} \rangle \times \langle u_p^{-n} | \boldsymbol{\nabla}_{\boldsymbol{p}} u_p^n \rangle \right). \tag{1.46}$$

Then using $\mathrm{Re}\, \langle \boldsymbol{\nabla}_{\boldsymbol{p}} u_p^n | u_p^n \rangle = 0$ again we arrive at the right-hand side of Eq.(1.44).

Plugging the identity Eq.(1.44) into Eq.(1.25) gives the self-rotation contribution to the orbital magnetization for each spin species [189]:

$$M_{\mathrm{SR}}=\frac{e\epsilon_{\alpha\beta}}{2\hbar c}\sum_{p}\mathrm{Im}\left\langle\partial_{p_\alpha}u_k|H_k-\epsilon_k|\partial_{p_\beta}u_p\right\rangle f_p=\frac{e}{\hbar c}\sum_{p,\pm}\epsilon_p^{\pm}\Omega_p^{\pm}f(\epsilon_p^{\pm}-\mu) \tag{1.47}$$

As a result, the total orbital magnetization for each spin speciesm is

$$M=\frac{e}{\hbar c}\sum_{p,\pm}\left(\epsilon_p^{\pm}+\mu-\epsilon_p^{\pm}\right)\Omega_p^{\pm}f(\epsilon_p^{\pm}-\mu)=\frac{e\mu}{\hbar c}\sum_{p,\pm}\Omega_p^{\pm}f(\epsilon_p^{\pm}-\mu) \tag{1.48}$$

Finally, we apply this generic expression to electrons in one valley of BBG. Plugging Eq.(1.43) into Eq.(1.48), we arrive at the following expression for the total orbital magnetization for each spin species in valley K of BBG[1]:

$$M_K^{\mathrm{BBG}}(\mu)=\begin{cases}\frac{eD}{2\pi\hbar}, & \mu>D\\ \frac{e\mu}{2\pi\hbar}, & -D<\mu<D\\ -\frac{eD}{2\pi\hbar}, & \mu<-D\end{cases}. \tag{1.49}$$

The orbital magnetization in valley K' is associated with that in valley K through the relation: $M_{K'}^{\mathrm{BBG}}(\mu)=-M_K^{\mathrm{BBG}}(\mu)$ due to time-reversal symmetry. These results show that the orbital magnetization is activated upon applying the transverse field D and vanishes in the absence of D. This behavior is consistent with the anticipated behavior based on the symmetry analysis presented above . In particular, the system exhibits C_2 symmetry when $D=0$, resulting in the enforced vanishing of the valley orbital magnetization. However, a non-zero D breaks the C_2 symmetry, thereby enabling the emergence of a nonvanishing valley orbital magnetization.

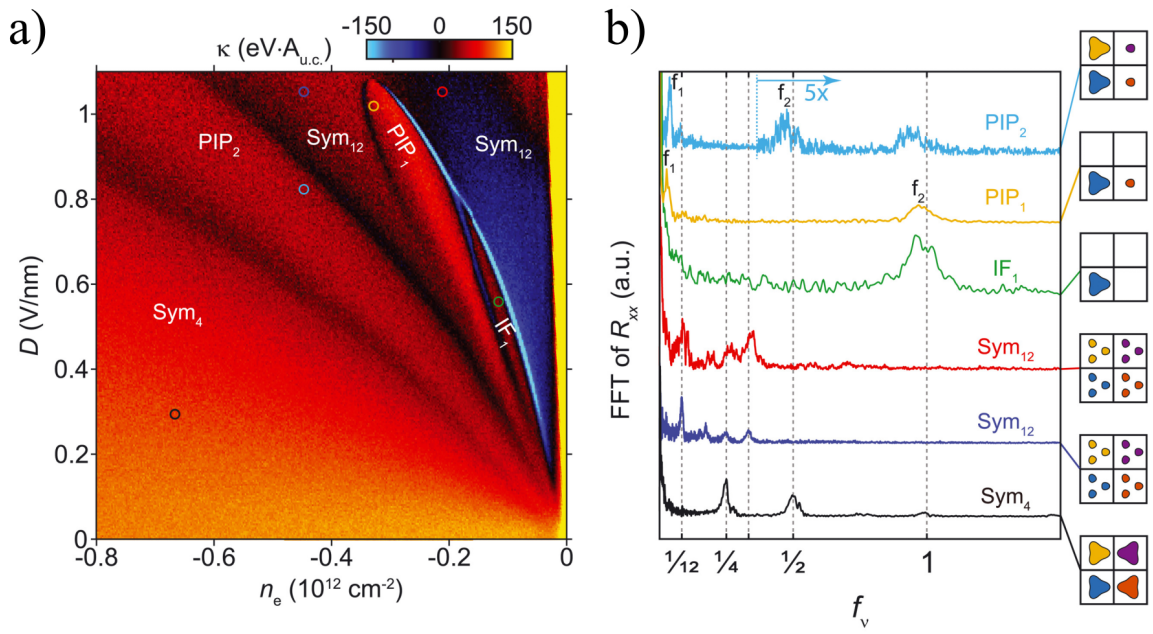

Figure 1-6: Adapted from Ref.[201]. a) Measured inverse compressibility in BBG at zero magnetic field. The x axis is the electron density n_e. A negative value of n_e means hole doping. The y axis is the strength of the displacement field. b) Fast Fourier transform (FFT) of $R_{xx}(1/B_\perp)$ measured at the (n_e, D) points indicated by the colored symbols in a). The x axis is the frequency normalized to n_e. Peaks reflect fractional areas of the Fermi seas enclosed by a phase-coherent orbit. The inset for each trace is a schematic of the Fermi seas in four isospin species.

1.4.4 Stoner orders in multilayer graphene

Stoner magnetism is expected to occur in BBG since its flattened band structure, described by Eq. (1.41), results in a high density of states at low carrier density and high transverse field. This high density of states makes the system highly susceptible to the Stoner instability, as indicated by the Stoner criterion in Eq. (1.7). Indeed, direct numerical calculations (see Chapter 2 and Ref.[202]) predict a variety of isospin-polarized phases occurring in BBG and RTG, where the balance of electron occupation number in valley K and K' and that in spin $\uparrow$ and $\downarrow$ is spontaneously broken.

Recent experiments[201, 35, 150] have confirmed the presence of these isospin-polarized phases. Shown in Fig.1-6 a) is a typical phase diagram of BBG, adapted from Ref.[201]. Here, the color code represents the measured inverse compressibility. Each abrupt change of color indicates a phase transition between various phases of different isospin polarization. A similar cascade of isospin-polarized phases has been observed in RTG[202, 203]. In the experiments, the degeneracy of spin and valley species is determined by measuring the quantum oscillation frequency[201, 35]. Namely, in an applied out-of-plane $B_\perp$ field, the resistivity oscillates periodically as a function of $1/B_\perp$ due to Landau levels crossing the Fermi level[6]. The quantum oscillation frequency is proportional to the size of each pocket. Thus the degeneracy of isospin species can be determined by comparing the quantum oscillation frequency with the total carrier density n, which can be extracted from gate voltages. Using this technique, the authors of Ref.[201] identify several types of isospin polarized phases, such as a partially isospin polarized phase (PIP_2) where two out of four isospins have higher densities than the other two, and a fully isospin polarized phase where all carriers are in one isospin species.

[1]It should be noted that the expression for M_K^{BBG} used in this thesis differs from the result obtained from Eq.(1.48) by an overall minus sign. Therefore, the M_K^{BBG} in this thesis should be considered as the orbital magnetization along $-z$ direction. This convention is chosen for convenience and does not affect the analysis.

1.5 Thesis outline

In the following chapters of this thesis, we will explore how Stoner magnetism and Berry curvature give rise to new interactions, orders, and physics.

In Chapter 2 we will look into the details of Stoner orders in Bernal multilayer graphene. The material of this chapter is based on Ref.[38]. We will start by determining the phase diagram of isospin magnetism in BBG. Then, we will extend the concept of Stoner instability to fermi pockets in momentum space and demonstrate that isospin Stoner orders coexist with momentum-polarized phases that arise through a "flocking transition" in momentum space. These phases exhibit unique observables such as persistent currents in the ground state. Furthermore, momentum-polarized carriers "sample" the Berry curvature of the conduction band, which results in a distinctive behavior of the anomalous Hall conductivity and an overall orbital magnetization. These findings will provide additional evidence that BBG possesses a range of Stoner orders that coexist with an orbital magnetization.

Chapter 3 is based on Ref.[40]. In this chapter we will demonstrate a key effect that arises from Stoner magnetism in bands with Berry curvature — the chiral interaction between Berry's orbital magnetization and spin chirality density. This chiral interaction originates from carriers moving in the presence of a spin texture. As discussed above, the carriers see the texture as a source of pseudo-magnetic field coupled to their orbital motion through a geometric Aharonov-Bohm effect. This interaction favors chiral spin textures, such as skyrmions, which are topologically protected particle-like objects. The chiral interaction lowers the threshold for Stoner instability, making chiral spin-ordered phases readily achievable under realistic conditions. We will illustrate this effect using a graphene multilayer model, with magnetization and pseudo-magnetic fields that assume distinct values in different valleys. However, the results are applicable to generic Stoner magnets in bands endowed with Berry curvature.

In Chapter 4, we will explore another phenomenon arising from the chiral interaction: the chiral spin-wave edge mode. The material of this chapter is largely based on

Ref.[41]. We will demonstrate that Stoner spin-polarized phases that occur in bands with Berry curvature spin support chiral spin-wave edge modes that propagate ballistically along system boundaries without backscattering. The edge modes are weakly confined to the edge. This unique character of edge modes reduces their overlap with edge disorder and enhances their lifetime. The mode propagation direction flips upon reversing valley polarization, providing a clear and testable signature of the chiral interaction in Dirac bands and other systems with a k-space Berry curvature.

Chapter 2

Isospin- and momentum-polarized orders in bilayer graphene

2.1 Introduction

As discussed in Introduction, quantum materials with narrow bands have been found to host a variety of strongly correlated phases with exotic properties that can be accessed by tuning external fields and carrier density. Such phases were first discovered in narrow bands in moiré graphene[15, 112, 116, 42]. These findings triggered a large body of experimental work [21, 22, 80, 190, 135, 152, 186, 185, 154, 153, 176, 37, 99, 83, 29, 76, 23, 64, 74, 90, 191, 98] and, subsequently, inspired investigations into other narrow-band systems with interesting properties. Recently, two non-twisted graphene multilayers—Bernal-stacked bilayers and rhombohedral trilayers—have been identified[202, 203, 201, 35, 150] as systems showing cascades of ordered phases resembling those seen in moiré graphene[146, 204, 30, 144, 141]. These systems feature electron bands with field-tunable bandgaps and dispersion that flattens out quickly as the field increases. Carriers in these bands become nearly dispersionless at large fields, forming strongly interacting systems with interesting properties[34, 94, 164, 27, 25, 113, 174, 78, 31]. These developments prompted questions about new symmetry-breaking types and new orders achievable in these systems.

Perhaps the most unusual aspect of these systems is that the flat band is not an

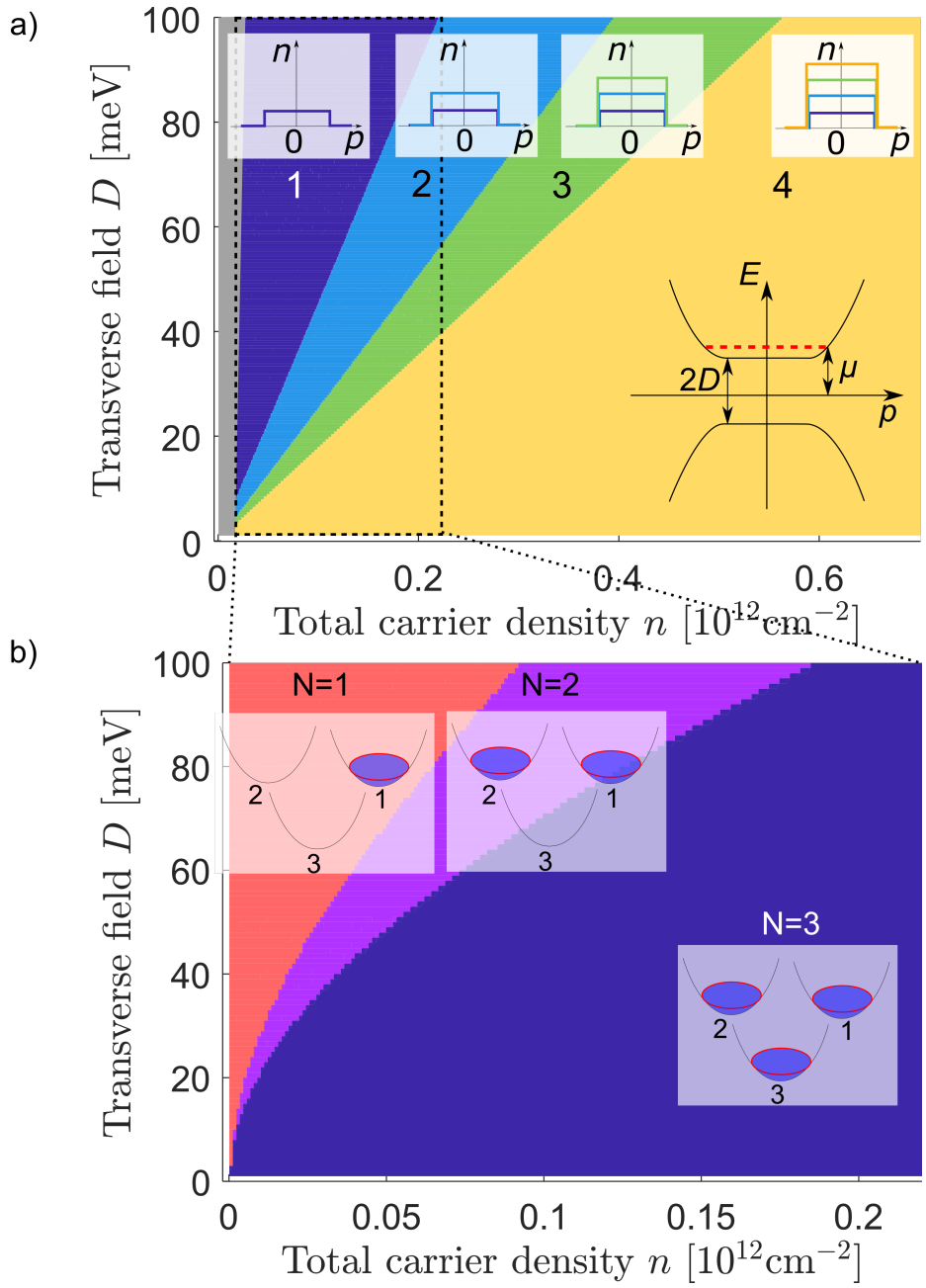

Figure 2-1: a) Phase diagram for different isospin (valley and spin) orders in a lightly-doped BBG band. Carriers form Fermi seas with the degree of isospin polarization increasing with field bias. States with different numbers of isospin species, pictured in the insets, are found in the four regions of the phase diagram obtained using realistic parameters. The polarization degree varies from one layer (fully polarized) to four layers (unpolarized) [see text beneath Eq. (2.12)]. b) Level-two symmetry breaking occurring in a dashed box marked in a). Different orders arise due to the Fermi sea spontaneously breaking into $N = 1$, 2, or 3 pockets and shifting to different band minima [see Fig. 2-2].

isolated band, as in moiré graphene. Instead, it is a flattened part of a dispersive band, with the degree of flatness and phase volume tunable by the displacement field. This behavior leads to properties distinct from those of unbiased bilayer graphene [128, 33, 174].

Here, starting from a simple Hubbard-like framework for the interaction effects in biased bilayer graphene (BBG), we analyze different order types that may occur in this system. The discussion in this Chapter is based on Ref.[39]. Electron exchange interactions in flattened bands drive isospin (spin-valley) polarization instability and produce a cascade of phase transitions between states with different polarizations, resembling those known in moiré graphene[146, 204, 30, 144, 141]. A phase diagram for this cascade, derived below and shown in Fig. 2-1 a), strongly resembles the phase diagram seen experimentally[201, 35, 150].

Further, an interesting change in behavior occurs at lower densities, where interactions lead to spontaneous momentum polarization of isospin-polarized Fermi sea, as illustrated in Fig. 2-1 b). Momentum-polarized phases originate from the exchange-induced "flocking" effect, wherein all carriers are shifted into one, two or three pockets at the band minima produced by the trigonal warping effects. These orders develop on top of the isospin-polarized phases.

Momentum-polarized states are described phenomenologically by an effective Hamiltonian:

$$\tilde{H}(\boldsymbol{k}) = H(\boldsymbol{k}) + \boldsymbol{u} \cdot \boldsymbol{k}. \tag{2.1}$$

Here $H(\boldsymbol{k})$ is the trigonal warped Hamiltonian which we can approximate with three parabolic pockets displaced from K points, as illustrated in Fig. 2-2, $\boldsymbol{u}$ is the order parameter that describes the polarization in momentum space. As we will see, a spatial dependent $\boldsymbol{u}(\boldsymbol{x})$ gives rise to a local persistent current and an orbital magnetization, which is allowed by the spontaneously broken time-reversal symmetry in momentum-polarized phases. The persistent currents and orbital magnetization generated in this way are distinct from those familiar for the bands endowed with Berry curvature.

In addition to that, the momentum-polarized carriers "sample" the Berry curvature of the conduction band, leading to jumps and other unique signatures in the anomalous Hall effect. These effects are enhanced by the redistribution of Berry curvature throughout the conduction band resulting from its trigonal warping (see Fig. 2-2). An abrupt onset of a $B = 0$ Hall effect, along with anisotropy of transport due to electronic nematicity, will provide clear signatures of momentum-polarized orders.

2.2 An effective one-band model

Isospin polarization occurs when the exchange interaction between carriers in the conduction or valence band exceeds the characteristic kinetic energy. In the BBG system, the kinetic energy is quenched when band dispersion is flattened by bandgap opening in the presence of a large transverse displacement field. This regime can be described by a one-band Hamiltonian derived by projecting the bilayer Hamiltonian to the conduction or valence band. Here we obtain this model starting from a conventional continuum two-band model (see Chapter1 or Ref.[110]):

$$
\begin{aligned}
H_0 &= \sum_{\xi s \boldsymbol{p}} \Psi^{\dagger}_{\xi s \boldsymbol{p}} \left[h_0^{\xi} + h_t^{\xi} + h_a + h_{D'} \right] \Psi_{\xi s \boldsymbol{p}} \qquad (2.2) \\
h_0^{\xi} &= h_1(\boldsymbol{p})\sigma_1 + h_2(\boldsymbol{p})\xi\sigma_2 + D\sigma_3 \\
h_t^{\xi} &= v_3 \left(p_1 \xi \sigma_1 - p_2 \sigma_2 \right), \quad h_a = \frac{p^2}{2m_a}, \quad h_{D'} = -D\frac{p^2}{\tilde{p}^2}\sigma_3
\end{aligned}
$$

where $\xi = K, K'$ represents valley K and K', $s = \uparrow, \downarrow$ represents spin-up and spin-down, $\Psi_{\xi s \boldsymbol{p}} = (\psi_{A\xi s \boldsymbol{p}}, \psi_{B\xi s \boldsymbol{p}})^{\mathrm{T}}$, $\sigma_{1,2,3}$ are the Pauli matrices acting on the valley and sublattice (layer) degrees of freedom, respectively. Unlike in Eq.(1.39) from Chapter 1, here we have included subleading terms such as trigonal warping and the quadratic term, as they are essential for the analysis of the three-pocket structure of the Fermi sea, which is crucial to our analysis in the following sections. The quantity D is the

parameter	value	parameter	value
a	2.46 Å	v	1.1×10^6 m/s
γ_0	3.16 eV	m_a	0.19 m_e
γ_1	0.381 eV	m	0.028 m_e
γ_3	0.38 eV	v_3	1.3×10^5 m/s
D	$0-100$ meV	$\tilde{p}a_{\mathrm{CC}}$	0.058

Table 2.1: Parameters in the Hamiltonian computed based on values in Ref. [110]. The velocities are defined as $v_i = (\sqrt{3}/2)a\gamma_i$ ($\hbar = 1$ throughout this paper). The BG band mass is defined as $m = \gamma_1/2v^2 \approx 0.028m_{\mathrm{e}}$.

interlayer bias generated by the transverse electric field. Here h_1 and h_2 are given by

$$h_1(\boldsymbol{p}) = -\frac{p_1^2 - p_2^2}{2m}, \quad h_2(\boldsymbol{p}) = -\frac{p_1 p_2}{m}. \tag{2.3}$$

The problem given in Eqs. (2.2) and (2.3) is derived under the assumption that intra- and interlayer hoppings (A1B1 and A2B1-type terms in the original Hamiltonian, which are 3.16 eV and 0.38 eV, respectively) are much larger than all other energy scales. Here h_t produces the trigonal warping; h_a produces the particle-hole asymmetry and $h_{D'}$ is the momentum-dependent contribution that is proportional to the displacement field with $\tilde{p} \approx 0.058/a_{\mathrm{CC}}$ a constant (see Table 2.1).

Our problem has a rich symmetry group that includes both exact and approximate symmetries. The true symmetry group of the free-electron Hamiltonian in Eq.(2) contains the spin-valley part which is $\mathrm{U(1)_v} \times \mathrm{SU(2)_K} \times \mathrm{SU(2)_{K'}}$, where $\mathrm{U(1)_v}$ describes valley conservation and $\mathrm{SU(2)_K}$, $\mathrm{SU(2)_{K'}}$ describe spin rotations performed independently in the two valleys. In addition, the true symmetry group contains a C_3 rotation, a mirror symmetry that interchanges the K and K' valleys, and lattice translations. In this and the next section, for simplicity, we focus on understanding the isospin orders in a SU(4)-symmetric model, obtained by suppressing the subleading terms[110], such as trigonal warping h_t. These terms govern subtle effects such as momentum polarization, which will be considered in Sec. 2.4 and Sec.2.5.

We measure the energies in meV and the momentum is made dimensionless by multiplying by the carbon-carbon atom distance $a_{\mathrm{CC}} = 1.46$ Å. The relevant system parameters are given in Table 2.1.

Here, we will be interested in the regime where the field-induced bandgap $2D$ is large compared to the carrier kinetic energy (see inset in Fig. 2-1 a)). In this regime, the upper and lower bands flatten out and effectively decouple. We, therefore, project the problem onto the conduction band

$$\tilde{H}_0 = \hat{P} H_0 \hat{P}, \tag{2.4}$$

Here the projection operator $\hat{P}$ is defined as

$$\hat{P} = \sum_{\xi} \frac{1}{2} \left(\frac{h_0^{\xi}(\boldsymbol{p})}{E(\boldsymbol{p})} + 1 \right), \quad E(p) = \sqrt{D^2 + \left(\frac{p^2}{2m} \right)^2}. \tag{2.5}$$

This yields a one-band SU(4)-invariant Hamiltonian $\tilde{H}_0$ of the form:

$$\tilde{H}_0 = \sum_{i\boldsymbol{p}} E(\boldsymbol{p}) \tilde{\psi}^{\dagger}_{i,\boldsymbol{p}} \tilde{\psi}_{i,\boldsymbol{p}}, \quad i = K\uparrow, K\downarrow, K'\uparrow, K'\downarrow, \tag{2.6}$$

where $\tilde{\psi}_{i,p}$ is the field operator of conduction band electrons in two valleys and two spins. From now on, we write the spin indices explicitly.

The electron-electron interaction, modeled as a density-density coupling, in notations of Eq.(2) reads:

$$H_{int} = \frac{1}{2} \sum_{\boldsymbol{p}\boldsymbol{p}'\boldsymbol{q}} V_{\boldsymbol{q}} \psi^{\dagger}_{\alpha\xi s,\boldsymbol{p}} \psi^{\dagger}_{\beta\xi' s'\boldsymbol{p}'} \psi_{\beta\xi' s'(\boldsymbol{p}'-\boldsymbol{q})} \psi_{\alpha\xi s(\boldsymbol{p}+\boldsymbol{q})}, \tag{2.7}$$

where ξ, ξ' label the valley degree of freedom, s, s' label the spin degree of freedom, and α, β label the sublattice degree of freedom. We adopt the usual convention that the repeated pairs of indices are summed over. This interaction in Eq.(7), obtained by suppressing the intervalley scattering processes and ignoring the difference between the interlayer and intralayer interactions, is invariant under SU(4) spin/valley rotations. At large D, the form of density-density interaction is approximately invariant

under projection onto the conduction band:

$$\tilde{H}_{int} = \frac{1}{2}\sum_{\boldsymbol{p}\boldsymbol{p}'\boldsymbol{q}} V_{\boldsymbol{q}} \tilde{\psi}^{\dagger}_{i,\boldsymbol{p}} \tilde{\psi}^{\dagger}_{j,\boldsymbol{p}'} \tilde{\psi}_{j,\boldsymbol{p}'-\boldsymbol{q}} \tilde{\psi}_{i,\boldsymbol{p}+\boldsymbol{q}} \tag{2.8}$$

Similar to Eq. (2.6), subscripts i and j take values $K\uparrow$, $K\downarrow$, $K'\uparrow$, $K'\downarrow$. Here we ignore the intervalley Coulomb scattering because the interaction $V_{\boldsymbol{q}}$ drops as $1/q$, leading to intervalley interactions that are smaller than the intra-valley interaction by a factor of $p_F/2K$ which is as small as 0.04 at carrier density 10^{12}cm^{-2}. As a result, the approximate Hamiltonian, Eq.(2.8), has an isospin SU(4) symmetry. We note parenthetically that at a small D field, Eq. (2.8) is no longer a good approximation since it should include a coherence factor that depends on the valley and momenta. This makes the strength of coupling between charge densities in valley K different from the coupling between charge densities in valley K and valley K', breaking the approximate SU(4) symmetry. However, this SU(4) symmetry-breaking effect is small in the regime of interest. Namely, since these coherence factors are $1-\mathcal{O}(E_F/D)$, the difference between the coherence factor in the intervalley density-density coupling term $\psi^{\dagger}_K\psi_K\psi^{\dagger}_{K'}\psi_{K'}$ and the one in the intravalley density-density coupling term $\psi^{\dagger}_K\psi_K\psi^{\dagger}_K\psi_K$ is at most $\mathcal{O}(E_F/D)$, which is small when displacement field D is much larger than the Fermi energy E_F.

To gain insight into the parameter regime for isospin polarization occurs we use a simple constant interaction model, refining it in the subsequent analysis of momentum polarized order. The isospin order is a result of a Stoner instability arising from the exchange energy, which can be written as

$$E_{\text{ex}} = -\frac{1}{2}\sum_{i\boldsymbol{q}\boldsymbol{q}'} V_{\boldsymbol{q}-\boldsymbol{q}'} n_{i\boldsymbol{q}} n_{i\boldsymbol{q}}, \quad n_{i\boldsymbol{q}} = \langle \tilde{\psi}^{\dagger}_{i,\boldsymbol{q}} \tilde{\psi}_{i,\boldsymbol{q}} \rangle \tag{2.9}$$

where i indexes isospin as in Eq. (2.8). Below, for simplicity, we model the interaction as a local interaction, $V_{\boldsymbol{q}-\boldsymbol{q}'} = V$.

Perhaps the closest comparison to our analysis of BBG in the literature is the early work on Stoner spin instability in BBG [27, 25, 164]. This work employed an

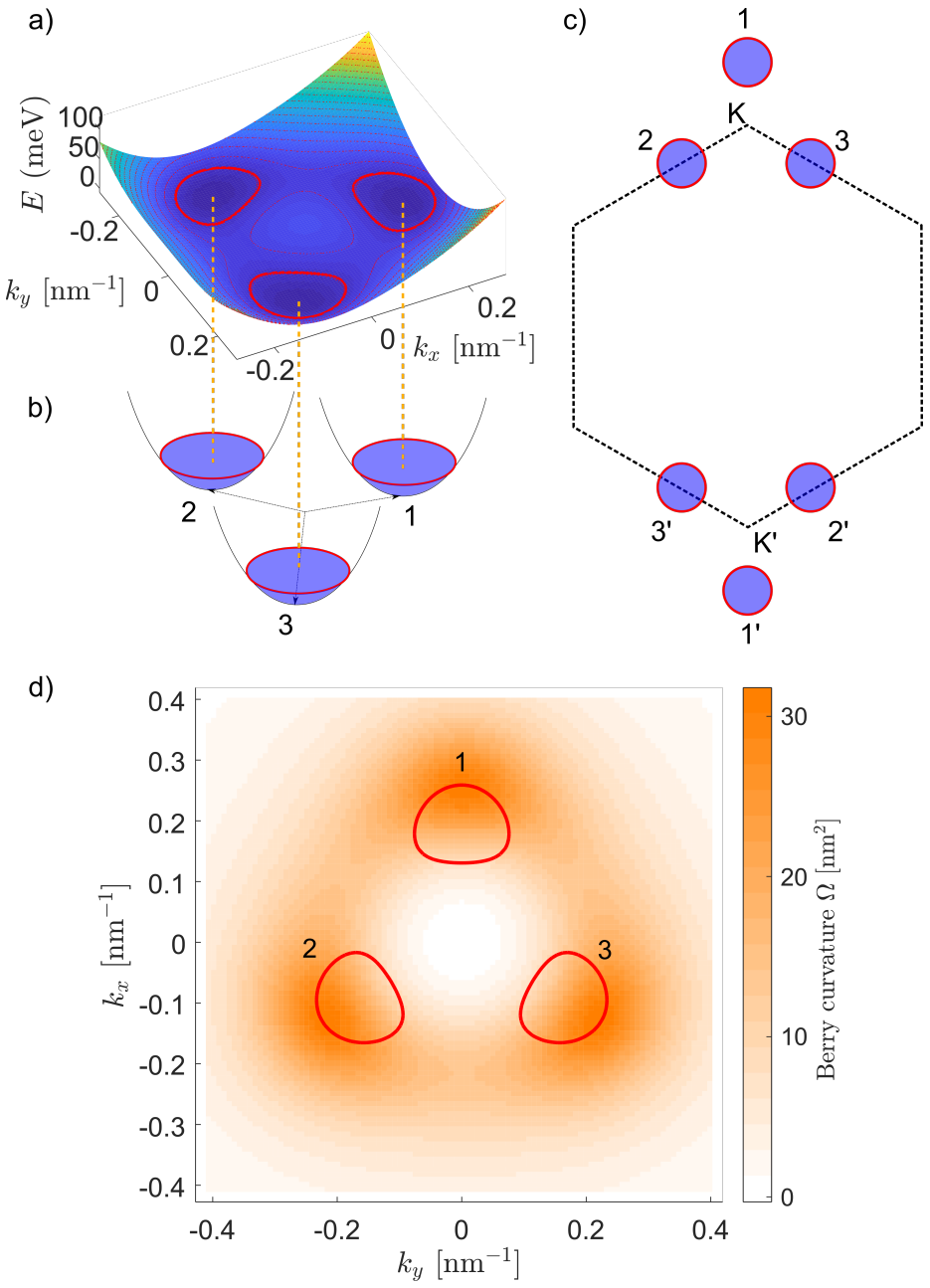

Figure 2-2: a) Conduction band dispersion flattened by transverse field. Trigonal warping interaction creates three mini-valleys, at low carrier density giving rise to three electron pockets (red contours). b) A toy model for the three-pocket band structure. c) Schematic for pockets positioned near K and K' points. d) The distribution of the Berry curvature in the conduction band near K point. Parameters used: bias potential $D = 100$ meV, the chemical potential $\mu = 90$ meV. The value $\mu < D$ reflects the effect of the trigonal warping.

atomic-scale short-ranged interaction, which did not allow treating valley and spin degrees of freedom on equal footing. The interaction used here, in contrast, is blind to valley and spin, leading to an approximate SU(4) symmetry and a cascade of isospin orders.

2.3 Broken isospin SU(4) symmetry and phase diagram

Next, we proceed to analyze the isospin polarization orders using as a framework the SU(4) symmetric model introduced above. The onset of SU(4) isospin polarization is determined by the Stoner criterion:

$$V\nu = 1, \tag{2.10}$$

with the density of states ν (per isospin species) in the conduction band,

$$\nu = \frac{m}{2\pi}\frac{\mu}{\sqrt{\mu^2 - D^2}} \approx \frac{m^2}{(2\pi)^2}\frac{D}{n}. \tag{2.11}$$

Here we have used the expression for the electron density in the single-electron picture, $n = \frac{m}{2\pi}\sqrt{\mu^2 - D^2}$, taking the chemical potential to lie near the bottom of the band, $\mu \approx D$. With this, we estimate the carrier density at the onset of the Stoner instability, finding a fan of phase boundaries n vs. D for $M = 1$, 2, or 3 isospin species:

$$n_D = M\frac{Vm^2D}{(2\pi)^2}. \tag{2.12}$$

While in general, the mean-field Stoner approach has limitations, in this case, it appears to be accurate. For BBG parameters $m = 0.028m_e$[110, 105, 180], $V = 10^3\,\mathrm{meV\,nm^2}$ [see Appendix 2.7], this simple model predicts an isospin ordering transition at carrier densities $n_D \sim 10^{12}\mathrm{cm}^{-2}$ for the interlayer bias $D = 100$ meV, in excellent agreement with Ref.[201].

irreps	$A_{2,\Gamma}$, 1D	$E_{\pm K}$, 2D
matrices	τ_3	(τ_1, τ_2)
O_1	$O_1^z = P_\tau^{\pm z} P_s^{\boldsymbol{m}}$	$O_1^{xy} = P_\tau^{\boldsymbol{\gamma}} P_s^{\boldsymbol{m}}$
broken symmetries	mirror, time reversal	rotation, mirror, translation
Ohmic conductivity	isotropic	anisotropic
spatial modulation	none	Kekulé order
Hall conductivity	nonvanishing	vanishing

Table 2.2: Symmetry classification of different isospin orders. Listed are results for two real irreducible representations (irreps) of the BBG space group discussed following Eq.(3), under which the order parameter for the full spin and valley polarized phase, $O_1 \sim (1 + \sum_i \gamma_i \tau_i) P_s^m$, can transform; other irreps ($A_{1,\Gamma}$, E_Γ, etc.) are not realized by isospin-polarized orders. Row 1 lists the irreps and their dimensions. Inrow 3, the projection operators in the valley and spin space constituting the order parameter are $P_\tau^{\pm z} = \frac{1}{2}(1 \pm \tau_3)$, $P_\tau^{\boldsymbol{\gamma}} = \frac{1}{2}(1 + \gamma_1 \tau_1 + \gamma_2 \tau_2)$, $P_s^{\boldsymbol{m}} = \frac{1}{2}(1 + \boldsymbol{s} \cdot \boldsymbol{m})$, where $\boldsymbol{\gamma} = (\gamma_1, \gamma_2)^{\mathrm{T}}$ with real $\gamma_{1,2}$, $\boldsymbol{m} = (m_1, m_2, m_3)^{\mathrm{T}}$ is an arbitrary three-dimensional real vector.rows 4-7 list broken symmetries and signature observables (see text).

The mean-field phase diagram, obtained by comparing energies of partially polarized states with $M = 1$, 2, 3, and 4 isospin species found numerically, is shown in Fig. 2-1 a). The yellow area represents the disordered phase where all four isospin species are equally filled. Purple, light blue, and green mark stability regions for isospin-ordered states. The inset in the lower right corner shows electron dispersion near charge neutrality, with the Fermi level marked by a red dashed line. The insets at the top illustrate the layer-cake structure of electron distribution in each of the phases, with the Fermi seas for different isospin species shown in different colors. The gray region near charge neutrality marks the band insulator phase with an unoccupied conduction band. The dashed rectangle marks the region of low carrier density on which the second half of this paper will focus. As we will see in Sec.2.4 and Sec.2.5, trigonal warping of the conduction band flattened by the external field D gives rise to Fermi sea breakups and level-two symmetry breaking through spontaneous momentum polarization. This behavior is summarized in the phase diagram in Fig. 2-1 b).

Because of the SU(4) symmetry of our problem, the phase diagram in Fig. 2-1 a) is insensitive to the order parameter orientation in the isospin space. However, in reality, small valley anisotropy in the Hamiltonian, e.g. trigonal warping or in-

tervalley scattering, can lift the SU(4) degeneracy and favor a certain orientation in isospin space. Here, rather than analyzing the competition between phases with different symmetries, we take a general symmetry approach and list all possible ways of breaking the SU(4) symmetry. The energetics describing this competition will be discussed elsewhere.

Our symmetry analysis benefits from the observation that the symmetry aspects of different orders and the general properties of the order parameter can be understood regardless of detailed knowledge of which order is ultimately favored. Below, we describe the possible order types and classify them through the symmetry of our problem.

For simplicity, we focus on the case of phase 1 where electrons only occupy one isospin species. Other orders can be studied in a similar manner. Table 2.2 summarizes the results for phase 1. In this case, there are two possible phases, O_1^z and O_1^{xy}, describing orders with valley imbalance and intervalley coherence, respectively. These two order types break different symmetries and have different signature observables as a result.

We arrive at this conclusion as follows. In phase 1 the order parameter is simply a projection onto the state with a given valley-spin orientation. Therefore, it takes the form of

$$O_1 = |v\rangle\langle v| \tag{2.13}$$

where v is an arbitrary normalized complex-valued four-component spinor in the isospin space, $|v\rangle = (\alpha_1|u_1\rangle, \alpha_2|u_2\rangle)^{\mathrm{T}}$ where $|u_1\rangle, |u_2\rangle$ are arbitrary normalized two-component state vectors in the spin subspace, α_1, α_2 are positive real numbers, $\alpha_1^2 + \alpha_2^2 = 1$. Overall phases are absorbed in $|u_1\rangle$ and $|u_2\rangle$. Using the symmetry $\mathrm{U(1)_v} \times \mathrm{SU(2)_K} \times \mathrm{SU(2)_{K'}}$ [see discussion following Eq.(3)] we can perform independent spin rotations in valleys K and K' to achieve $|u_1\rangle = |u_2\rangle$. Upon doing so the order parameter becomes factorized into a product of valley and spin projection, as given in Table 2.2. The symmetry analysis of the Pauli matrices in valley basis (see Table 2.2) indicates that $\tau_{1,2}$ and τ_3 transform under different irreducible representations. Thus,

an order parameter containing $\tau_{1,2}$ matrices and another one containing τ_3 corresponds to different broken symmetries. Therefore, to classify orders by symmetry, we look for an order parameter, O, that contains τ_3 or $\tau_{1,2}$ matrices only, but not a mixture of τ_3 and $\tau_{1,2}$. This gives two possible types of the order parameter with distinct symmetry: $O_1^z = \frac{1}{4}(1 \pm \tau_3)(1 + \boldsymbol{s} \cdot \boldsymbol{m})$ and $O_1^{xy} = \frac{1}{4}(1 + \gamma_1\tau_1 + \gamma_2\tau_2)(1 + \boldsymbol{s} \cdot \boldsymbol{m})$. Here, $\boldsymbol{m}$ is an arbitrary vector determining the spin direction, and (γ_1, γ_2) is an arbitrary normalized real-valued vector.

The order O_1^z represents a valley imbalance order, which transforms under $A_{2,\Gamma}$ and thus, features a breakdown of the mirror symmetry that swaps the two valleys. The second order parameter, O_1^{xy}, corresponds to the intervalley coherent order that transforms under $E_{\pm K}$. It breaks the three-fold rotation, reflection, and translation symmetries of the original problem, Eq.(2). This aspect clearly differentiates the AB bilayer graphene from the case of ABC trilayer: in the latter, the intervalley coherent state does not break the C_3 rotation symmetry[33, 34]. The symmetry classification of possible orders in AB bilayer graphene is summarized in Table.2.2.

Our symmetry analysis allows us to identify two observables that distinguish the valley imbalance and intervalley coherent orders in phase 1. These are anisotropy of conductivity and a spatial charge density wave modulation. For valley imbalance order O_1^z, neither rotation nor translation symmetry of the space group is broken, so the conductivity is isotropic and there is no spatial pattern. In comparison, for the valley coherence order O_1^{xy}, both rotation and translation symmetries are broken. The broken rotation symmetry leads to an anisotropic conductivity, whereas the broken translation symmetry leads to a spatial pattern with momentum $2K$, i.e. a Kekulé charge density wave. On a different note, temporal symmetry can be probed by Hall conductance. For the valley imbalance order O_1^z where time-reversal symmetry is broken, the Hall conductivity is nonvanishing. In comparison, the intervalley coherent order O_1^{xy} preserves time-reversal symmetry, guaranteeing a vanishing Hall conductance. These observables are summarized in the last three rows in Table 2.2.

2.4 Momentum-polarized order: the three-pocket model

Next, we turn to discuss momentum-polarized ordered states that are unique to BBG. These orders are triggered by the Lifshits transition in which an isospin-polarized Fermi sea splits into several distinct pockets centered around the minima of the conduction band. Following this transition, exchange interactions drive symmetry breaking between different pockets through momentum polarization instability.

It is instructive to start with a qualitative discussion of how this instability comes into play. There is an anisotropy in a realistic BBG bandstructure at small momenta due to the trigonal warping term, which is not included in the minimal description of band structure Eq. (2.2). This anisotropy leads to a three-pocket shape of the Fermi surface in the regime of extremely low carrier density. As a result, for each isospin, instead of uniformly filling all three pockets, there are three candidate electron configurations for the ground state, in which either one, two, or all three pockets are filled. Which one wins is determined by the competition between the kinetic and the exchange energy. The kinetic energy favors the configuration where all pockets are uniformly filled, whereas the exchange energy is optimized when all electrons are placed in the same pocket since the interpocket exchange interaction is weaker than the intrapocket one.

To estimate of the energy scales that govern this competition, we consider the total single-particle kinetic energy for all carriers polarized in one pocket:

$$E_{\text{kin}} \sim n^2/2\nu_*, \tag{2.14}$$

where $\nu_* \sim 5 \times 10^{-5}$ meV^{-1} nm^{-2} is the density of states at the bottom of a single pocket, obtained using the pocket dispersion parameters estimated below. To study the pocket order, we take into account the momentum dependence of the interaction. Then the exchange energy is:

$$E_{\text{ex}} \sim -\frac{2\pi e^2}{\kappa|p|}n^2 \sim -\frac{\sqrt{\pi}}{\kappa}e^2 n^{3/2}, \quad |p| \sim \sqrt{4\pi n}, \tag{2.15}$$

with the characteristic momentum scale estimated from particle spacing. As a result, the exchange energy dominates at sufficiently small density $n \lesssim n_* = \frac{4\pi}{\kappa^2} e^4 \nu_*^2 \sim 10^{11}$ cm^{-2}, where we have used a realistic value $D \sim 100$ meV and the dielectric constant $\kappa \sim 5$. The κ value was taken to be close to the "intrinsic" dielectric constant in monolayer graphene arising due to intraband polarization in the Dirac band. The realistic κ values will be somewhat larger and may depend on the substrate and other details of the experimental setup.

The resulting phase diagram in the small density regime is shown in Fig. 2-1 b). At the lowest carrier density, exchange energy dominates and all electrons prefer to polarize in a single pocket. Upon carrier density increasing, the system undergoes phase transitions, first to a two-pocket configuration, and then to a three-pocket (unpolarized) phase. For illustration, in Fig. 2-1 b), we set the dielectric constant to be $\kappa = 3$, so that the phase diagram showcases all possible phases. The details of the phase diagram observed in the experiment may vary from system to system since the competition of pocket orders is sensitive to screening effects that depend on the experimental setup. If screening is made stronger [e.g. by a proximal gate], the pocket-ordered state will be suppressed compared to that shown in Fig. 2-1 b). Alternatively, if the screening is made weaker, the pocket-polarized phase will expand, taking over a larger part of the phase diagram. We note that the energy difference between the pocket polarized and unpolarized states is of the order of 0.1meV to 1meV per carrier, yielding a readily accessible ordering temperature scale of a few kelvins.

We end this section by detailing the procedure through which we extract the parameters k_* and m_* used in the three-pocket model by starting from the realistic BG band structure. As we only care about the band dispersion near the band minima, we model the three-pocket band structure using three isotropic parabolic bands:

$$H_\alpha(\boldsymbol{p}) = \frac{(\boldsymbol{p} - \boldsymbol{k}_\alpha)^2}{2m_*}, \quad \alpha = 1, 2, 3. \tag{2.16}$$

Here α labels the pockets, $\boldsymbol{k}'_\alpha s$ are the centers of pockets, corresponding to three

minima of the conduction band:

$$\boldsymbol{k}_1 = k_*(0,1), \quad \boldsymbol{k}_{2,3} = k_* \left(\mp \frac{\sqrt{3}}{2}, -\frac{1}{2} \right). \tag{2.17}$$

The values of k_* and m_* will be specified below.

In order to relate the three-pocket bandstructure represented by three parabolas to the single-particle bandstructure shown before, we first adopt a minimal model that possesses the pockets at a large displacement field D. This model is described by the Hamiltonian

$$H_{3-p}^{min} = \sum_{\boldsymbol{p}} \psi_{i\boldsymbol{p}}^{\dagger} \left[h_0(\boldsymbol{p}) + h_t(\boldsymbol{p}) + h_{D'}(\boldsymbol{p}) \right]_{ij} \psi_{j\boldsymbol{p}} \tag{2.18}$$

Here i labels isospin, the term $h_{D'}$ is responsible for the Mexican-hat shape dispersion. We find the value of k_* by neglecting the trigonal warping term:

$$k_*(D) \approx \tilde{p} \frac{D}{\tilde{E}}, \quad \tilde{E} = \frac{\tilde{p}^2}{2m} \approx 0.2 \text{ eV}, \tag{2.19}$$

The trigonal warping determines the positions of the three minima of the conduction band but has a negligible effect on the radial coordinate of these minima.

The mass m_* is a parameter that we introduced in the three-pocket toy model to mimic the bottom of the conduction band from (2.18). The Hamiltonian Eq.(2.18) near one of the minimums takes the following form

$$H(\boldsymbol{k}_1 + \delta\boldsymbol{p}) = \frac{\delta p_x^2}{2m_{*\perp}} + \frac{\delta p_y^2}{2m_{*\parallel}}, \tag{2.20}$$

We find that the effective mass in radial direction $m_{*\parallel}$ is determined mainly by h_D, whereas the perpendicular mass $m_{*\perp}$ is only finite when we include the trigonal warping term:

$$m_{*\parallel} \approx \frac{m\tilde{E}}{4D}, \quad m_{*\perp} \approx \frac{\tilde{p}}{6v_3}. \tag{2.21}$$

In our three-pocket toy model Eq.(2.16), we set the parameter m_* as

$$m_* = \sqrt{m_{*\perp} m_{*\parallel}}. \tag{2.22}$$

so that the three-pocket model reproduces the density of states of the realistic band structure.

2.5 Stoner instability in the pocket channel. Phase diagram.

Using the three-pocket model, we proceed to analyze the instability toward the momentum-polarized state and obtain a phase diagram. For clarity, we focus on the effects arising in phase 1 [see Fig.2-1], where the additional effects of densities in different isospin states is absent. There are three possible candidate ground states in which electrons fill up one, two or all three pockets. To determine which one of them is the true ground state, we compare their energies E_N ($N = 1, 2, 3$ is the number of occupied pockets) at the same total carrier density n. Their energies $E_N = E_K^{(N)} + E_{ex}^{(N)}$ consist of kinetic and exchange energy contributions. Using the fact that the density of states in each pocket is a constant $\nu_* = m_*/2\pi$, we can write the total kinetic energy as

$$E_K^{(N)} = \frac{N}{2\nu_*}\frac{n^2}{N^2} = \frac{\pi n^2}{N m_*} \tag{2.23}$$

In order to explore the pocket polarization, we restore the momentum dependence of the interaction in the exchange part of the free energy:

$$E_{ex}^{(N)} = -\frac{1}{2}\sum_{i,j=1}^{N}\sum_{\boldsymbol{p},\boldsymbol{p}'} V_{p-p'} n_{i\boldsymbol{p}} n_{j\boldsymbol{p}'}, \quad V_{\boldsymbol{p}-\boldsymbol{p}'} = \frac{2\pi e^2}{\kappa|\boldsymbol{p}-\boldsymbol{p}'|}, \tag{2.24}$$

where $n_{i\boldsymbol{p}}$ is the occupation number at momentum $\boldsymbol{p}$ measured relative to the pocket i center. For simplicity, as in Eq.2.15, we use momentum-independent dielectric constant κ. When the carrier density is small, the interpocket exchange interactions

yield a nearly momentum-independent renormalization of the energy of each electron, which justifies approximating the Fermi surfaces in the pockets by discs centered at $\boldsymbol{k}_i$. This yields an estimate for exchange energy

$$E_{ex}^{(N)} = -\sum_{i,j=1}^{N} \sum_{\boldsymbol{p},\boldsymbol{p}'} \frac{1}{2} V_{\boldsymbol{p}-\boldsymbol{p}'+\boldsymbol{k}_{ij}} n_{\boldsymbol{p}} n_{\boldsymbol{p}'}, \tag{2.25}$$

$$V_{\boldsymbol{p}-\boldsymbol{p}'} = \frac{2\pi e^2}{|\boldsymbol{p}-\boldsymbol{p}'|}, \quad n_{\boldsymbol{p}} = 1 - \theta(|p| - p_0). \tag{2.26}$$

where $\boldsymbol{k}_{ij} = \boldsymbol{k}_i - \boldsymbol{k}_j$ are momentum differences between pocket centers, $n_{\boldsymbol{p}}$ is the occupation number of the state with momentum $\boldsymbol{p}$ measured relative to the pocket center $n_{\boldsymbol{p}} = 1 - \theta(|p| - p_0)$. Here p_0 is the radius of the circular Fermi surface in each pocket

$$p_0 = \sqrt{4\pi n/N}. \tag{2.27}$$

With these expressions, the exchange energy can be evaluated analytically by performing the Fourier transform. Namely, perform Fourier transform:

$$V(r) = \frac{e^2}{|r|} = \int \frac{d^2p}{(2\pi)^2} e^{i\boldsymbol{p}\cdot\boldsymbol{r}} V_{\boldsymbol{p}} \tag{2.28}$$

and

$$n(r) = \int \frac{d^2p}{(2\pi)^2} e^{i\boldsymbol{p}\cdot\boldsymbol{r}} n_{\boldsymbol{p}} \tag{2.29}$$

Then, the exchange energy can be written as

$$\begin{aligned} E_{ex}^{(N)} &= -\frac{1}{2} \sum_{ij} \int d^2r V(\boldsymbol{r}) n(\boldsymbol{r})^2 e^{i\boldsymbol{k}_{ij}\cdot\boldsymbol{r}} \\ &= -\frac{1}{2} \sum_{ij} \int_0^\infty V(r) n(r)^2 2\pi J_0(r|\boldsymbol{k}_{ij}|) x dx \end{aligned} \tag{2.30}$$

Here J_0 is the Bessel function. To evaluate this quantity, we need to first work out the form of $n(r)$:

$$n(r) = \int_{|p|<p_0} \frac{dp_x dp_y}{4\pi^2} e^{ip_x r} = \int \frac{dp_x}{2\pi^2} \sqrt{p_0^2 - p_x^2} e^{ip_x r}. \tag{2.31}$$

Passing to polar coordinates, we have

$$n(r) = \frac{p_0^2}{2\pi^2} \int_{-\frac{\pi}{2}}^{\frac{\pi}{2}} d\theta \cos^2\theta e^{iz\sin\theta} \tag{2.32}$$
$$= \frac{p_0^2}{8\pi} \left[J_2(z) + 2J_0(z) + J_{-2}(z)\right] = \frac{p_0^2}{4\pi} \left[J_2(z) + J_0(z)\right]$$

where $z = rp_0$, J_0 and J_2 are Bessel functions. With these expressions, we finally arrive at

$$E_{ex}^{(N)} = -\frac{e^2 p_0^4}{16\pi} \sum_{ij} \int_0^\infty dr \left[J_2(rp_0) + J_0(rp_0)\right]^2 J_0(r|\boldsymbol{k}_{ij}|). \tag{2.33}$$

Our isotropic parabolic bands model for pockets [see Eq.(2.16)] is expected to be accurate when the distance k_* from the pocket centers to K point is much greater than the pocket radius p_0. This yields an upper bound for carrier density: $n \lesssim 0.3 \times 10^{12}$ cm^2, where we used the value of k_* estimated above. As Fig. 2-1 a) indicates, the maximal density in phase 1 always satisfies the above validity condition. We can therefore use the results in Eqs. (2.23),(2.33) to determine the phase diagram by comparing the energies of one-pocket, two-pocket, and three-pocket configurations.

2.6 Momentum-polarized phases: observables and phenomenology

There are several unique observables that can be predicted for the momentum polarized phases. One surprising phenomenon that these phases display is the presence of persistent currents in the ground state, which are allowed by spontaneously-broken time reversal and inversion broken due to the transverse electric field. Such currents will not survive in a spatially uniform system bulk, yet they will show up at boundaries and interfaces. For example, they are expected to occur in the presence of spatial domains in which electrons populate different pockets. This behavior can be understood by parameterizing the momentum polarization using a position-dependent vector $\boldsymbol{u}(\boldsymbol{x})$ as in the mean-field Hamiltonian given in Eq.(2.1). In each domain,

$\boldsymbol{u}(\boldsymbol{x})$ is a uniform vector field aligned with a certain crystal axis. For a uniform $\boldsymbol{u}$, the electric current in equilibrium equals zero since the integral over the Fermi sea of carrier velocities derived from Eq. (2.1) will vanish. However, at a domain wall $\boldsymbol{u}(\boldsymbol{x})$ varies in space and interpolates between different values in the domains. In this case, a nonzero local current is allowed. This argument predicts a contribution to orbital magnetization proportional to the curl of $\boldsymbol{u}(\boldsymbol{x})$:

$$\boldsymbol{m}(\boldsymbol{x}) = \chi \boldsymbol{\nabla} \times \boldsymbol{u}(\boldsymbol{x}), \tag{2.34}$$

where the susceptibility χ is proportional to the Landau diamagnetic susceptibility. Here, terms such as $\boldsymbol{\nabla} \cdot \boldsymbol{u}$ must be excluded since $\boldsymbol{m}$ is an axial vector. Therefore, we expect a nonvanishing magnetization that peaks on the domain boundaries, originating from persistent currents that counter-propagate on the two sides of domain boundaries. The magnetization distribution localized at the domain boundaries is a directly testable signature of persistent currents.

Other interesting observables can arise from broken crystallographic symmetries. Indeed, two possible orders of the "parent" phase, i.e. phase 1, correspond to two kinds of broken symmetries— either breaking only mirror symmetry or breaking rotation, mirror, and translation symmetries (see Table 2.2). If phase 1 only breaks mirror symmetry, then populating one or two out of three pockets will further break the three-fold rotation symmetry without breaking the translation symmetry, leading to electron nematicity. This symmetry breaking can be observed by measuring the anisotropy in the conductivity. If, however, the parent isospin order is intervalley coherent, then the only remaining symmetry to be broken in the pocket-polarization transition is the translation symmetry. Namely, the pocket polarization on top of valley coherent states transforms the Kekulé charge density wave into an incommensurate density wave which carries momentum $\boldsymbol{P}_{i,j'} = 2\boldsymbol{K} + \boldsymbol{k}_i + \boldsymbol{k}_{j'}$, $i, j = 1, 2, 3$, $\boldsymbol{k}_{i'} = -\boldsymbol{k}_i$, see Fig. 2-2 c). In this case, the pocket order can be detected by imaging long-period spatial modulations.

The momentum-polarized pocket orders can also be detected by measuring the

Hall conductivity. When pocket orders occur on top of the valley imbalance order O_1^z which allows a nonvanishing Hall conductivity, the Hall conductivity changes abruptly since the Berry curvature is non-uniform near K point [see Fig. 2-2 d)]. If pocket ordering occurs on top of O_1^{xy} isospin order, which originally respects the time-reversal symmetry, enforcing a vanishing Hall conductivity, then the onset of such a momentum polarization can break the time-reversal symmetry so long as electrons populate different pockets in valleys K and K' [e.g. pocket 1 and $2'$ in Fig. 2-2 c)]. As a result, the Hall conductivity will jump from zero to some finite value at the pocket ordering transition. Therefore, regardless of the form of the parent isospin order, we always expect a discontinuous behavior in Hall conductance at the onset of pocket orders.

Another experimentally accessible signature of the Berry curvature is magnetization due to orbital currents in the ground state of the system. The magnetization can be estimated using the approach described in Refs.[187], giving ~ 4 Bohr magnetons per electron for the parameters used in Fig. 2-2 d) [see Appendix 2.8]. This is a few times larger than the orbital magnetic moments of electrons in a Landau level and is readily measurable.

2.7 Estimating interaction strength

In our analysis of the phase diagram above, we have been using the value of V to represent the strength of exchange interaction. Here, we provide an estimate for this quantity.

The interaction strength used in our model can be taken as the strength of the screened Coulomb interaction at the relevant momentum, which is Fermi momentum p_0. This gives an estimate

$$V = \tilde{V}_{p_0}. \tag{2.35}$$

Accounting for Thomas-Fermi screening, the screened Coulomb potential takes the

following form

$$\tilde{V}_{p_0} = \frac{V_{p_0}}{1 + V_{p_0}\Pi_{p_0}}, \tag{2.36}$$

where Π_{p_0} is the polarization function at Fermi momentum. We estimate this quantity using the value of density of states at Fermi surface ν_0. When the band is flat compared to the interaction energy, which is the case of interest, we have

$$\nu_0 V_{p_0} \gg 1. \tag{2.37}$$

In this regime, the screened Coulomb interaction is approximately given by

$$\tilde{V}_{p_0} = \frac{1}{\nu_0}. \tag{2.38}$$

Therefore, we can estimate the interaction as

$$V \sim \frac{1}{\nu_0} \sim 10^3 \text{ meV nm}^2 \tag{2.39}$$

where we have used $\nu_0 \sim n/W \sim 10^{-3}$ meV nm^{-2}, where n is the carrier density $n \sim 10^{12}$ cm^{-2}, $W \sim 10\,$meV is the Fermi energy measured from the band bottom at this carrier density.

2.8 The Berry curvature and orbital magnetization

It is straightforward to compute the Berry curvature using the Hamiltonian Eq. (2.18). Here we consider the Berry curvature for a realistic BG model and obtain the result of Fig.2-2. We take the form of the Hamiltonian projected to conduction band in Eq. (2.18), and rewrite it as

$$H_{3-p}^{min} = \sum_{\boldsymbol{p}} \psi_{i\boldsymbol{p}}^{\dagger} \boldsymbol{h}(\boldsymbol{p}) \cdot \boldsymbol{\tau}_{ij} \psi_{j\boldsymbol{p}}, \tag{2.40}$$

$$\boldsymbol{h}(p) \cdot \boldsymbol{\tau} = h_0(\boldsymbol{p}) + h_t(\boldsymbol{p}) + h_{D'}(\boldsymbol{p}) \tag{2.41}$$

where $\boldsymbol{\tau} = (\tau_1, \tau_2, \tau_3)$. Then the Berry curvature is given by

$$\Omega_{\boldsymbol{p}} = \frac{1}{2}\frac{\boldsymbol{h}}{|\boldsymbol{h}|} \cdot \left(\frac{\partial \boldsymbol{h}(\boldsymbol{p})}{\partial p_1} \times \frac{\partial \boldsymbol{h}(\boldsymbol{p})}{\partial p_2} \right). \tag{2.42}$$

In main text Fig.2-2 we use Eq.(2.42) to numerically compute the Berry curvature.

Next, we estimate the orbital magnetization which arises from Berry curvature. Below, we recall the derivation of orbital moment described in Ref. [187], and apply it to our problem. As an estimate, here we only consider the contribution to the orbital magnetization due to the center-of-mass motion of electrons. The true orbital magnetization also includes a contribution due to the self-rotation effect. That, however, does not change the order of magnitude of the magnetization.

As a starting point, we consider the current flowing along the sample boundary, treating it as an anomalous current arising due to Berry's curvature and driven by the filed due to spatially varying trapping potential U. This gives the current

$$I = e \int dx n(x) v(x) \tag{2.43}$$

$$= e \int dx \int \frac{d^2p}{(2\pi)^2} \Omega_{\boldsymbol{p}} f(\epsilon_{\boldsymbol{p}} - \mu + U) \frac{\partial U}{\partial x} \tag{2.44}$$

where x is the coordinate in the direction normal to the boundary. The magnetization per unit area is therefore given by

$$M = \frac{IA}{A} = e \int_0^{\tilde{\mu}} \Omega_{FS}(\tilde{\mu} - U) dU, \tag{2.45}$$

$$\Omega_{FS}(E) = \int \frac{d^2p}{(2\pi)^2} \Omega_{\boldsymbol{p}} f(\epsilon_{\boldsymbol{p}} - E) \tag{2.46}$$

To estimate the magnetization value, we apply Eq. (2.46) to the three-pocket model used in the main text, taking Ω_p as a constant $\Omega_p \sim \Omega$ within the Fermi sea. This gives

$$\frac{M}{\mu_B} \approx \frac{N m_* m_{\mathrm{e}} \Omega \tilde{\mu}^2}{2\pi}. \tag{2.47}$$

where μ_B is the Bohr magneton, m_{e} is the electron mass, N is the number of pockets

that are filled, $\tilde{\mu}$ is Fermi level measured from the bottom of the band. We estimate M for the case shown in Fig.2-2, where $N = 3$, $\tilde{\mu} = 10$ meV, and $\Omega \sim 15$ nm^2 [extracted from Fig. 2-2], we find

$$\frac{M}{\mu_B} \sim 4 \times 10^{-3} \text{nm}^{-2} \sim 4n \tag{2.48}$$

where we used electron density $n = 10^{11}$ cm^{-2}, a value corresponding to the regime where pocket polarization is expected. This predicts a sizable orbital magnetic moment of ~ 4 Bohr magnetons per conduction electron.

2.9 Summary for Chapter 2

The above analysis demonstrates that exchange interactions in the flattened BBG bands result in a cascade of isospin-polarized orders and momentum-polarized orders. These orders are of interest for a number of reasons, in particular, because they feature persistent currents and magnetization in the ground state. We stress that this phenomenon is distinct from orbital magnetization familiar in topological bands where it arises due to the Berry phase. The momentum-polarized orders, rather than merely providing additional symmetry-breaking options by extending 4 isospin species to 12 isospin and pocket species, lead to unique physical properties such as nematic order with broken time reversal, persistent currents, and Hall conductivity. Momentum polarization results in abrupt changes of the Berry curvature seen by electrons, leading to jumps in the anomalous Hall conductivity and orbital magnetization that can provide a convenient diagnostic of momentum polarization orders.

Chapter 3

Chiral interaction and skyrmions

3.1 Introduction

This Chapter starts the discussion of the interplay between the k-space Berry curvature and Stoner magnetism. As discussed in the Introduction, there are two primary classes of interest in graphene-based narrow-band systems. One is moiré graphene[3, 21, 22, 24, 204, 184, 146]. Another is non-moiré graphene that hosts flat bands, such as field-biased Bernal bilayers and rhombohedral trilayers [202, 203, 201, 150, 35]. New exotic orders appear when the moiré twist angle is tuned to a magic value [15] or when bands are flattened by a transverse electric field [110]. The richness of the observed orders, which include isopsin (spin and valley) polarized phases coexisting with insulating and superconducting phases, motivates seeking new exotic orders.

Of special interest are the chiral itinerant magnetic phases, wherein spins wrap around the Bloch sphere, spanning a solid angle. Chiral spin textures have been explored in various magnetic systems[126, 48]. Famously, the Dzialoshinskii-Moriya (DM) coupling favors spin textures[17] such as helical spin density waves [14, 127, 82] and skyrmions—the seminal topologically-protected particle-like spin configurations[142]. Is it possible to achieve a chiral spin order in graphene-based systems? At first sight, this may seem problematic as staple interactions that stabilize chiral magnetic orders are absent or extremely weak in graphene. Indeed, in noncentrosymmetric magnets—the bulk chiral magnetic metals[143, 121, 130, 193, 151, 149] and mag-

netic layers[68, 75]—skyrmions are stabilized by the DM coupling governed by the microscopic spin-orbit interactions (SOI)[17, 48]. However, the microscopic SOI in graphene is usually negligible compared to other energy scales[129]. Likewise, the mechanisms that utilize frustration[138, 95, 67] are not found in graphene systems.

In this paper, we address this challenge by demonstrating a new mechanism that favors chiral spin orders. Namely, we show that chiral interactions that can drive chiral spin orders are naturally present in interacting electronic systems with bands that are equipped with Berry curvature. Unlike the mechanisms studied before, our chiral interactions do not require any extra broken symmetries, microscopic SOI or frustrations. The results of this Chapter have been published in Ref.[40]

Specifically we argue that the exchange interaction in Dirac bands such as those found in graphene multilayers, moiré [162, 15, 3] and non-moiré[110, 27], results in a chiral interaction which leads to Stoner instability towards chiral ordered states. Fig.3-1 illustrates this for a quadratic Dirac band model of a field-biased bilayer graphene (BBG). The chiral interaction that drives this ordering arises from orbital magnetization due to k-space Berry curvature of Dirac carriers. This interaction occurs in the presence of a position-dependent spin polarization, taking the form:

$$\delta F = \int d^2x \sum_i -(M_{i,+} - M_{i,-})B_i(\boldsymbol{x}), \tag{3.1}$$

where $M_{i,\pm}$ is the orbital magnetization of the majority-spin and minority-spin carriers (see Eq.(3.10)). The quantity $B_i(\boldsymbol{x})$ is defined as the topological density of spin texture multiplied by the flux quantum ϕ_0:

$$B_i(\boldsymbol{x}) = \frac{\phi_0}{4\pi}\boldsymbol{S}_i \cdot (\partial_1 \boldsymbol{S}_i \times \partial_2 \boldsymbol{S}_i), \quad \phi_0 = hc/e, \tag{3.2}$$

where $\boldsymbol{S}_i(x)$ is the unit-vector field representing spin polarization of carriers in valleys $i = K, K'$. The quantity $B_i(\boldsymbol{x})$ represents a 'magnetic field' associated with the spin-dependent (chiral) Aharonov-Bohm effect.

The key aspect of the chiral interaction, Eq.(3.1), is that the position-dependent

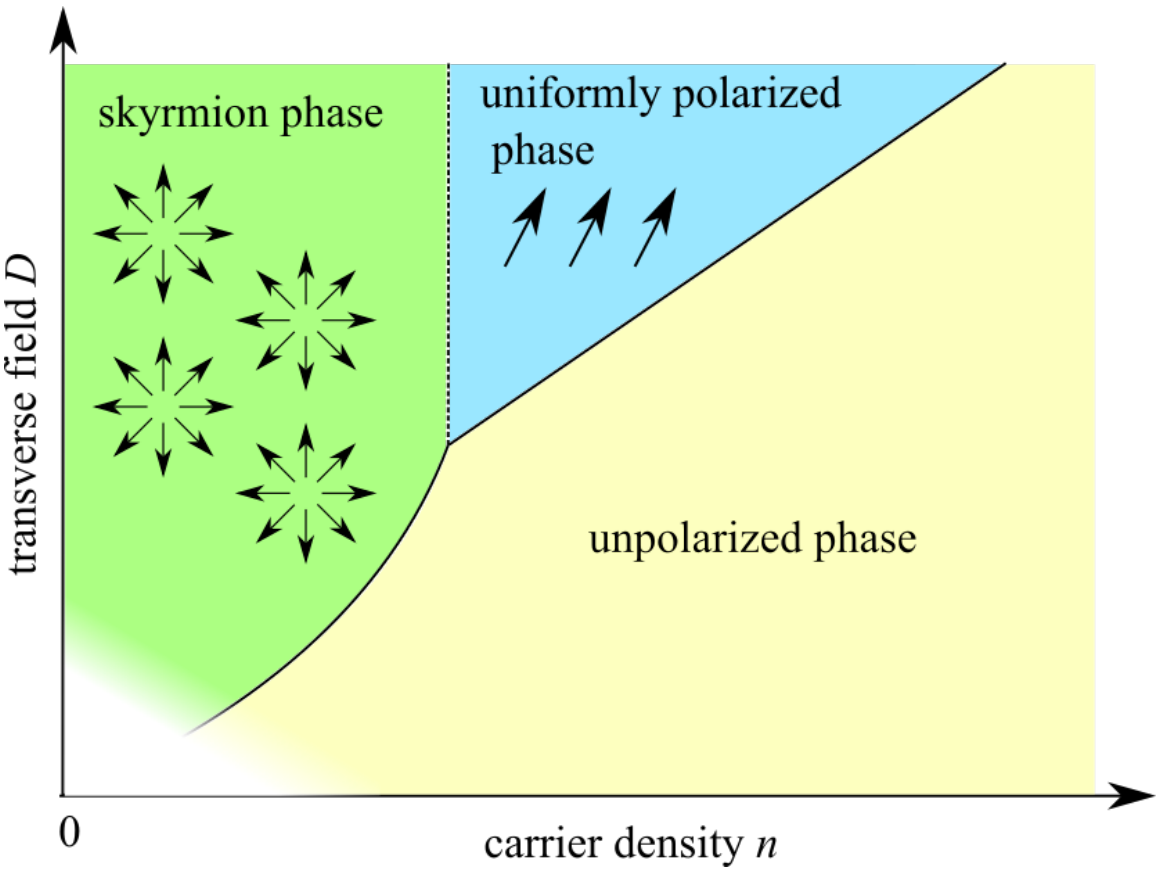

Figure 3-1: The mean-field phase diagram for chiral magnetic order in the quadratic Dirac model, Eqs.(3.3) and (3.4), away from charge neutrality at $D = 0$. Transition between uniformly spin-polarized and unpolarized phases is first-order, occurring on a straight line in the n-D plane given by Eq.(3.16). Transition between skyrmion phase and uniformly polarized phase is second-order, with skyrmion density vanishing at the phase boundary given by Eq.(3.24). Here we ignore valley ordering, focusing on spin polarization in one valley (see text).

quantization axis along which carrier spins are polarized is, in general, allowed to twist in space. Eq.(3.1), derived below, can be viewed as an extension of the basic electromagnetic coupling of a magnetic moment and external field, $E = -\boldsymbol{M} \cdot \boldsymbol{B}$.

Since M_i describes orbital magnetization whereas B_i is a property of spin texture, the interaction in Eq.3.1 resembles the atomic spin-orbital interaction (SOI) $E \sim \boldsymbol{L}\cdot\boldsymbol{S}$. Yet, the interaction in Eq.3.1 is of a totally different origin, governed by the interplay of momentum-space Berry curvature and exchange interaction, not relying on spin-orbital coupling. It therefore has unique symmetry properties distinct from those of SOI: the quantities B_i are invariant under the $SU(2)$ spin rotations performed separately in each valley, which leave the orbital quantities $M_{i,\pm}$ intact. As discussed below, the interaction in Eq.3.1 also respects discrete symmetries of BBG, including the time-reversal and mirror symmetries.

3.2 Chiral interaction

We note that the chiral interaction that drives skyrmions in our theory is essentially different from the one described in recent works, where skyrmions in isospin-polarized moiré graphene flat bands have been invoked to predict exotic superconductivity [19, 84]. The mechanism that stabilizes skyrmions in these papers is an isospin extension of quantum Hall ferromagnet physics, in which the skyrmion emerge in Landau levels spin-split by exchange interactions [160, 102, 49, 126]. Skyrmions of this type have been predicted [192, 133] and recently observed [200, 100] in graphene at high magnetic fields.

Next, we derive the interaction between spin-chirality and orbital magnetization, Eq.(3.1), by a microscopic analysis starting from a fully SU(2)-invariant Hamiltonian not involving SOI. To that end, we consider Stoner magnetism of Dirac fermions with spin-exchange coupling

$$\mathcal{H} = \sum_p c_p^\dagger H(p) c_p - \frac{1}{2}\sum_{\boldsymbol{x},\boldsymbol{x}'} U(\boldsymbol{x}-\boldsymbol{x}') : s_\alpha(x) s_\alpha(x') :, \tag{3.3}$$

where the last term is an exchange interaction written in terms of spin density $s_\alpha(x) = \psi^\dagger(x)\sigma_\alpha\psi(x)$ with Pauli matrices σ_α representing ordinary spin-1/2 variables, $\alpha = 1, 2, 3$. The density-density interaction $e^2/\kappa|r - r'|$, which generates the exchange interaction on a microscale, is suppressed for conciseness. Its role will be discussed below. Here we will use a toy-model form of exchange coupling $U(\boldsymbol{x} - \boldsymbol{x}') = 2\pi U_0\xi^{-2}e^{-(\boldsymbol{x}-\boldsymbol{x}')^2/2\xi^2}$, normalized so that $\int d^2xU(\boldsymbol{x}) = U_0$. The Dirac band is described by a general 2×2 Dirac Hamiltonian in the sublattice A, B basis. Here we consider the quadratic Dirac problem

$$H(p) = \begin{pmatrix} D & \frac{(p_1 - i\eta p_2)^2}{2m} \\ \frac{(p_1 + i\eta p_2)^2}{2m} & -D \end{pmatrix} \tag{3.4}$$

with $\eta = \pm 1$ for the valleys K and K', respectively. Accordingly, the quantities $\psi(x)$, $\psi^\dagger(x)$, c_p, $c_p^\dagger$ are spinors with the A and B sublattice components and the ordinary spin-1/2 components. The Hamiltonian $H(p)$ is particle-hole symmetric, with the terms producing particle-hole asymmetry and trigonal warping ignored for simplicity. Incorporating these terms later or generalizing to other Dirac band types would be straightforward. Realistic parameter values are discussed beneath Eq.(3.24).

To describe spin textures, we perform a mean-field analysis in which the field describing magnetic order is allowed to vary in space. Since the exchange interactions are predominantly intravalley it will be sufficient to carry out the analysis for an individual valley and consider the role of valley degrees of freedom later. The Hubbard-Stratonovich (HS) transformation is carried out using an ordering field $\boldsymbol{h}(\boldsymbol{x})$ with both the modulus and orientation being position-dependent, $e^{\int dt \sum_k \frac{U(k)}{2} \boldsymbol{s}_k \cdot \boldsymbol{s}_{-k}} = \int D[\boldsymbol{h}] e^{\int dt \sum_k \boldsymbol{h}_k(t)\cdot\boldsymbol{s}_{-k} - \frac{\boldsymbol{h}_k(t)\boldsymbol{h}_{-k}(t)}{2U(k)}}$, where $D[\boldsymbol{h}] = \prod_{k,t} d\boldsymbol{h}_k(t)$. Here we introduced Fourier harmonics of the HS field, the spin density and the interaction $\boldsymbol{h}_k = \int d^2x \boldsymbol{h}(x)e^{-i\boldsymbol{k}\boldsymbol{x}}$, $\boldsymbol{s}_k = \int d^2x \boldsymbol{s}(x)e^{-i\boldsymbol{k}\boldsymbol{x}}$, $U(k) = \int d^2xU(x)e^{-i\boldsymbol{k}\boldsymbol{x}} = U_0e^{-k^2\xi^2/2}$. Integrating out fermions and assuming a time-independent $\boldsymbol{h}(x)$, we obtain the free energy with a nonlocal

$h(x)h(x')$ interaction

$$F = \text{Tr}\,\log\left[i\omega - H(p) - h_\alpha(x)\sigma_\alpha\right] + \sum_k \frac{\boldsymbol{h}_k \boldsymbol{h}_{-k}}{2U(k)}, \tag{3.5}$$

where, for conciseness, the chemical potential μ is incorporated in H and Tr denotes $\sum_x \int \frac{d\omega d^2p}{(2\pi)^3}\,\text{Tr}_{\,2\times 2}$. In this case, it is easy to compare the states with uniform polarization and those with spatially dependent $\boldsymbol{h}(\boldsymbol{x})$ on equal footing. The saddle point condition yields a time-independent $h = |\boldsymbol{h}|$, which is nothing but the Stoner mean field value

$$h = U_0(n_+ - n_-)/2, \tag{3.6}$$

where n_+ and n_- are local densities of carriers with spins parallel and antiparallel to local spin quantization axis $\boldsymbol{h}(x)$. We will call these spin species the majority and the minority spins, respectively. When the system is fully polarized, the mean field equals $h = U_0 n/2$. The term $-h_\alpha(x)\sigma_\alpha$ describes electron spins coupled to a spin texture with a position-dependent magnetization polarized along the unit vector $\boldsymbol{S}(x) = \boldsymbol{h}(x)/h$, where $|\boldsymbol{h}(x)| = h$.

Accordingly, we consider the last term in free energy [Eq.(3.5)] $F_h = \sum_k \frac{\boldsymbol{h}_k \cdot \boldsymbol{h}_{-k}}{2U(k)}$ assuming that the local spin-quantization axis is slowly-varying, $\xi\partial_\mu S_\alpha \ll 1$. Assuming that the exchange interaction radius ξ exceeds the Fermi wavelength, which makes the short-wavelength fluctuations in $\boldsymbol{h}(x)$ weak, we can approximate $U(k)^{-1} = U_0^{-1}(1 + k^2\xi^2/2)$, giving

$$F_h = \sum_k \frac{\boldsymbol{h}_k \cdot \boldsymbol{h}_{-k}}{2U(k)} \approx \sum_x \frac{h^2}{2U_0} + \frac{1}{2} J(\partial_\mu S_\alpha)^2, \tag{3.7}$$

with the spin stiffness parameter defined as $J = \frac{\xi^2 h^2}{2U_0}$.

Next, we introduce a gauge field describing Berry phase for electrons in the presence of a slowly varying spin texture[12, 183, 148, 72]. This is done by carrying out spin rotation at every point in position space, $|\boldsymbol{S}(x)\pm\rangle = U_{\boldsymbol{S}(x)}\,|\boldsymbol{z}\pm\rangle$, such that

$\boldsymbol{h}_\alpha \sigma_\alpha = U^\dagger_{\boldsymbol{S}(x)} h\sigma_3 U_{\boldsymbol{S}(x)}$. Absorbing μ in $H(p)$, we have

$$F = \int d^2x \sum_{\omega,p} \text{Tr } \log\left[i\omega - H(\boldsymbol{p} - \boldsymbol{a}\sigma_3) - h\sigma_3\right] + F_h \tag{3.8}$$

where F_h is defined in Eq.(3.7). The gauge field $\boldsymbol{a}$ describing position-dependent spin rotation is defined as $a_\mu(x) = -\frac{i}{2}\,\text{Tr}\,(\sigma_z U^{-1}_{\boldsymbol{S}(x)} \partial_\mu U_{\boldsymbol{S}(x)})$ [136, 53, 65]. The quantity $\nabla \times \boldsymbol{a}$ is nothing but the spin chirality density, since

$$\nabla \times \boldsymbol{a} = \frac{1}{2}\epsilon_{\mu\nu} \boldsymbol{S} \cdot (\partial_\mu \boldsymbol{S} \times \partial_\nu \boldsymbol{S}). \tag{3.9}$$

This relation links the skyrmion topological density and the pseudomagnetic field, Eq.(3.2). For a derivation of this result, which follows closely previous literature, see Appendix.

We are interested in the instability of a spatially-uniform magnetic order towards a twisted state with a nonzero gauge field $\boldsymbol{a}$. We therefore consider power-series expansion of the electronic energy in Eq.(3.8) in small $\boldsymbol{a}$. We neglect the longitudinal fluctuations of $\boldsymbol{h}$, which are gapped, focusing on the soft angular fluctuations, $\delta\boldsymbol{h}(\boldsymbol{x}) \perp \boldsymbol{h}$. For a slowly varying unit-vector field $\boldsymbol{S}(\boldsymbol{x}) = \boldsymbol{h}/|\boldsymbol{h}|$, the dependence on $\boldsymbol{a}$ in the first term of Eq.(3.8), hereafter referred to as F_1, can be found by an expansion in powers of $\boldsymbol{a}$. At order $\boldsymbol{a}^2$ we have

$$\begin{aligned} F_1 &= \sum_{\pm} E_\pm - \Delta M B + \frac{1}{2}\chi B^2, \quad \Delta M = M_+ - M_-, \\ E_\pm &= \sum_k (\epsilon^\pm_k - \mu) f(\epsilon^\pm_k), \quad \chi = \chi_+ + \chi_-. \end{aligned} \tag{3.10}$$

where the quantities $M_\pm$ and $\chi_\pm$ are the orbital magnetizations and the Landau diamagnetic susceptibility of the majority and minority spins, $B(\boldsymbol{x}) = \frac{e}{\hbar}\nabla \times \boldsymbol{a}$ is the pseudo magnetic field. Using the relation in Eq.(3.9), it is straightforward to show that B defined in this way is identical to B given in Eq.(3.2). The $E_\pm$ contributions are the energies of spin-majority and spin-minority fermions in the bands with an exchange spin splitting, $\epsilon^s_k = \epsilon_k \mp h$, evaluated at $\boldsymbol{a} = 0$, whereas the second and

third terms represent the dependence on the pseudomagnetic field $\nabla \times \boldsymbol{a}$ at second order in $\boldsymbol{a}$.

The contributions $\mp M_{\pm} B$ describe orbital magnetization of spin-majority and spin-minority carriers, arising due to Berry curvature, coupled to the pseudomagnetic field. Crucially, both the conduction and valence bands contribute to M. Therefore, perhaps counterintuitively, both up-spin and down-spin contributions to M matter even if the conduction band is fully polarized. The values $M_{\pm}$ depend on the band filling and will be discussed below. The sign $\mp$ accounts for the fact that the Berry phase for the carriers with opposite spins, moving in a slowly varying texture $\boldsymbol{h}(x)$, has opposite signs, described by the σ_3 factor in Eq.(3.8). In this form, Eq.(3.8) describes the limit of a weak, non-quantizing pseudomagnetic field B, which is sufficient for the purpose of analyzing the transition from zero to nonzero B.

Putting everything together, we can write the system energy in the absence of pseudo magnetic field B as

$$F = \int d^2x \left[E_+ + E_- + \frac{h^2}{2U_0} + \frac{J}{2}(\partial_\mu \boldsymbol{S})^2 \right] \tag{3.11}$$

Using this expression, we can seek the ground state by comparing the energies of the ordered and disorder states. To account for the effect of a long-range $1/r$ density-density interaction without incorporating it explicitly in the mean-field analysis, we consider different states at the same total carrier density n. This approach is valid due to the large charging energy values $E_c = \frac{1}{2} V_0 n^2$ which typically exceed other energy scales in the system. When E_c is included in the analysis, the dependence of the total energy on n is dominated by the following terms:

$$\frac{V_0 n^2}{2} - \mu n = \frac{V_0}{2} \left(n - \frac{\mu}{V_0} \right)^2 - \frac{\mu^2}{2V_0} \tag{3.12}$$

These terms pin the density to $n = \frac{\mu}{V_0}$ regardless of the order type. Therefore, comparing energies of different states at the same μ in the presence of E_c is equivalent to comparing their energies at the same n.

To analyze the ordering described by Eq.(3.11) we proceed in two steps: First

analyze the Stoner instability while temporarily ignoring B . Next, we consider the dependence on B and the transition from a uniform magnetic order to a twisting order.

In the absence of B, Eq.(3.11) describes the standard Stoner instability—a transition from a disordered state to a uniformly polarized state. Since the density of states in the quadratic Dirac band monotonically decreases as a function of energy, the ground state configuration is either fully spin polarized or spin unpolarized, depending on the band parameters and interaction strength. [For a more general band dispersion partial spin polarization can also occur.] The energy density of a fully polarized phase where $n_+ = n, n_- = 0$ is given by

$$F_{\rm fp} = E_{\rm tot}(n) - \frac{U_0 n^2}{2} \tag{3.13}$$

where n is a given total carrier density. We have used Eq.(3.6) . Here $E_{\rm tot}(n) = \int_0^{\sqrt{4\pi n}} \frac{d^2k}{4\pi^2}\epsilon_k$ represents the total kinetic energy of electrons of density n in one spin one valley in the absence of interaction. Similarly, the energy of unpolarized state where $n_+ = n_- = n/2$ is given by

$$F_{\rm unp} = 2E_{\rm tot}(n/2) \tag{3.14}$$

Here, we have used $h = 0$ in unpolarized phase. For our quadratic Dirac band, $E_{\rm tot}$ takes the following form:

$$E_{\rm tot}(n) = \frac{mD^2}{4\pi}\left(\log(x + \sqrt{1+x^2}) + x\sqrt{1+x^2}\right), \tag{3.15}$$

where $x = \frac{2\pi n}{mD}$ is a dimensionless density parameter. The regime of interest is that of strong exchange interaction, which corresponds to low values $n \ll 2mD$. In this case, we can use power-series expansion $E_{\rm tot}(n) = \frac{mD^2}{2\pi}(x + \frac{5}{12}x^3 + ...)$. This allows a direct comparison of the energies of polarized and unpolarized states. Simple algebra

then predicts the fully polarized state to win when

$$\frac{n}{D} < \frac{2m^2 U_0}{5\pi^2}. \tag{3.16}$$

Therefore, the phase boundary is a straight line on the D-n phase diagram (see Fig.3-1). This phase transition is first-ordered since the full polarization occurs abruptly.

Next, we consider the role of a spin texture $\boldsymbol{S}(\boldsymbol{x})$ and derive the condition for skyrmion proliferation. From Eqs.(3.10),(3.11), we see that system energy depends on $\boldsymbol{S}$ as $E_{\boldsymbol{S}} = \int d^2x \left[\frac{J}{2}(\partial_\mu S_\alpha)^2 \mp \Delta M B + \frac{\chi}{2}B^2\right]$. Therefore, the spin texture enters the energetics in two ways: through pseudo magnetic field B which is proportional to the spin chirality density Eq.(3.9), and also through the spin stiffness energy $\frac{1}{2}J(\partial_\mu \boldsymbol{S})^2$. However, the latter contribution has a lower bound associated with spin chirality

$$\frac{1}{2}\int d^2x(\partial_\mu \boldsymbol{S})^2 \geq \frac{1}{2}\int d^2x|\epsilon_{\mu\nu}\boldsymbol{S}\cdot(\partial_\mu \boldsymbol{S}\times\partial_\nu \boldsymbol{S})|.$$

This relation follows from the well-known identity[142]:

$$\int d^2x \left[(\partial_\mu \boldsymbol{S})^2 \mp \epsilon_{\mu\nu}\boldsymbol{S}\cdot(\partial_\mu \boldsymbol{S}\times\partial_\nu \boldsymbol{S})\right] \tag{3.17}$$

$$= \frac{1}{2}\int d^2x(\partial_\mu \boldsymbol{S} \pm \epsilon_{\mu\nu}\boldsymbol{S}\times\partial_\nu \boldsymbol{S})^2 \geq 0, \tag{3.18}$$

Expressing the stiffness energy through $|B|$ gives

$$E_{\boldsymbol{S}}[B] = \int d^2x \left[-\Delta M B + \frac{2Je}{\hbar c}|B| + \frac{\chi}{2}B^2\right], \tag{3.19}$$

Obviously, the quantity $E_{\boldsymbol{S}}[B]$ is only well-defined when spin polarization occurs. Therefore, below we focus on the effect of $E_{\boldsymbol{S}}[B]$ on the fully spin-polarized state.

3.3 Skyrmion phase

It is now straightforward to derive the condition for nonzero chirality to be favored. The free energy in Eq.(3.19) gives the threshold for nucleating chiral spin textures in

the ground state:

$$\Delta M \geq 2Je/\hbar c. \tag{3.20}$$

As a reminder, $\Delta M = M_+ - M_-$, $M_\pm = M(\mu \pm h)$ in one particular valley. Below, without loss of generality, we focus on K valley. In our particle-hole-symmetric Dirac model, the total orbital magnetization of all electrons in valley K takes a simple form[189]:

$$M_K(\mu) = \begin{cases} \frac{eD}{2\pi\hbar}, & \mu > D \\ \frac{e\mu}{2\pi\hbar}, & -D < \mu < D \\ -\frac{eD}{2\pi\hbar}, & \mu < -D \end{cases}, \tag{3.21}$$

taking opposite values in valleys K and K'. This dependence, with M being constant in each band, is a unique property of our Dirac band. A more general model would yield M that depends on doping in each band.

For a fully polarized state at a carrier density n, $M_+ = \frac{eD}{2\pi\hbar}$ whereas M_- depends on density. To calculate M_- we first calculate chemical potential using $\mu + h = \sqrt{D^2 + (\frac{4\pi n}{2m})^2}$ which gives:

$$\mu = \sqrt{D^2 + (2\pi n/m)^2} - U_0 n/2 \sim D - U_0 n/2 \tag{3.22}$$

where we have ignored $O(n^2)$ terms since we are interested in the low density regime. Plugging this into Eq.(3.21) we find

$$M_- = M(\mu - h) = (D - U_0 n)\, e/2\pi\hbar \tag{3.23}$$

As a result, $\Delta M = eU_0 n/(2\pi\hbar)$. Plugging this into Eq.(3.20) and using $J = \frac{\xi^2 h^2}{2U_0}$, we find a transition from a fully polarized state to chiral spin state occurs at $\frac{eU_0 n}{2\pi\hbar} \geq \frac{\xi^2 U_0 n^2 e}{4\hbar}$ which gives

$$n\xi^2 \leq \frac{2}{\pi} \tag{3.24}$$

Since our mean-field analysis works for ξ exceeding the Fermi wavelength λ_F, the condition in Eq.(3.24) is marginally met. The threshold Eq.(3.24) can be further

softened in multilayer graphene (such as tilayer, quadlayer, or pentalayer) because ΔM is proportional to the valley Chern number, which for N-layer graphene can take values that scale with the number of layers, $C = N/2$. As a result, the threshold softens to $n\xi^2 \leq \frac{2}{\pi}C$.

To show that the chiral phase is readily accessible we estimate the required size of ξ using realistic parameters. In BBG system of interest, the carrier density n_c at the onset of Stoner transition can be estimated from Eq.(3.16). For interaction strength $U_0 = 5 \times 10^3$meV nm^2, a band mass $m = 0.03m_e$ and a typical high value [201, 150, 35, 202, 203] $D = 100$meV, it predicts Stoner instability at $n_c \sim 3 \times 10^{11}$ cm^{-2}. Eq.(3.24) then predicts that to nucleate skyrmions the interaction radius must satisfy $\xi \lesssim 20$nm, a realistic value comparable to the Fermi wavelength.

A phase diagram describing the competition between the orders described above is shown in Fig.3-1. The transition line from uniformly polarized phase to skyrmion phase is given by Eq.(3.24). We note that, compared to the transition line between the uniformly polarized phase and unpolarized phase, the transition line between skyrmion phase and unpolarized phase is pushed slightly into the unpolarized phase. This is because when skyrmion condenses, the energy contribution from pseudo magnetic field Eq.(3.19) is always negative and tends to stabilize ordered state. This phase boundary is a first-order phase transition because the translation symmetry and the spin $SU(2)$ symmetry are simultaneously broken on this line.

We note that the condition for skyrmion instability Eq.(3.24) can be softened in Dirac bands with larger valley Chern numbers, since ΔM is proportional to the total Hall conductivity in the lower band. Large valley Chern numbers can be achieved in graphene multilayers, such as trilayer, quadlayer, or pentalayer. Another appealing system is moiré graphene, where valley-Chern minibands [162] give rise to a doping-dependent orbital magnetization, potentially leading to a skyrmion instability triggered by spin polarization onset.

The proliferation of skyrmions through the mechanism discussed above can lead to two possible ground states—skyrmion crystal and skyrmion liquid, arising when zero-point or thermal fluctuations are weak and strong, respectively. These phases

have properties similar to those of the vortex lattice and vortex liquid phases in superconductors [71, 51, 70, 16]. Which of the two states wins in the true ground state is an interesting topic for future work.

These two phases can be readily distinguished by transport measurements. In the presence of a valley polarization, which is ubiquitous in BBG and moire graphene systems, we expect quantized topological Hall effect in both states in the absence of an applied magnetic field [65, 60]. When time-reversal is not spontaneously broken (no valley polarization), a quantized topological valley Hall effect will occur, since the time-reversal requires skyrmions in valley K and K' to have opposite chiralities. On the other hand, the longitudinal transport will be very different in the two phases—vanishing for skyrmion crystal and nonzero for skyrmion liquid, dual to that of superconducting vortex crystals and liquids.

3.4 Spin-dependent pseudo magnetic field

In this section we substantiate the physical picture of a spin-dependent gauge field described above by a microscopic derivation. In essence, spin of an electron moving through a spin texture is rotated in spin space. This spin rotation effect, arising due to an electron spin being locked to the local spin quantization axis and tracking it along the electron trajectory, is described by a spin-dependent geometric phase. This adiabatic regime in which the geometric phase picture applies occurs when the Stoner spin gap is large compared to $\hbar v/\ell$, where ℓ is the characteristic spatial lengthscale of the spin texture modulation and v is Fermi velocity.

Here we derive this result step by step starting from a microscopic Hamiltonian, Eq.(3.2) of the main text, finding that a spin texture gives rise to an effective gauge field whose flux density is associated with the spin chirality. In our analysis below, without loss of generality, we focus on spins in valley K and suppress the valley label. A spin texture is described by a position-dependent $\boldsymbol{S}(r)$. Our plan is to carry out an $SU(2)$ spin rotation to bring all the local spin polarization to the same orientation and, in this way, generate a Hamiltonian that features a spin-dependent

pseudo-gauge-field term.

We start with a one-electron Hamiltonian in valley K, writing it in position space:

$$H(r) = \begin{pmatrix} D & \frac{(p_1 - ip_2)^2}{2m} \\ \frac{(p_1+ip_2)^2}{2m} & -D \end{pmatrix} 1_S - h1_L \boldsymbol{S}(r) \cdot \boldsymbol{\sigma} \tag{3.25}$$

where 1_S and 1_L are respectively the identity matrix in spin and sublattice subspace. In the first term, $p_{1,2} = -i\partial_{1,2}$. The second term represents the effect of a position-dependent spin polarization arising after a Hubbard-Stratonovich transformation, see Eq.(3.5) of the main text. Next, we perform a position-dependent $SU(2)$ similarity transformation $T(r)$ on the Hamiltonian, such that it rotates all spins to the $+z$ direction:

$$T^\dagger(r)(\boldsymbol{S}(r) \cdot \boldsymbol{\sigma})T(r) = \sigma_3 \tag{3.26}$$

After the spin rotation, the Hamiltonian becomes

$$\begin{aligned} \tilde{H}(r) &= T^\dagger(r)H(r)T(r) \\ &= \begin{pmatrix} D & \frac{(\Pi_1 - i\Pi_2)^2}{2m} \\ \frac{(\Pi_1+i\Pi_2)^2}{2m} & -D \end{pmatrix} 1_S - h1_L\sigma_3 \end{aligned} \tag{3.27}$$

where

$$\begin{aligned} \Pi_\mu &= -iT^\dagger(r)\partial_\mu T(r) = p_\mu + A_\mu, \\ A_\mu &= -iT^\dagger(r)\left[\partial_\mu, T(r)\right], \quad \mu = 1, 2 \end{aligned}$$

Here $A_{1,2}$ are 2×2 matrices representing an $SU(2)$ gauge field, and the square brackets represent commutators. The quantities A_μ can be expressed in terms of Pauli matrices:

$$A_\mu = \sum_{i=1,2,3} a_{\mu,i}\sigma_i \tag{3.28}$$

In the adiabatic regime, where all spins track the spin-up or the spin-down states in rotated basis, the off-diagonal components $a_{\mu,1}$ and $a_{\mu,2}$ only contribute at a sublead-

ing order. We therefore keep only the diagonal σ_3 components in spin, finding

$$\Pi_\mu = p_\mu + a_\mu \sigma_3. \tag{3.29}$$

where from now on a_μ will be used as a shorthand for $a_{\mu,3}$. This result indicates that the spin-up and spin-down electrons, which describe the majority and minority spin in the original basis, see a $U(1)$ gauge field of opposite signs (here spin-up and spin-down refers to states in a rotated basis). After some algebra[136], one finds

$$a_\mu = \frac{1}{2}(1 - \cos\theta)\partial_\mu \phi \tag{3.30}$$

where θ and ϕ are the spherical polar and azimuthal angles measured with respect to the z axis introduced in Eq.(3.26). The pseudo magnetic field B is then given by $B(\boldsymbol{x}) = \epsilon_{\mu\nu}\partial_\nu a_\mu = \nabla_x \times \boldsymbol{a}$. The result in Eq.(3.30) indicates that the geometric phase picked up by an electron moving in the pseudo magnetic field $B(\boldsymbol{x})$ is equal to $1/2$ of the solid angle swept by the spin quantization axis, which is the result used in main text, Eq.(3.2).

3.5 Valley-dependent orbital magnetization in graphene bilayer

To gain more insight into the physics of the orbital magnetization, Eq.(3.21) of the main text, here we rederive this known result[189] by a method that does not explicitly use Berry curvature. Our plan is to calculate the orbital magnetization in an individual graphene valley using thermodynamic relation:

$$M_K = -\frac{\partial \Xi_K}{\partial B}, \tag{3.31}$$

where Ξ_K is the thermodynamic potential of electrons in this valley, defined as

$$\Xi_K = \sum_\alpha (\epsilon_\alpha - \mu) f(\epsilon_\alpha), \quad f(\epsilon) = \frac{1}{e^{\beta(\epsilon-\mu)}+1} \tag{3.32}$$

where ϵ_α are the Landau level energies in the particle and hole bands, labeled by $\alpha = \{\pm, n\}$.

In order to obtain the magnetization at $B = 0$ we first calculate the Landau level energies ϵ_α and, by using the Euler-Maclaurin summation formula, extract the part of the sum over α in Eq.(3.32) which is linear in B at small B. As we will see, the contribution linear in B is equal to that originating from the anomalous Landau levels reduced by a factor of two, as discussed below. We will end this section by discussing the general character of this result and its relation to the spectral flow.

The Landau level energies can be derived directly from the BBG Hamiltonian[110, 109]. For illustration, here we do it for a simplified form of the Hamiltonian involving no trigonal warping terms:

$$H_K(p) = \begin{pmatrix} D + \frac{p^2}{2m_0} + \frac{p^2}{2m_a} & -\frac{(p_1 - ip_2)^2}{2m} \\ -\frac{(p_1+ip_2)^2}{2m} & -D - \frac{p^2}{2m_0} + \frac{p^2}{2m_a} \end{pmatrix} \tag{3.33}$$

Magnetic field can be incorporated in the Hamiltonian through the substitution $\boldsymbol{p} \to \boldsymbol{p} - \frac{e}{c}\boldsymbol{a}$. We will first carry out the analysis ignoring the terms $p^2/2m_0$ and $p^2/2m_a$. This is justified because these two terms are subleading for a realistic BBG band[110]. For the same reason we ignore the trigonal warping term (not shown in Eq.(3.33)). To illustrate the generality of our results, we will subsequently present the analysis for the full Hamiltonian in Eq.(3.33), finding that the quadratic terms $p^2/2m_0$ and $p^2/2m_a$ do not affect the result.

Next we consider the Landau levels formed in the presence of a B field, at first excluding the quadratic terms in the diagonal elements. As is well known, in each valley — K or K' — the Hamiltonian in Eq.(3.33), with the quadratic terms excluded, in the presence of a magnetic field generates three groups of Landau levels: (i) a pair of anomalous Landau levels at the edges of the hole band for valley K and particle

band for valley K', and (ii) two sequences of Landau levels in the particle and hole bands that are related by particle-hole symmetry. The energies of these Landau levels in valley K can be written as [89]

$$\epsilon_{\pm,n} = \epsilon_{\pm}(x_n) = \pm\sqrt{x_n^2 - \frac{1}{4}\hbar^2\omega_c^2 + D^2}, \quad n \geq 2,$$
$$\epsilon_{0,1} = -D, \quad x_n = \hbar\omega_c\left(n - \frac{1}{2}\right), \tag{3.34}$$

where $\omega_c = eB/m$ is the cyclotron frequency. For valley K' similar expressions arise, however the anomalous Landau levels are positioned at the particle band edge, $\epsilon_{0,1} = D$.

Accordingly, the thermodynamic potential Ξ_K in the presence of a B field is a sum of three contributions

$$\Xi_K = \Xi_+ + \Xi_- + \Xi_{01}, \tag{3.35}$$

where

$$\Xi_\pm = \frac{eB}{h}\sum_n(\epsilon_{\pm,n} - \mu)f(\epsilon_{\pm,n}), \tag{3.36}$$

$$\Xi_{01} = \frac{2eB}{h}(-D - \mu)f(-D), \tag{3.37}$$

with eB/h representing the numbers of electrons in each Landau level per unit area.

Magnetization is given by the linear ($O(B)$) term in $\Xi_K(B)$. The $O(B)$ contribution from the anomalous levels in each valley is already clearly written in Eq.(3.37). To calculate the $O(B)$ contribution from $\Xi_\pm$ we use the Euler-Maclaurin formula which approximates a sum by an integral. For the contribution of the particle band we have

$$\Xi_+ = \frac{eB}{h}\left[\frac{1}{\hbar\omega_c}\int_{x_{n=2}}^{\infty} dx(\epsilon(x) - \mu)f(\epsilon(x)) \right. \tag{3.38}$$
$$\left. + \frac{1}{2}(\epsilon\left(x_{n=2}\right) - \mu)f\left(\epsilon(x_{n=2})\right)\right] + O(B^2),$$

where $x_{n=2} = \frac{3}{2}\hbar\omega_c$, see Eq.(3.34). Here we have used $\epsilon(\infty)f(\infty) = 0$. Working out

the integral gives

$$\Xi_+ = -\frac{eB}{h}(D-\mu)f(D) + O(B^2). \tag{3.39}$$

Similarly, the $O(B)$ contribution of the lower-band Landau levels is given by

$$\Xi_- = -\frac{eB}{h}(-D-\mu)f(-D) + O(B^2). \tag{3.40}$$

After plugging Eqs. (3.37), (3.39) and (3.40) into Eqs. (3.31) and (3.35), we arrive at

$$M_K(\mu) = \begin{cases} \frac{2eD}{2\pi\hbar}, & \mu > D \\ \frac{e(\mu+D)}{2\pi\hbar}, & -D < \mu < D \\ 0, & \mu < -D \end{cases} . \tag{3.41}$$

We note that this dependence differs by a constant shift by $\Delta M_K = \frac{eD}{2\pi\hbar}$ from the result in Eq.(3.21) of the main text that was inferred from the general expression for orbital magnetization obtained in Ref.[189]. This constant shift arises from the way the contribution of the deep-lying levels is cut off, which is different from the conventional way[189]. However, this difference is immaterial because the deep-lying states, due to their dubious valley character and identical occupancies for opposite spins, are not expected to affect physical observables.

Indeed, at the bottom of the graphene band the carrier states cannot be unambiguously identified with the K and K' valleys. Therefore the ambiguity arising from the cutoff is a matter of convention rather than a physical effect. Furthermore, the quantity that matters for the physics of interest is the difference of the contributions from the spin-up and spin-down bands, $\Delta M = M_{K,\uparrow} - M_{K,\downarrow}$. The bands for opposite spins are filled equally at the bottom, such that the contributions of the deep-lying states to $M_{K,\uparrow}$ and $M_{K,\downarrow}$ cancel each other.

The meaning of the resulting dependence $M_K(\mu)$, in which M_K is constant when the Fermi level lies within one of the bands, can be understood in terms of a spectral flow induced by a variation of B. Namely, the role of the Landau levels moving up and down is merely to cancel half of the contribution to magnetization M_K of

the anomalous Landau levels in the corresponding bands. As a result, there is no μ dependence when the Fermi level lies outside the gap. In that each anomalous level contributes a half of the 'nominal value' of a single Landau level. This contribution comes with a plus sign or a minus sign depending on whether an anomalous Landau level is present for the band and valley in question. The resulting dependence of orbital magnetization is identical for the K and K' valleys up to a sign reversal, $M_K(\mu) = -M_{K'}(\mu)$.

This analysis can be applied to a realistic model of biased Bernal bilayer graphene, where the band Hamiltonian takes a more complicated form[110]. Here we show that adding the two quadratic terms given in Eq.(3.33), that were neglected temporarily, does not alter the result for $M_K(\mu)$.

The term $p^2/2m_a$ is an identity matrix in the sublattice variables. As a result, it merely shifts the energy eigenvalues without affecting the electron wavefunction that determines the orbital magnetization. Therefore, this term only affect the diamagnetic susceptibility but does not affect the magnetization at $B = 0$. Indeed, adding it in Eq.(3.38) yields an $O(B^2)$ contribution to the themodynamic potential, changing somewhat the diamagnetic susceptibility but not changing $M_K(\mu)$.

The term $p^2/2m_0$ has a σ_3 sublattice structure; therefore, this term does affect the wavefunctions. However, this term alone does not break the particle-hole symmetry. Also, this term does not affect the energy of the lowest Landau level in the particle band. As a result, the two conditions necessary for the reasoning above [from Eq.(3.35) to Eq.(3.40)] — the particle-hole symmetry and the two anomalous Landau levels — remain valid. Therefore, the result for magnetization remains unchanged.

3.6 Summary for Chapter 3

In conclusion, we have demonstrated that the chiral interaction — an emergent spin-orbital coupling — exists in Stoner magnetism in bands with Berry curvature. This interaction couples the spin chirality density to orbital magnetization while preserving the SU(2) spin rotation symmetry. One significant implication of this chiral interac-

tion is the emergence of a skyrmion ground state. Our study predicts that such a skyrmion phase can occur in multilayer graphene systems at low carrier densities. The new mechanism we propose for generating skyrmions provides electrical tunability, as the orbital magnetization can be tuned directly by gate voltages. This discovery holds great potential for advancing our understanding of fundamental physics and developing practical applications.

Chapter 4

Chiral spin-wave edge modes in Stoner magnets

4.1 Introduction

The material of this Chapter is largely based on Ref.[41]. As discussed in Sec.1.4.4, Stoner ferromagnetism is a correlated electron order ubiquitous in topological materials of current interest, including moiré graphene[3, 21, 22, 204, 184, 146], and nontwisted graphene bilayers and trilayers [201, 150, 35, 202, 203]. Yet, the fundamental properties of this state, especially those governed by Berry curvature in k space, are presently poorly understood. Here we predict that this state hosts chiral spin excitations. These excitations are confined to system edges and domain boundaries between different valley-polarized regions, propagating along them in a manner resembling Quantum Hall (QH) edge states, as illustrated in Fig.4-1. The microscopic origin of this behavior is the geometric phase of carrier spins tracking magnetization along carrier trajectories. Carrier spin rotation by a position-dependent magnetization generates a Berry phase in direct space that serves as a spin-dependent magnetic vector potential that couples to the orbital dynamics of carriers (see Eqs.(4.4),(4.5)) [136, 53, 125, 65]. The chiral edge behavior arises due to the coupling between this geometric magnetic field and orbital magnetization due to Berry curvature in k space. The geometric character of this interaction ensures robust chiral edge physics even in

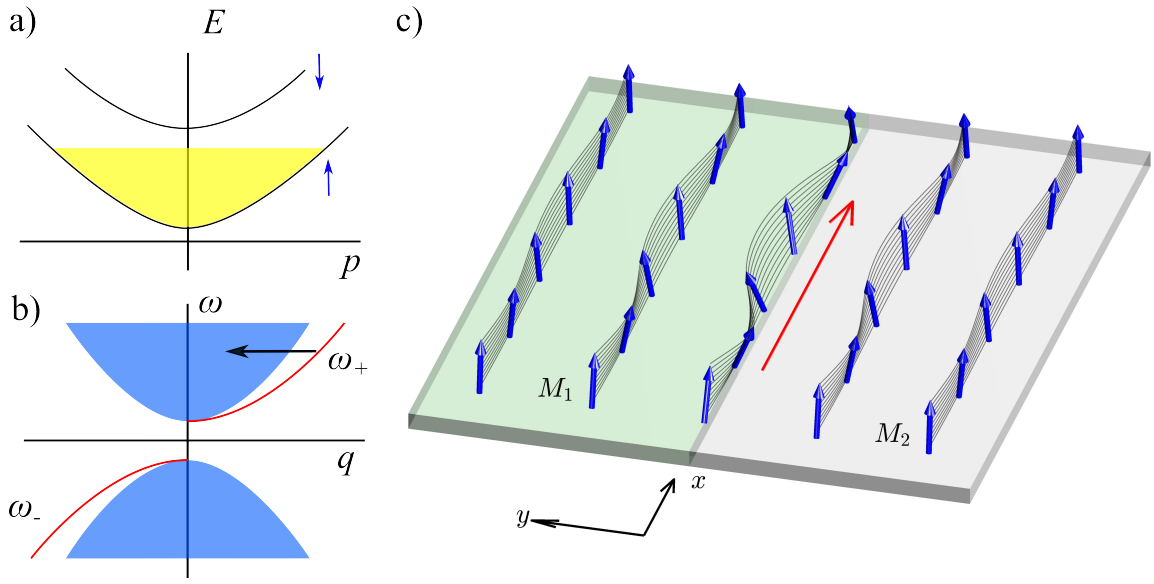

Figure 4-1: (a) Schematic band structure of a fully spin-polarized Stoner phase in a valley-polarized graphene bilayer or trilayer band. Only the valley populated by carriers is shown. (b) The spin-wave edge mode dispersion obtained for a step in orbital magnetization $M_1 \neq M_2$ induced by a gate, Eq.(4.12). The mode (red) is positioned outside the bulk magnon continuum (blue). The group velocity $v_g = d\omega/dq$ of a constant sign indicates the chiral character of the mode. The edge-to-bulk scattering (black arrow) is blocked by the energy and momentum conservation. (c) Schematic of the spatial dependence of the edge mode. The chiral mode is confined to the step and propagates along it without backscattering.

"vanilla" spin-polarized Fermi seas such as those seen in Refs.[201, 150, 35, 202, 203].

The band magnetism of carriers exhibiting orbital magnetization is a broad framework applicable to a diverse range of systems. This includes, in particular, the QH ferromagnets [59, 133, 1, 192] and correlated excitonic phases in QH bilayers [163, 45, 46, 96, 50]. Orbital magnetization in these systems exists due to Landau levels rather than the k-space Berry curvature and in QH bilayers the layer index plays the role of spin in our analysis. Here we focus on chiral edges in spin-polarized metals and, afterwards, comment on possible extensions to the QH systems.

In graphene multilayers [201, 150, 35, 202, 203], the predicted chiral edge behavior is sensitive to valley polarization. In a valley- and spin-polarized phase (identified as a quarter metal in Refs.[201, 150, 35, 202, 203]), the band orbital magnetization exhibits opposite signs in valleys K and K'. As a result, the chirality (i.e., the propagation

direction) of edge modes flips upon reversing the valley imbalance.

A very different behavior is expected in a valley-unpolarized but spin-polarized phase (half-metal in the nomenclature of Refs.[201, 150, 35, 202, 203]). In this case, the two valleys host Stoner metals with the band orbital magnetization of opposite signs. In this phase, the edges will host pairs of counter-propagating chiral edge modes, one for each valley. These two modes together respect the orbital time reversal symmetry, unbroken in the half-metal phase, i.e. the system is non-chiral.

The exceptional cleanness of graphene multilayers makes them an appealing system to probe this behavior. Spin lifetimes as long as 6 ns measurered in large bilayer graphene (BLG) systems by a nonlocal Hanle effect at 20 K [66] are explained by residual magnetic disorder [87, 88]. In contrast, recently, it was demonstrated that electrons isolated from edge disorder by gate confinement and trapped in gate-defined quantum dots acquire ultralong spin lifetimes, reaching values of 200 μs [10] and 50 ms [54] when measured in an applied magnetic field by pulsed-gate spectroscopy. Therefore, probing spin excitations in gate-defined electron puddles presents a distinct advantage. Yet, spin lifetimes measured in large BLG systems [66] also lie in a suitable range. Spin lifetimes can be further increased by applying nonquantizing magnetic fields that, apart from a constant offset, have little impact on the chiral spin-wave dispersion (see Eq.(4.17)).

In a metallic state the chiral mode at the edge can, in principle, decay by scattering into the 2D spin-one particle-hole continuum and spin waves. The former process is blocked by energy conservation since the spin-one continuum is gapped at small momenta [see Fig. 4-2 (a)]. The latter process, as shown by the black arrow in Fig.4-1 (b), is blocked by the energy and momentum conservation for a smooth edge but can be viable for a rough edge. However, as discussed in Sec.4.3, in the long-wavelength limit the edge modes have vanishing overlaps with the edge disorder potential, a property that protects the modes from edge-to-bulk scattering.

The chiral edge behavior in a Stoner metal phase discussed here is distinct from that predicted for magnetic phases with a nontrivial magnon band topology [115, 103, 36, 55, 111, 156, 157]. In these systems, chiral edge excitations lie above the first

magnon band and are therefore gapped. To the contrary, the chiral modes described here arise at the boundary of a uniformly spin-polarized Stoner Fermi sea—a metallic compressible state with a nontopological bulk magnon band. The edge excitations are gapless (in the absence of an externally applied magnetic field, see below) and have dispersion positioned beneath that of bulk spin waves (in our case these are nothing but the gapless magnons of a Heisenberg ferromagnet). Accordingly, here chiral modes arise in the absence of microscopic spin-dependent interactions such as Dzyaloshinskii-Moriya interaction (DMI) or dipolar interaction (as in Refs.[115, 103, 36, 55, 111] and Refs.[156, 157], respectively). Instead, they originate from an interplay between the exchange interaction and orbital magnetization in bands with Berry curvature and broken time reversal symmetry. Our spin waves act analogously to the chiral edge plasmons predicted for such bands [161], yet they transport spin rather than charge and arise from a very different mechanism.

4.2 Edge mode dispersion

Collective spin dynamics, both bulk and edge, are readily analyzed in the long-wavelength limit, at frequencies below the Stoner continuum [see Fig. 4-2 (a)]:

$$\Delta = U n_s > \omega(q), \tag{4.1}$$

where Δ is the Stoner gap, U is the exchange interaction, n_s is spin-polarized carrier density and $\omega(q)$ is mode dispersion. We employ an effective action for spin variables obtained by integrating out fermion orbital degrees of freedom. In that, we assume the electron velocity is large compared to that of spin-waves, $v_F \gg v_g = d\omega/dk$. As found below, the long-wavelength spin-wave dispersion is quadratic, $\omega(k) \sim k^2$, a behavior that confirms the separation of time scales for the orbital and spin degrees of freedom and justifies our analysis. The effective action for spin variables takes the

form [see e.g. [123, 52]]

$$A = \int dt d^2r \left(i n_s S_0 \langle \eta(\boldsymbol{r},t)|\partial_t|\eta(\boldsymbol{r},t)\rangle - \mathcal{H}[\boldsymbol{n}] \right), \tag{4.2}$$

where the first term is the Wess-Zumino-Witten action, hereafter referred to as $A_{\rm WZW}$, representing the single-spin Berry phase accumulated through time evolution. The second term is the Hamiltonian of a spin-polarized state discussed below. The quantity $|\eta(\boldsymbol{r},t)\rangle$ represents a coherent spin state in (2+1)D space-time. Here $n_s = n_\uparrow - n_\downarrow$ is the density of spin-imbalanced carriers, the factor $n_s S_0$ is the spin density, where $S_0 = \hbar/2$. In what follows spin polarization is described by a unit vector

$$\boldsymbol{n}(\boldsymbol{r},t) = \langle \eta(\boldsymbol{r},t)|\boldsymbol{\sigma}|\eta(\boldsymbol{r},t)\rangle.$$

The term $\mathcal{H}[\boldsymbol{n}]$ in Eq.(4.2) is the effective spin Hamiltonian. Symmetry arguments and microscopic analysis predict [40] the long-wavelength Hamiltonian

$$\mathcal{H}[\boldsymbol{n}] = n_s \left[\frac{J}{2} (\partial_\mu \boldsymbol{n})^2 - M(r) B(\boldsymbol{r},t) - \boldsymbol{h}_0 \cdot \boldsymbol{n} \right]. \tag{4.3}$$

Here J is spin stiffness, the second term is an interaction between the band orbital magnetization and the geometric magnetic field, the last term is the Zeeman energy per carrier, with the g-factor and Bohr magneton absorbed in the external magnetic field $\boldsymbol{h}_0$.

As indicated above, the interaction $-MB$ originates from a geometric Berry phase, arising due to electron spins tracking magnetization along electron trajectories. Spin rotation generates a Berry phase in position space defined by a spin-dependent magnetic vector potential [136]

$$a_\mu = \frac{\hbar c}{2e} (1 - \cos\theta)\, \partial_\mu \phi, \quad \mu = x, y. \tag{4.4}$$

Here θ and ϕ are the polar and azimuthal angles measured with respect to the spin polarization axis in the ground state. The sign of a_μ is chosen to describe the Berry

phase accrued by the majority-spin carriers. For the minority-spin carriers the vector potential is of the opposite sign and is described by $-a_\mu$, giving a Berry phase of the opposite sign. The geometric magnetic field is simply the curl of a_μ. In terms of $\boldsymbol{n}$, it reads:

$$B(\boldsymbol{r},t) = \nabla \times \boldsymbol{a} = \frac{\phi_0}{4\pi}\boldsymbol{n}\cdot(\partial_x\boldsymbol{n}\times\partial_y\boldsymbol{n}), \tag{4.5}$$

where $\phi_0 = hc/e$ is the flux quantum. This physics was first discussed in the early literature on high T_c superconductivity[12, 183, 148, 72] and later in the literature on noncollinear magnetic systems [136, 53, 65, 125]. Importantly, unlike static spin textures in the latter systems, our spin-wave dynamics generate a time-dependent vector potential, Eq.(4.4). This yields a geometric electric field [125, 8]

$$E_\mu = -\partial a_\mu/c\partial t - \nabla a_0 = \frac{\hbar}{2e}\boldsymbol{n}\cdot(\partial_t\boldsymbol{n}\times\partial_\mu\boldsymbol{n}), \tag{4.6}$$

which can enable electrical detection of the spin waves.

The quantity $M(r)$ in the second term in Eq.(4.3) describes the orbital magnetization per carrier in a spin-imbalanced band arising due to Berry curvature in k space. It is given by a sum of contributions of the filled states in the spin-valley-polarized Fermi sea. For a partially spin-polarized Fermi sea the contributions to M from the majority-spin and minority-spin carriers are of opposite signs, giving $M = M_\uparrow - M_\downarrow$. The opposite signs originate from the opposite signs of a_μ for the spin-up and spin-down carriers discussed beneath Eq.(4.4). These opposite sign contributions cancel in a spin-unpolarized state but lead to $M \neq 0$ in a fully or partially spin-polarized state. The position dependence $M(r)$ reflects spatially varying spin or valley imbalance arising, e.g., due to gating.

The geometric fields a_μ, B and $\boldsymbol{E}_\mu$ are derived in the adiabatic regime when an electron spin tracks spin texture along the electron's trajectory. The adiabatic regime occurs when the spin texture is sufficiently long-wavelength such that the Stoner spin gap $\Delta = Un_s$ is much greater than $\hbar v_F q$, where q is the characteristic spin-wave wavenumber and U is the exchange interaction (see Eq.(4.1)).

The Hamiltonian, Eq.(4.3), features different phases depending on the M and

J values [40]. If $M > 2J$ and h_0 is small enough, the uniformly polarized state is predicted to become unstable towards twisting, giving rise to a skyrmion texture with a nonzero chiral density B. Here, we consider excitations in a uniformly polarized state

$$\boldsymbol{n}(r,t) = \boldsymbol{n}_0 + \delta\boldsymbol{n}(r,t), \quad \delta\boldsymbol{n} \perp \boldsymbol{n}_0, \tag{4.7}$$

with $\boldsymbol{n}_0 \parallel \boldsymbol{h}_0$, occurring for not too large M values.

The spin wave dispersion can be obtained from the canonical equations of motion found from the saddle-point condition $\delta A/\delta\boldsymbol{n} = 0$, with A given in Eq.(4.2). Indeed, the variation of the Wess-Zumino-Witten term A_{WZW} [the first term in Eq.(4.2)] can be found by noting that this term equals to $n_s S_0$ times the solid angle swept by $\boldsymbol{n}$. As a result, its variation can be expressed as

$$\delta A_{\mathrm{WZW}} = n_s S_0 \int dt d^2r (\delta\boldsymbol{n} \times \partial_t \boldsymbol{n}) \cdot \boldsymbol{n}, \tag{4.8}$$

The variation of the action in Eq.(4.2) gives $\delta A = (n_s S_0 \partial_t \boldsymbol{n} \times \boldsymbol{n} - \delta\mathcal{H}/\delta\boldsymbol{n}) \cdot \delta\boldsymbol{n}$, giving equations of motion:

$$n_s S_0 \partial_t \boldsymbol{n}(r) = \boldsymbol{h}(r) \times \boldsymbol{n}(r), \quad \boldsymbol{h} = -\frac{\partial\mathcal{H}}{\partial\boldsymbol{n}} + \partial_\mu \frac{\partial\mathcal{H}}{\partial\partial_\mu\boldsymbol{n}}. \tag{4.9}$$

Linearizing about a uniformly polarized state yields coupled linear equations for $\delta\boldsymbol{n}$ components, which are identical to those found for a nonchiral problem,

$$S_0 \partial_t \delta\boldsymbol{n}(r,t) = \boldsymbol{h}_0 \times \delta\boldsymbol{n}(r,t) + J\partial_\mu^2 \delta\boldsymbol{n}(r,t) \times \boldsymbol{n}_0. \tag{4.10}$$

Plane wave solutions to this equation yield a simple isotropic and non-chiral spin-wave dispersion

$$\omega_\pm(q) = \pm(h_0 + Jq^2)/S_0, \tag{4.11}$$

with values approaching $\pm h_0/S_0$ in the limit $q \to 0$, universally and independent of the exchange interaction, as required by the Larmor theorem.

For a spatially uniform M, the $-MB$ term is a topological invariant. Therefore,

a local twist of spin does not change the $\mathcal{H}$ value. As a result, this interaction neither affects the energy nor impacts the spin waves. A spatially varying M, to the contrary, has a profound effect on spin waves. In particular, system boundaries and interfaces between regions in which M takes different values support chiral spin-wave modes reminiscent of the QH edge states. To illustrate this behavior we consider a step

$$M(y) = \begin{cases} M_1, & y > 0 \\ M_2, & y < 0. \end{cases} \tag{4.12}$$

In this case, after linearization, Eq.(4.7), we find

$$\boldsymbol{h} = n_s \left[J\partial_\mu^2 \delta\boldsymbol{n} - \partial_y M(y)(\boldsymbol{n}_0 \times \partial_x \delta\boldsymbol{n}) + \boldsymbol{h}_0 \right]. \tag{4.13}$$

Other terms vanish at first order in $\delta\boldsymbol{n}$. As a result, the linearized equations of motion become

$$S_0 \partial_t \delta\boldsymbol{n} = \boldsymbol{h}_0 \times \delta\boldsymbol{n} + J\partial_\mu^2 \delta\boldsymbol{n} \times \boldsymbol{n}_0 + m\delta(y)(\boldsymbol{n}_0 \times \partial_x \delta\boldsymbol{n}) \times \boldsymbol{n}_0,$$

where $m = M_2 - M_1$ is the difference between M on two sides of the edge. These equations are solved by writing $\delta\boldsymbol{n}(x, y)$ as a superposition of complex-valued helical components:

$$\delta\boldsymbol{n}(r,t) = \begin{pmatrix} \delta n_x(r,t) \\ \delta n_y(r,t) \end{pmatrix} = \sum_q e^{iqx} \left[e^{-i\omega_+ t} \psi_{q,+}(y) \begin{pmatrix} 1 \\ i \end{pmatrix} + e^{-i\omega_- t} \psi_{q,-}(y) \begin{pmatrix} 1 \\ -i \end{pmatrix} \right],$$

where we carried out the Fourier transform in time and the translation-invariant x direction. Plugging this ansatz into the equations of motion for $\delta\boldsymbol{n}(r,t)$, we obtain two decoupled 1D problems for a quantum particle in a delta-function potential, separately for each helicity:

$$S_0 \omega_\pm \psi(y) = \pm \left[h_0 + J(q^2 - \partial_y^2) \right] \psi - mq\delta(y)\psi(y), \tag{4.14}$$

where $\psi(y)$ is a shorthand for $\psi_{q,\pm}(y)$. These equations support bound states which

are edge spin waves for the helical polarization of a plus (minus) sign for mq of a positive (negative) sign, respectively.

Indeed, the bound state is described by an exponential solution for both helicities:

$$\psi_{q,\pm}(y) = u_q e^{-\lambda_q |y|}, \quad \lambda_q > 0, \tag{4.15}$$

where the condition $\lambda_q > 0$ is required for the mode to be normalizable. The value of λ_q and the dispersion are determined by the condition

$$0 = \pm 2J\lambda_q \delta(y) - mq\delta(y), \tag{4.16}$$

which gives $\lambda_q = \pm\frac{mq}{2J}$. Therefore, the right-helicity mode ψ^q_+ exists only for $mq > 0$, whereas the left-helicity mode ψ^q_- exists only for $mq < 0$.

$$\omega_\pm(q) = \pm\frac{1}{S_0}\left[h_0 + \left(J - \frac{m^2}{4J}\right)q^2\right] \tag{4.17}$$

The resulting dispersion is illustrated in Fig.4-1 (b) for $m > 0$. The group velocity $v_g = d\omega/dq$ is of the same sign for both helicities, as expected for a chiral edge mode. At $q = 0$, the frequency value agrees with the Zeeman frequency for a single spin, as required by Larmor's theorem. At this point λ_q vanishes, which signals that the mode ceases to be confined to the edge and transforms into a uniformly precessing state.

Notably, the discrete chiral mode, Eq.(4.17), appears in a robust manner regardless of magnetization values in the two halfplanes and the step size $m = M_1 - M_2$. At M_1 approaching M_2 the chiral mode, while remaining discrete, approaches the bulk magnon continuum and merges with it at $M_1 = M_2$. Another interesting aspect of the dispersion in Eq.(4.17) is that the group velocity reverses when m exceeds $2J$, upon which the mode propagation direction is reversed, with the left-moving excitations becoming right-moving and vice versa. In this regime the frequencies $\omega_\pm(q)$ reverse their signs when the wavenumber reaches a certain critical value, $q = q_* = \sqrt{4Jh_0/(4J^2 - m^2)}$. Frequency sign reversal signals an instability towards a

spatial modulation at the edge with spatial periodicity $2\pi/q_*$. Notably, this instability can occur before skyrmions are nucleated in the bulk. This happens, in particular, when M_1 and M_2 are of opposite signs. In this case, the condition for skyrmion nucleation in the bulk, $2J < |M_{1,2}|$, is more stringent than that for the instability at the edge, $2J < |M_1 - M_2|$.

Next, we consider polarization of chiral modes. As we found above, the modes of both helicities, ψ_+ and ψ_-, propagate in the same direction. This gives rise to an interesting space-time picture that combines propagation with velocity v_g and precession about $\boldsymbol{h}_0$. Indeed, a narrow wavepacket u_q centered at $q \approx q_0$ evolves as

$$\begin{aligned} \delta\boldsymbol{n}(r,t) &= \sum_{q>0} \phi_q^+(r,t) \begin{pmatrix} 1 \\ i \end{pmatrix} + \sum_{q<0} \phi_q^-(r,t) \begin{pmatrix} 1 \\ -i \end{pmatrix} \\ &\sim e^{-\lambda_{q_0}|y|} u(x - v_g t) \begin{pmatrix} \cos\left[\omega_0 t - q_0 x + \theta_0\right] \\ \sin\left[\omega_0 t - q_0 x + \theta_0\right] \end{pmatrix}. \end{aligned} \tag{4.18}$$

Here, $\phi_q^\pm(r,t) = e^{-i\omega_\pm(q)t + iqx - \lambda_q|y|} u_q$. The quantity $u(x)$ is the Fourier transform of u_q, $\omega_0 = \omega_+(q_0)$, v_g is the group velocity $d\omega/dq$ at $q = q_0$, θ_0 is a free parameter. This describes spin precession and 1D propagation, as illustrated in Fig. 4-1 (c).

Lastly, we discuss the relation between the analysis above and the collective spin excitations in QH ferromagnets. The seminal prediction of skyrmions in QH ferromagnets by Sondhi et al.[160] relies on the notion of an excess charge induced on a chiral spin texture, $\delta\rho(r) = \frac{1}{c}\sigma_{xy} B(r)$, a value that follows from the topological pumping argument [173, 132] with σ_{xy} the Hall conductivity of a filled Landau level and B the quantity in Eq.(4.5). This gives a contribution to the energy

$$\delta E = \int d^2 r V_g \delta\rho(r), \tag{4.19}$$

where V_g is the gate voltage. Since $B(r) = \frac{\phi_0}{4\pi} \boldsymbol{n} \cdot \partial_1 \boldsymbol{n} \times \partial_2 \boldsymbol{n}$, the quantity in Eq.(4.19) is identical in form to our $-MB$ interaction (the second term in Eq.(4.3)). Furthermore, it is straightforward to link the prefactor with the orbital magnetization of a fully

filled Landau level

$$M = \frac{1}{c} V_g \sigma_{xy}. \tag{4.20}$$

This relation follows from the thermodynamic relation $dM/d\mu = dn/dB_{\rm ext}$ and the Streda formula $dn/dB_{\rm ext} = \frac{\sigma_{xy}}{ce}$. Having reproduced the $-MB$ interaction in the QH framework, we are led to conclude that the chiral spin waves derived above must also occur in QH ferromagnets. While a detailed analysis should be deferred to future work, we expect that these modes differ in two distinct ways from various chiral charge and spin edge modes that have been widely investigated in QH systems [9, 106, 175, 73, 81, 198, 86, 145, 85]First, their dispersion at small k will be quadratic rather than linear. Second, rather than being tightly confined to the edge on a magnetic length scale, these modes will feature a wider profile extending far into the bulk. The weak confinement may suppress scattering by edge disorder and boost the lifetimes for these modes.

Last, we envision that extending the pulsed gate spectroscopy of Refs. [10, 54] to probe the gate-confined electron puddles can allow to launch the chiral spin waves and detect them in a manner analogous to the time-domain detection of QH edge magnetoplasmons [7, 199, 47, 91]. Further, electron-spin resonance (ESR) measurements on such puddles by the technique recently used to probe ESR in graphene[158] can provide direct information of the chiral mode dispersion. Indeed, for a puddle of circumference L the mode dispersion in Eq.(4.17), will translate into sidebands of the ESR resonance with frequencies

$$\omega_n = \omega(q_n), \quad q_n = 2\pi n/L, \tag{4.21}$$

with integer n. Here $n = 0$ is the fundamental ESR frequency and $n = 1, 2, 3...$ describes a family of chiral mode excitations. The $\omega = \omega_n$ resonances will occur over a continuous background due to the 2D spin-wave continuum, Eq.(4.11). As an example, we consider a disk of circumference $L = 10\,\mu$m for which the minimal wavenumber is $q_1 = 2\pi/L$. Estimating the stiffness as the e-e interaction at the Fermi wavelength scale, $J \sim e^2/(\kappa\lambda_F)$, and plugging realistic parameter values, we

find the sideband frequency detuning of $\omega_1 - \omega_0 \approx 50$ MHz. This value is greater than $1/T_1$ found in Refs.[10, 54] and lies in a convenient spectral range for microwave measurements. We also note that, as discussed above, spin dynamics in our system is accompanied by a geometric electric field given in Eq.(4.6). The oscillating electric polarization induced by this field can be used for a direct electrical detection of the chiral spin-wave dynamics.

4.3 Edge mode damping

Here, we discuss the intrinsic mechanisms of the edge spin wave damping. We first consider the system ignoring edge roughness and then discuss the decay pathway that is enabled by the edge roughness. We argue that both mechanisms give damping that becomes negligible at long wavelengths and low frequencies.

First, we consider the Landau damping due to the 2D particle-hole continuum. In spin-polarized metals there are two different particle-hole continua: the spin-zero continuum and the spin-one continuum. The spin-zero particle-hole continuum spans wavenumbers $0 < k < 2k_F$ and extends in frequency down to $\omega = 0$. Spin waves cannot simply decay into these excitations owing to the spin U(1) symmetry that ensures spin conservation. Therefore, these excitations do not impact the spin-wave lifetime on a tree level. Scattering involving spin-zero continuum can only take place through higher-order processes in which a spin wave is scattered by a spin-zero excitation or emits it without decaying. However, such processes are suppressed by the phase space volume for the final states.

Another 2D particle-hole continuum nominally available for decay, which is not blocked by the spin conservation, is the spin-one continuum, in which an electron is excited from the spin-majority band to the spin-minority band. However, the spin-one excitations are fully gapped at small momenta [see Fig.4-2 (a)] and, as a result, this scattering pathway is absent for long-wavelength (low-frequency) spin waves. Moreover, for the fully spin-polarized phase, the spin-one excitation is fully gapped at all momenta, which fully protects the long-wavelength spin waves from the

edge-to-bulk scattering.

Next, we study the scattering from the spin wave edge mode to bulk spin waves by edge disorder, and show that the lifetime is ultra-long for long-wavelength edge modes. As a simple model, we consider a step in magnetization with a wiggly boundary, illustrated in Fig. 4-2 (b). We will describe spin waves by a problem linearized in a weak perturbation about the uniform state, as implemented in the main text [see Eq.(7) therein]. Using the right and left helicity representation [see Eq.(14) of the main text] and, without loss of generality, focusing on the ψ_+ mode, we arrive at an effective action

$$A = \int dt d^2 r \bar{\psi}_+ \left(i\partial_t - H \right) \psi_+, \tag{4.22}$$

where $H = h_0 - \frac{J}{2}(\partial_x^2 + \partial_y^2) + \epsilon_{jj'}\partial_j M(r)\partial_{j'}$, and $M(r)$ describes two domains with magnetization M_1 and M_2 [Fig.4-2 (b)]. The magnetization gradient $\partial_j M(r)$ is a delta function centered at the wiggly domain boundary. For conciseness, we suppressed factors such as n_s, S_0, etc.

A convenient way to carry out the analysis is to employ a coordinate change that transforms a modulated boundary into a straight one. This can be done by a conformal mapping defined by an analytic function in the halfplane $y > 0$ and an anti-analytic function in the halfplane $y < 0$ with values matching at $y = 0$. The most general function of this type is of the form

$$z' = x' + iy' = z + \sum_k g_k e^{ikx - |k||y|}. \tag{4.23}$$

Under such conformal mapping the Schroedinger operator in Eq.(4.22) preserves its form up to a change in coefficients, allowing to describe a wiggly edge as a straight edge with a perturbation in the metric localized in its vicinity. The simple transformation rule is a consequence of the conformal invariance of the 2D Laplacian and the chiral density terms in our Hamiltonian, Eq.(3) in the main text. Indeed, denoting the Jacobian of the mapping in Eq.(4.23) as $D(r) = (\partial x', \partial y')/(\partial x, \partial y)$, we find that

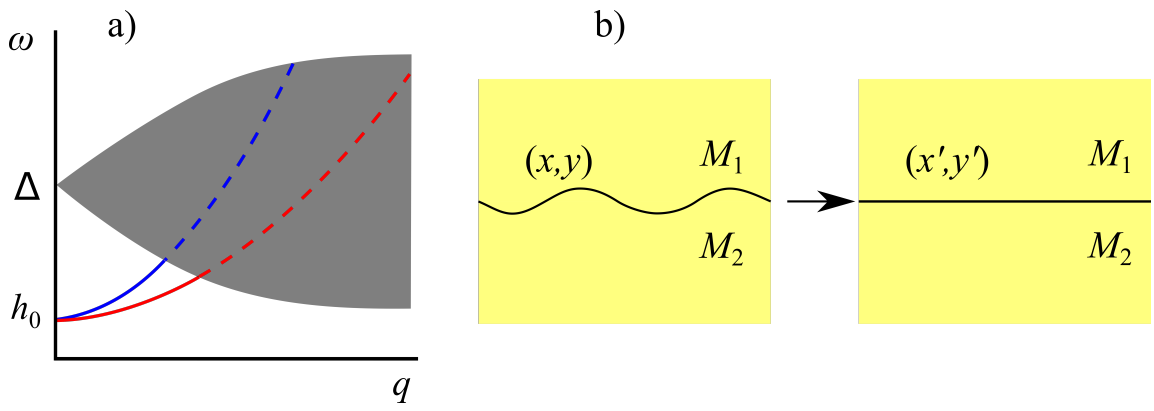

Figure 4-2: (a) Collective spin excitations in the bulk (blue line) and at the edge (red line) superimposed with the spin-one particle-hole continuum (gray region). Below the Stoner gap $\Delta = Un_s$ the collective modes are decoupled from the continuum and are therefore discrete. Upon entering the continuum they become Landau-damped (dashed lines). The spin-zero particle-hole continuum with wavenumbers $0 < k < 2k_F$ and frequencies extending down to $\omega = 0$ is not shown. This continuum is irrelevant for the damping of spin waves since one-excitation processes are blocked by U(1) spin conservation. (b) A wiggly step in magnetization $M(r)$ representing a rough edge. By a conformal mapping, Eq.(4.23), the problem with a wiggly edge is mapped onto the one with a straight edge and a fluctuating metric localized near the edge, Eq.(4.24). The edge-to-bulk scattering gives rise to a finite lifetime of the edge mode, $\tau = 1/\gamma$, where γ is given in Eq.(4.25).

under the conformal mapping the terms $i\partial_t - h_0$ in Eq.(4.22) are multiplied by D^{-1} whereas other terms remain unchanged.

The lifetime can now be calculated from the selfenergy for the Greens function

$$G = \frac{1}{\omega - H} = \frac{1}{\frac{\omega - h_0}{D(r)} + J(\partial_x^2 + \partial_y^2) - im\delta(y)\partial_x}$$

Expanding the Jacobian in powers of the modulation amplitude g_k gives $D^{-1}(r) = 1 + \delta p(r)$ where $\delta p(r) = \sum_k k g_k e^{ikx - |k||y|} + \text{c.c.} + O(g_k^2)$. We can now rewrite the Greens function in terms of the Hamiltonian for the straight edge, $H_0 = h_0 - J(\partial_x^2 + \partial_y^2) + im\delta(y)\partial_x$, and the perturbation $\delta p(r)$ localized near the edge:

$$G = \frac{1}{\omega - H_0 + (\omega - h_0)\delta p(r)}. \tag{4.24}$$

This expression is exact and can therefore be used to obtain the lifetime of the chiral edge mode in a closed form. Starting with a normalized wavefunction for the chiral mode derived above, $|\psi_+^0\rangle = e^{iqx}e^{-\lambda_q|y|}\lambda_q^{1/2}$, and calculating the lifetime from the selfenergy of G found at second order in $\delta p(r)$ we find the decay rate

$$\gamma = 2\pi \sum_{\boldsymbol{Q}} \mathrm{Im}G_0(\omega, \boldsymbol{Q}) |\left\langle e^{i\boldsymbol{Q}\boldsymbol{r}} | (\omega - h_0)\delta p(r) | \psi_+^0 \right\rangle|^2$$

where $G_0 = \frac{1}{\omega - H_0 + i0}$ and $\boldsymbol{Q}$ is the bulk magnon momentum. For a simple order of magnitude estimate it will be sufficient to approximate the spectral function $\mathrm{Im}G_0(\omega, \boldsymbol{Q})$ as that of the bulk magnon continuum, $\mathrm{Im}G_0(\omega, \boldsymbol{Q}) = \pi\delta(\omega - J\boldsymbol{Q}^2)$. Estimating this expression we find the decay rate that scales as

$$\gamma \sim \lambda_q(\omega - h_0)^2 \tag{4.25}$$

At small q these quantities scale as $\lambda_q \sim |q|$, $\omega - h_0 \sim q^2$ yielding the decay rate that vanishes in the long-wavelength limit as $\gamma \sim q^5$. The long lifetime arises as a combination of two effects. First, because of the Larmor theorem, in the small q limit the mode frequency for both bulk and edge is pinned to h_0 regardless of the

presence of an edge disorder. Second, because at small q the edge mode has a large penetration length into the bulk, $1/\lambda$. As a result, the mode weakly overlaps with the edge roughness, which suppresses the edge-to-bulk scattering.

4.4 Summary for Chapter 4

Chiral edge excitations represent a unique manifestation of chiral interactions in a metallic spin-polarized Fermi sea with a Berry band curvature. Despite occurring in a non-topological setting they are protected from backscattering by their chiral character. Correlated-electron phases that host chiral edge modes allowing excitations to propagate along system boundaries in a one-way manner are of keen interest for fundamental physics and are expected to harbor interesting applications. We describe the requirements for such modes to exist and argue that the chiral behavior and associated exotic physics are generic and readily accessible in state-of-the-art systems.

Chapter 5

Conclusions and Outlook

The central finding of this thesis is the existence of chiral interaction in Stoner magnets in the presence of k-space Berry curvature. This chiral interaction represents an emergent spin-orbital coupling that arises solely from the Stoner exchange interaction, independent of microscopic spin-orbital interactions. It couples the spin degrees of freedom in a Stoner magnet to the orbital magnetization of a spin-polarized Fermi sea endowed with Berry curvature while maintaining the SU(2) spin rotation symmetry.

In Chapter 2 we introduce, through a microscopic framework that uses Bernal bilayer graphene (BBG) band as a setting, a cascade of spin- and valley-polarized phases and their generalization—the momentum-polarized orders that occurs in the low carrier density regime of the system. This sets the stage for the discussion of the new physics enabled by the chiral interaction.

In Chapter 3, using BBG as an example, we present a fully microscopic derivation of the chiral interaction. Subsequently, we show that this interaction tends to stabilize skyrmion ground states which can occur in multilayer graphene systems at low carrier densities. What makes these skyrmions unique is that they are electrically tunable due to the direct tunability of the orbital magnetization through gate voltages. This feature opens up the possibility of controlling the skyrmion properties through all-electrical methods, which can have significant implications for future technological applications.

In Chapter 4, we explore another consequence of the chiral interaction: the chiral

edge excitations, which are spin waves that propagate unidirectionally along the edge or a step of orbital magnetization. These excitations exist in a uniformly polarized phase, in the absence of skyrmion order, or in the presence of skyrmions. The long-wavelength modes are long-lived because of small overlap with edge roughness, and are immune to backscattering due to their chiral character. The propagation direction for these excitation flips upon reversing the magnetization sign. As such, the chiral edge spin excitations represent a surprising phenomenon of fundamental interest that may have promising applications.

The work presented in this thesis poses a number of intriguing questions for future research:

1. **Chiral order in the absence of long-range spin order.**

   In 2D systems, at any finite temperature, thermal fluctuations suppress the long-range spin order. Since the chiral interaction only requires short-range correlations of spins, we expect it to be present even in the absence of a long-range spin order. Due to the softness of spin fluctuations in a system that possesses spin SU(2) symmetry, it is natural to expect the long-range spin order to be suppressed without the chirality order being destroyed. As a result, the skyrmion phase predicted in Chapter 3 will retain the chirality order when the positional order and the long-range spin order are suppressed by fluctuations. Such fluctuating spin textures with spin chirality of a definite sign will provide a realization of a "chiral spin liquid" occurring in a metallic state, a novel phase of matter with interesting properties. A similar question can be asked about the role of quantum fluctuations of spin and the properties of the ground state at zero temperature. While the role of thermal fluctuations can be analyzed by the standard methods of statistical mechanics, the quantum problem is considerably more subtle and calls for developing new ideas and new methods.

2. **The chiral interaction, edge excitations and skyrmions for other Stoner orders?**

   This thesis primarily focuses on the simplest case of 1/4 metal in which only one

spin/valley species is occupied. However, as discussed above, the chiral interaction can also be derived for partially polarized orders, such as spin-polarized half-metals, where both valleys are fully occupied and exhibit complete spin polarization. In such cases, what happens to the edge modes and what type of skyrmion order is favored? Since in a realistic setting the exchange interaction is predominantly intravalley due to the smallness of k_F compared to $K - K'$, we anticipate a simultaneous occurrence of several different edge modes with an interesting valley structure. We also expect skyrmion ground states with skyrmions in valley K and antiskyrmions in valley K', or vice versa. Realistic systems may involve a weak intervalley exchange interaction, which favors ferromagnetic alignment between the spins in the two valleys. Such an interaction would cause the skyrmions in valley K to repel the antiskyrmions in valley K', resulting in the formation of a checkerboard superlattice composed of alternating skyrmions and antiskyrmions.

3. **Analogs of the chiral interaction for superconducting orders and other many-body orders.**

   Specifically, does this type of interaction lead to new superconducting phases with the spin and orbital degrees of freedom coupled together? An appealing setting to probe this physics is the spin-triplet superconducting state in which the triplet spin of the condensate takes on the role of the spin-polarization discussed in this thesis. If the spin-triplet Cooper pairs form a texture with a nonvanishing chirality, this texture will act on condensate as a pseudo magnetic field, inducing vortices in the absence of an externally applied magnetic field. As a result, we envisage a spin-triplet superconducting system that develops a new ground state where chiral spin textures of Cooper pairs coexist with vortices. It is interesting to understand under what conditions such exotic states can occur in realistic systems, and explore questions such as topological properties of vortices and quasiparticles with different spin, charge and statistics.

Bibliography

[1] Jason Alicea and Matthew PA Fisher. Graphene integer quantum hall effect in the ferromagnetic and paramagnetic regimes. Physical Review B, 74(7):075422, 2006.

[2] Alexander Altland and Ben D Simons. Condensed matter field theory. Cambridge university press, 2010.

[3] Eva Y Andrei and Allan H MacDonald. Graphene bilayers with a twist. Nature materials, 19(12):1265–1275, 2020.

[4] Masato Aoki and Hiroshi Amawashi. Dependence of band structures on stacking and field in layered graphene. Solid State Communications, 142(3):123–127, 2007.

[5] Daniel Arovas. Lecture notes on condensed matter physics (a work in progress), chapter 4, 2010.

[6] Neil W Ashcroft and N David Mermin. Solid state physics. Cengage Learning, 2022.

[7] RC Ashoori, HL Stormer, LN Pfeiffer, KW Baldwin, and K West. Edge magnetoplasmons in the time domain. Physical Review B, 45(7):3894, 1992.

[8] Christian Back, Vincent Cros, Hubert Ebert, Karin Everschor-Sitte, Albert Fert, Markus Garst, Tianping Ma, Sergiy Mankovsky, TL Monchesky, Maxim Mostovoy, et al. The 2020 skyrmionics roadmap. Journal of Physics D: Applied Physics, 53(36):363001, 2020.

[9] NQ Balaban, U Meirav, Hadas Shtrikman, and V Umansky. Observation of the logarithmic dispersion of high-frequency edge excitations. Physical Review B, 55(20):R13397, 1997.

[10] L Banszerus, K Hecker, S Möller, E Icking, K Watanabe, T Taniguchi, C Volk, and C Stampfer. Spin relaxation in a single-electron graphene quantum dot. Nature Communications, 13(1):3637, 2022.

[11] Changhua Bao, Wei Yao, Eryin Wang, Chaoyu Chen, José Avila, Maria C Asensio, and Shuyun Zhou. Stacking-dependent electronic structure of trilayer graphene resolved by nanospot angle-resolved photoemission spectroscopy. Nano letters, 17(3):1564–1568, 2017.

[12] G Baskaran and Philip W Anderson. Gauge theory of high-temperature superconductors and strongly correlated fermi systems. Physical Review B, 37(1):580, 1988.

[13] Michael Victor Berry. Quantal phase factors accompanying adiabatic changes. Proceedings of the Royal Society of London. A. Mathematical and Physical Sciences, 392(1802):45–57, 1984.

[14] Benedikt Binz, Ashvin Vishwanath, and Vivek Aji. Theory of the helical spin crystal: a candidate for the partially ordered state of mnsi. Physical review letters, 96(20):207202, 2006.

[15] Rafi Bistritzer and Allan H MacDonald. Moiré bands in twisted double-layer graphene. Proceedings of the National Academy of Sciences, 108(30):12233–12237, 2011.

[16] Gianni Blatter, Mikhail V Feigel'man, Vadim B Geshkenbein, Anatoly I Larkin, and Valerii M Vinokur. Vortices in high-temperature superconductors. Reviews of modern physics, 66(4):1125, 1994.

[17] AN Bogdanov and UK Rößler. Chiral symmetry breaking in magnetic thin films and multilayers. Physical review letters, 87(3):037203, 2001.

[18] N Bohr. Collected works, volume i: Early works (1905–1911). North-Holland, Amsterdam, page 380, 1972.

[19] Thomas Bömerich, Lukas Heinen, and Achim Rosch. Skyrmion and tetarton lattices in twisted bilayer graphene. Physical Review B, 102(10):100408, 2020.

[20] DW Boukhvalov and MI Katsnelson. Tuning the gap in bilayer graphene using chemical functionalization: Density functional calculations. Physical Review B, 78(8):085413, 2008.

[21] Yuan Cao, Valla Fatemi, Ahmet Demir, Shiang Fang, Spencer L. Tomarken, Jason Y. Luo, Javier D. Sanchez-Yamagishi, Kenji Watanabe, Takashi Taniguchi, Efthimios Kaxiras, and et al. Correlated insulator behaviour at half-filling in magic-angle graphene superlattices. Nature, 556(7699):80–84, Mar 2018.

[22] Yuan Cao, Valla Fatemi, Shiang Fang, Kenji Watanabe, Takashi Taniguchi, Efthimios Kaxiras, and Pablo Jarillo-Herrero. Unconventional superconductivity in magic-angle graphene superlattices. Nature, 556(7699):43–50, Mar 2018.

[23] Yuan Cao, Daniel Rodan-Legrain, Jeong Min Park, Noah FQ Yuan, Kenji Watanabe, Takashi Taniguchi, Rafael M Fernandes, Liang Fu, and Pablo Jarillo-Herrero. Nematicity and competing orders in superconducting magic-angle graphene. science, 372(6539):264–271, 2021.

[24] Yuan Cao, Daniel Rodan-Legrain, Oriol Rubies-Bigorda, Jeong Min Park, Kenji Watanabe, Takashi Taniguchi, and Pablo Jarillo-Herrero. Tunable correlated states and spin-polarized phases in twisted bilayer–bilayer graphene. Nature, 583(7815):215–220, 2020.

[25] Eduardo V Castro, Kostya S Novoselov, Sergey V Morozov, NMR Peres, JMB Lopes Dos Santos, Johan Nilsson, F Guinea, AK Geim, and AH Castro Neto. Electronic properties of a biased graphene bilayer. Journal of Physics: Condensed Matter, 22(17):175503, 2010.

[26] Eduardo V Castro, KS Novoselov, SV Morozov, NMR Peres, JMB Lopes Dos Santos, Johan Nilsson, F Guinea, AK Geim, and AH Castro Neto. Biased bilayer graphene: semiconductor with a gap tunable by the electric field effect. Physical review letters, 99(21):216802, 2007.

[27] Eduardo V Castro, NMR Peres, T Stauber, and NAP Silva. Low-density ferromagnetism in biased bilayer graphene. Physical Review Letters, 100(18):186803, 2008.

[28] Ming-Che Chang and Qian Niu. Berry phase, hyperorbits, and the hofstadter spectrum: Semiclassical dynamics in magnetic bloch bands. Physical Review B, 53(11):7010, 1996.

[29] Youngjoon Choi, Jeannette Kemmer, Yang Peng, Alex Thomson, Harpreet Arora, Robert Polski, Yiran Zhang, Hechen Ren, Jason Alicea, Gil Refael, et al. Electronic correlations in twisted bilayer graphene near the magic angle. Nature physics, 15(11):1174–1180, 2019.

[30] Youngjoon Choi, Hyunjin Kim, Yang Peng, Alex Thomson, Cyprian Lewandowski, Robert Polski, Yiran Zhang, Harpreet Singh Arora, Kenji Watanabe, Takashi Taniguchi, et al. Correlation-driven topological phases in magic-angle twisted bilayer graphene. Nature, 589(7843):536–541, 2021.

[31] Yang-Zhi Chou, Fengcheng Wu, Jay D Sau, and Sankar Das Sarma. Acoustic-phonon-mediated superconductivity in bernal bilayer graphene. Physical Review B, 105(10):L100503, 2022.

[32] Piers Coleman. Introduction to many-body physics. Cambridge University Press, 2015.

[33] Vladimir Cvetkovic, Robert E. Throckmorton, and Oskar Vafek. Electronic multicriticality in bilayer graphene. Phys. Rev. B, 86:075467, Aug 2012.

[34] Vladimir Cvetkovic and Oskar Vafek. Topology and symmetry breaking in abc trilayer graphene. arXiv preprint arXiv:1210.4923, 2012.

[35] Sergio C de la Barrera, Samuel Aronson, Zhiren Zheng, Kenji Watanabe, Takashi Taniguchi, Qiong Ma, Pablo Jarillo-Herrero, and Raymond Ashoori.

Cascade of isospin phase transitions in bernal-stacked bilayer graphene at zero magnetic field. Nature Physics, 18(7):771–775, 2022.

[36] Sebastián A Díaz, Jelena Klinovaja, and Daniel Loss. Topological magnons and edge states in antiferromagnetic skyrmion crystals. Physical review letters, 122(18):187203, 2019.

[37] John F Dodaro, Steven A Kivelson, Yoni Schattner, Xiao-Qi Sun, and Chao Wang. Phases of a phenomenological model of twisted bilayer graphene. Physical Review B, 98(7):075154, 2018.

[38] Zhiyu Dong, Andrey V Chubukov, and Leonid Levitov. Spin-triplet superconductivity at the onset of isospin order in biased bilayer graphene. arXiv preprint arXiv:2205.13353, 2022.

[39] Zhiyu Dong, Margarita Davydova, Makinde Ogunnaike, and Leonid Levitov. Isospin ferromagnetism and momentum polarization in bilayer graphene. arXiv preprint arXiv:2110.15254, 2021.

[40] Zhiyu Dong and Leonid Levitov. Chiral stoner magnetism in dirac bands. arXiv preprint arXiv:2208.02051, 2022.

[41] Zhiyu Dong, Olumakinde Ogunnaike, and Leonid Levitov. Collective excitations in chiral stoner magnets. Phys. Rev. Lett., 130:206701, May 2023.

[42] JMB Lopes Dos Santos, NMR Peres, and AH Castro Neto. Continuum model of the twisted graphene bilayer. Physical Review B, 86(15):155449, 2012.

[43] Mildred S Dresselhaus and Gene Dresselhaus. Intercalation compounds of graphite. Advances in physics, 51(1):1–186, 2002.

[44] Igor Dzyaloshinsky. A thermodynamic theory of "weak" ferromagnetism of antiferromagnetics. Journal of physics and chemistry of solids, 4(4):241–255, 1958.

[45] JP Eisenstein. Exciton condensation in bilayer quantum hall systems. Annu. Rev. Condens. Matter Phys., 5(1):159–181, 2014.

[46] JP Eisenstein and AH MacDonald. Bose–einstein condensation of excitons in bilayer electron systems. Nature, 432(7018):691–694, 2004.

[47] G Ernst, RJ Haug, J Kuhl, KV von Klitzing, and K Eberl. Acoustic edge modes of the degenerate two-dimensional electron gas studied by time-resolved magnetotransport measurements. Physical review letters, 77(20):4245, 1996.

[48] Albert Fert, Nicolas Reyren, and Vincent Cros. Magnetic skyrmions: advances in physics and potential applications. Nature Reviews Materials, 2(7):1–15, 2017.

[49] HA Fertig, Luis Brey, R Côté, AH MacDonald, A Karlhede, and SL Sondhi. Hartree-fock theory of skyrmions in quantum hall ferromagnets. Physical Review B, 55(16):10671, 1997.

[50] ADK Finck, JP Eisenstein, LN Pfeiffer, and KW West. Quantum hall exciton condensation at full spin polarization. Physical Review Letters, 104(1):016801, 2010.

[51] Daniel S Fisher, Matthew PA Fisher, and David A Huse. Thermal fluctuations, quenched disorder, phase transitions, and transport in type-ii superconductors. Physical Review B, 43(1):130, 1991.

[52] Eduardo Fradkin. Field theories of condensed matter physics, 2013.

[53] Takashi Fujita, MBA Jalil, SG Tan, and Shuichi Murakami. Gauge fields in spintronics. Journal of applied physics, 110(12):17, 2011.

[54] Lisa Maria Gächter, Rebekka Garreis, Jonas Daniel Gerber, Max Josef Ruckriegel, Chuyao Tong, Benedikt Kratochwil, Folkert Kornelis de Vries, Annika Kurzmann, Kenji Watanabe, Takashi Taniguchi, et al. Single-shot spin readout in graphene quantum dots. PRX Quantum, 3(2):020343, 2022.

[55] Felipe Garcia-Sanchez, Pablo Borys, Arne Vansteenkiste, Joo-Von Kim, and Robert L Stamps. Nonreciprocal spin-wave channeling along textures driven by the dzyaloshinskii-moriya interaction. Physical Review B, 89(22):224408, 2014.

[56] Paola Gava, Michele Lazzeri, A Marco Saitta, and Francesco Mauri. Ab initio study of gap opening and screening effects in gated bilayer graphene. Physical Review B, 79(16):165431, 2009.

[57] Andre K Geim and Irina V Grigorieva. Van der waals heterostructures. Nature, 499(7459):419–425, 2013.

[58] Andre K Geim and Konstantin S Novoselov. The rise of graphene. Nature materials, 6(3):183–191, 2007.

[59] Steven M Girvin. Spin and isospin: exotic order in quantum hall ferromagnets. Phys. Today, 53(6):39–41, 2000.

[60] Börge Göbel, Alexander Mook, Jürgen Henk, and Ingrid Mertig. Unconventional topological hall effect in skyrmion crystals caused by the topology of the lattice. Physical Review B, 95(9):094413, 2017.

[61] F Guinea, AH Castro Neto, and NMR Peres. Interaction effects in single layer and multi-layer graphene. The European Physical Journal Special Topics, 148:117–125, 2007.

[62] F Guinea, AH Castro Neto, and NMR Peres. Electronic states and landau levels in graphene stacks. Physical Review B, 73(24):245426, 2006.

[63] F Guinea, AH Castro Neto, and NMR Peres. Electronic properties of stacks of graphene layers. Solid state communications, 143(1-2):116–122, 2007.

[64] Francisco Guinea and Niels R Walet. Electrostatic effects, band distortions, and superconductivity in twisted graphene bilayers. Proceedings of the National Academy of Sciences, 115(52):13174–13179, 2018.

[65] Keita Hamamoto, Motohiko Ezawa, and Naoto Nagaosa. Quantized topological hall effect in skyrmion crystal. Physical Review B, 92(11):115417, 2015.

[66] Wei Han, KM McCreary, K Pi, WH Wang, Yan Li, Hua Wen, JR Chen, and RK Kawakami. Spin transport and relaxation in graphene. Journal of Magnetism and Magnetic Materials, 324(4):369–381, 2012.

[67] Satoru Hayami, Ryo Ozawa, and Yukitoshi Motome. Effective bilinear-biquadratic model for noncoplanar ordering in itinerant magnets. Physical Review B, 95(22):224424, 2017.

[68] Stefan Heinze, Kirsten Von Bergmann, Matthias Menzel, Jens Brede, André Kubetzka, Roland Wiesendanger, Gustav Bihlmayer, and Stefan Blügel. Spontaneous atomic-scale magnetic skyrmion lattice in two dimensions. nature physics, 7(9):713–718, 2011.

[69] Lillian Hoddeson, Gordon Baym, and Michael Eckert. The development of the quantum-mechanical electron theory of metals: 1928—1933. Reviews of modern physics, 59(1):287, 1987.

[70] Jun Hu and Allan H MacDonald. Two-dimensional vortex lattice melting. Physical review letters, 71(3):432, 1993.

[71] BA Huberman and S Doniach. Melting of two-dimensional vortex lattices. Physical Review Letters, 43(13):950, 1979.

[72] LB Ioffe, V Kalmeyer, and PB Wiegmann. Hall coefficient of the doped mott insulator: A signature of parity violation. Physical Review B, 43(1):1219, 1991.

[73] SV Iordanski and A Kasbuba. Excitations in a quantum hall ferromagnet with strong coulomb interaction. Journal of Experimental and Theoretical Physics Letters, 75:348–353, 2002.

[74] Hiroki Isobe, Noah FQ Yuan, and Liang Fu. Unconventional superconductivity and density waves in twisted bilayer graphene. Physical Review X, 8(4):041041, 2018.

[75] Wanjun Jiang, Gong Chen, Kai Liu, Jiadong Zang, Suzanne GE Te Velthuis, and Axel Hoffmann. Skyrmions in magnetic multilayers. Physics Reports, 704:1–49, 2017.

[76] Yuhang Jiang, Xinyuan Lai, Kenji Watanabe, Takashi Taniguchi, Kristjan Haule, Jinhai Mao, and Eva Y Andrei. Charge order and broken rotational symmetry in magic-angle twisted bilayer graphene. Nature, 573(7772):91–95, 2019.

[77] Florian Jonietz, Sebastain Mühlbauer, Christian Pfleiderer, Andreas Neubauer, Wolfgang Münzer, Andreas Bauer, T Adams, Robert Georgii, Peter Böni, Rembert A Duine, et al. Spin transfer torques in mnsi at ultralow current densities. Science, 330(6011):1648–1651, 2010.

[78] Jeil Jung, Marco Polini, and Allan H MacDonald. Persistent current states in bilayer graphene. Physical Review B, 91(15):155423, 2015.

[79] N Kanazawa, Y Onose, T Arima, D Okuyama, K Ohoyama, S Wakimoto, K Kakurai, S Ishiwata, and Y Tokura. Large topological hall effect in a short-period helimagnet mnge. Physical review letters, 106(15):156603, 2011.

[80] Jian Kang and Oskar Vafek. Strong coupling phases of partially filled twisted bilayer graphene narrow bands. Physical review letters, 122(24):246401, 2019.

[81] A Karlhede, K Lejnell, and SL Sondhi. Dynamics of the compact, ferromagnetic $\nu = 1$ edge. Physical Review B, 60(23):15948, 1999.

[82] Mitsuo Kataoka and Osamu Nakanishi. Helical spin density wave due to antisymmetric exchange interaction. Journal of the Physical Society of Japan, 50(12):3888–3896, 1981.

[83] Alexander Kerelsky, Leo J McGilly, Dante M Kennes, Lede Xian, Matthew Yankowitz, Shaowen Chen, K Watanabe, T Taniguchi, James Hone, Cory Dean, et al. Maximized electron interactions at the magic angle in twisted bilayer graphene. Nature, 572(7767):95–100, 2019.

[84] Eslam Khalaf, Shubhayu Chatterjee, Nick Bultinck, Michael P Zaletel, and Ashvin Vishwanath. Charged skyrmions and topological origin of superconductivity in magic-angle graphene. Science advances, 7(19):eabf5299, 2021.

[85] Udit Khanna, Moshe Goldstein, and Yuval Gefen. Emergence of neutral modes in laughlin-like fractional quantum hall phases. Physical Review Letters, 129(14):146801, 2022.

[86] Maxim Kharitonov, Stefan Juergens, and Björn Trauzettel. Interplay of topology and interactions in quantum hall topological insulators: U (1) symmetry, tunable luttinger liquid, and interaction-induced phase transitions. Physical Review B, 94(3):035146, 2016.

[87] Denis Kochan, Martin Gmitra, and Jaroslav Fabian. Spin relaxation mechanism in graphene: resonant scattering by magnetic impurities. Physical review letters, 112(11):116602, 2014.

[88] Denis Kochan, Susanne Irmer, Martin Gmitra, and Jaroslav Fabian. Resonant scattering by magnetic impurities as a model for spin relaxation in bilayer graphene. Physical Review Letters, 115(19):196601, 2015.

[89] Mikito Koshino and Edward McCann. Parity and valley degeneracy in multilayer graphene. Physical Review B, 81(11):115315, 2010.

[90] Vladyslav Kozii, Hiroki Isobe, Jörn WF Venderbos, and Liang Fu. Nematic superconductivity stabilized by density wave fluctuations: Possible application to twisted bilayer graphene. Physical Review B, 99(14):144507, 2019.

[91] N Kumada, H Kamata, and T Fujisawa. Edge magnetoplasmon transport in gated and ungated quantum hall systems. Physical Review B, 84(4):045314, 2011.

[92] AB Kuzmenko, Iris Crassee, Dirk Van Der Marel, P Blake, and KS Novoselov. Determination of the gate-tunable band gap and tight-binding parameters in bilayer graphene using infrared spectroscopy. Physical Review B, 80(16):165406, 2009.

[93] Sylvain Latil and Luc Henrard. Charge carriers in few-layer graphene films. Physical Review Letters, 97(3):036803, 2006.

[94] Yongjin Lee, Shi Che, Jairo Velasco Jr, David Tran, Jacopo Baima, Francesco Mauri, Matteo Calandra, Marc Bockrath, and Chun Ning Lau. Gate tunable magnetism and giant magnetoresistance in abc-stacked few-layer graphene. arXiv preprint arXiv:1911.04450, 2019.

[95] AO Leonov and M Mostovoy. Multiply periodic states and isolated skyrmions in an anisotropic frustrated magnet. Nature communications, 6(1):8275, 2015.

[96] JIA Li, T Taniguchi, K Watanabe, J Hone, and CR Dean. Excitonic superfluid phase in double bilayer graphene. Nature Physics, 13(8):751–755, 2017.

[97] ZQ Li, EA Henriksen, Zhigang Jiang, Zhao Hao, Michael C Martin, P Kim, HL Stormer, and Dimitri N Basov. Band structure asymmetry of bilayer graphene revealed by infrared spectroscopy. Physical Review Letters, 102(3):037403, 2009.

[98] Yu-Ping Lin and Rahul M Nandkishore. Chiral twist on the high-t c phase diagram in moiré heterostructures. Physical Review B, 100(8):085136, 2019.

[99] Shang Liu, Eslam Khalaf, Jong Yeon Lee, and Ashvin Vishwanath. Nematic topological semimetal and insulator in magic-angle bilayer graphene at charge neutrality. Physical Review Research, 3(1):013033, 2021.

[100] Xiaomeng Liu, Gelareh Farahi, Cheng-Li Chiu, Zlatko Papic, Kenji Watanabe, Takashi Taniguchi, Michael P Zaletel, and Ali Yazdani. Visualizing broken symmetry and topological defects in a quantum hall ferromagnet. Science, 375(6578):321–326, 2022.

[101] Chun Hung Lui, Zhiqiang Li, Zheyuan Chen, Paul V Klimov, Louis E Brus, and Tony F Heinz. Imaging stacking order in few-layer graphene. Nano letters, 11(1):164–169, 2011.

[102] AH MacDonald, HA Fertig, and Luis Brey. Skyrmions without sigma models in quantum hall ferromagnets. Physical review letters, 76(12):2153, 1996.

[103] Kristian Mæland and Asle Sudbø. Quantum topological phase transitions in skyrmion crystals. arXiv preprint arXiv:2205.12965, 2022.

[104] Juan L Mañes, Francisco Guinea, and María AH Vozmediano. Existence and topological stability of fermi points in multilayered graphene. Physical Review B, 75(15):155424, 2007.

[105] AS Mayorov, DC Elias, Marcin Mucha-Kruczynski, RV Gorbachev, T Tudorovskiy, A Zhukov, SV Morozov, MI Katsnelson, VI Fal'ko, AK Geim, et al. Interaction-driven spectrum reconstruction in bilayer graphene. Science, 333(6044):860–863, 2011.

[106] Victoria Mazo, HA Fertig, and Efrat Shimshoni. Collective edge modes of a quantum hall ferromagnet in graphene. Physical Review B, 86(12):125404, 2012.

[107] Edward McCann. Asymmetry gap in the electronic band structure of bilayer graphene. Physical Review B, 74(16):161403, 2006.

[108] Edward McCann, David SL Abergel, and Vladimir I Fal'ko. The low energy electronic band structure of bilayer graphene. The European Physical Journal Special Topics, 148(1):91–103, 2007.

[109] Edward McCann and Vladimir I Fal'ko. Landau-level degeneracy and quantum hall effect in a graphite bilayer. Physical review letters, 96(8):086805, 2006.

[110] Edward McCann and Mikito Koshino. The electronic properties of bilayer graphene. Reports on Progress in Physics, 76(5):056503, apr 2013.

[111] Paul A McClarty. Topological magnons: A review. Annual Review of Condensed Matter Physics, 13:171–190, 2022.

[112] Eugene J Mele. Commensuration and interlayer coherence in twisted bilayer graphene. Physical Review B, 81(16):161405, 2010.

[113] Hongki Min, Giovanni Borghi, Marco Polini, and A. H. MacDonald. Pseudospin magnetism in graphene. Phys. Rev. B, 77:041407, Jan 2008.

[114] Hongki Min, Bhagawan Sahu, Sanjay K Banerjee, and AH MacDonald. Ab initio theory of gate induced gaps in graphene bilayers. Physical Review B, 75(15):155115, 2007.

[115] Alexander Mook, Jürgen Henk, and Ingrid Mertig. Edge states in topological magnon insulators. Physical Review B, 90(2):024412, 2014.

[116] E Suárez Morell, JD Correa, P Vargas, M Pacheco, and Z Barticevic. Flat bands in slightly twisted bilayer graphene: Tight-binding calculations. Physical Review B, 82(12):121407, 2010.

[117] Tôru Moriya. Anisotropic superexchange interaction and weak ferromagnetism. Physical review, 120(1):91, 1960.

[118] M Mucha-Kruczyński, DSL Abergel, E McCann, and VI Fal'Ko. On spectral properties of bilayer graphene: the effect of an sic substrate and infrared magneto-spectroscopy. Journal of Physics: Condensed Matter, 21(34):344206, 2009.

[119] M Mucha-Kruczyński, E McCann, and Vladimir I Fal'Ko. Electron–hole asymmetry and energy gaps in bilayer graphene. Semiconductor Science and Technology, 25(3):033001, 2010.

[120] M Mucha-Kruczyński, O Tsyplyatyev, A Grishin, Edward McCann, Vladimir I Fal'ko, Aaron Bostwick, and Eli Rotenberg. Characterization of graphene through anisotropy of constant-energy maps in angle-resolved photoemission. Physical Review B, 77(19):195403, 2008.

[121] Sebastian Mühlbauer, Benedikt Binz, F Jonietz, Christian Pfleiderer, Achim Rosch, Anja Neubauer, Robert Georgii, and Peter Böni. Skyrmion lattice in a chiral magnet. Science, 323(5916):915–919, 2009.

[122] N Nagaosa, XZ Yu, and Y Tokura. Gauge fields in real and momentum spaces in magnets: monopoles and skyrmions. Philosophical Transactions of the Royal Society A: Mathematical, Physical and Engineering Sciences, 370(1981):5806–5819, 2012.

[123] Naoto Nagaosa. Quantum field theory in condensed matter physics, 1999.

[124] Naoto Nagaosa. Emergent electromagnetism in condensed matter. Proceedings of the Japan Academy, Series B, 95(6):278–289, 2019.

[125] Naoto Nagaosa and Yoshinori Tokura. Emergent electromagnetism in solids. Physica Scripta, 2012(T146):014020, 2012.

[126] Naoto Nagaosa and Yoshinori Tokura. Topological properties and dynamics of magnetic skyrmions. Nature nanotechnology, 8(12):899–911, 2013.

[127] O Nakanishi, A Yanase, A Hasegawa, and M Kataoka. The origin of the helical spin density wave in mnsi. Solid State Communications, 35(12):995–998, 1980.

[128] Rahul Nandkishore and Leonid Levitov. Flavor symmetry and competing orders in bilayer graphene. arXiv preprint arXiv:1002.1966, 2010.

[129] AH Castro Neto, Francisco Guinea, Nuno MR Peres, Kostya S Novoselov, and Andre K Geim. The electronic properties of graphene. Reviews of modern physics, 81(1):109, 2009.

[130] A Neubauer, C Pfleiderer, B Binz, A Rosch, R Ritz, PG Niklowitz, and P Böni. Topological hall effect in the a phase of mnsi. Physical review letters, 102(18):186602, 2009.

[131] Johan Nilsson, AH Castro Neto, F Guinea, and NMR Peres. Electronic properties of bilayer and multilayer graphene. Physical Review B, 78(4):045405, 2008.

[132] Qian Niu and DJ Thouless. Quantised adiabatic charge transport in the presence of substrate disorder and many-body interaction. Journal of Physics A: Mathematical and General, 17(12):2453, 1984.

[133] Kentaro Nomura and Allan H MacDonald. Quantum hall ferromagnetism in graphene. Physical review letters, 96(25):256602, 2006.

[134] Kostya S Novoselov, Andre K Geim, Sergei V Morozov, De-eng Jiang, Yanshui Zhang, Sergey V Dubonos, Irina V Grigorieva, and Alexandr A Firsov. Electric field effect in atomically thin carbon films. science, 306(5696):666–669, 2004.

[135] Masayuki Ochi, Mikito Koshino, and Kazuhiko Kuroki. Possible correlated insulating states in magic-angle twisted bilayer graphene under strongly competing interactions. Physical Review B, 98(8):081102, 2018.

[136] Kenya Ohgushi, Shuichi Murakami, and Naoto Nagaosa. Spin anisotropy and quantum hall effect in the kagomé lattice: Chiral spin state based on a ferromagnet. Physical Review B, 62(10):R6065, 2000.

[137] Taisuke Ohta, Aaron Bostwick, Thomas Seyller, Karsten Horn, and Eli Rotenberg. Controlling the electronic structure of bilayer graphene. Science, 313(5789):951–954, 2006.

[138] Tsuyoshi Okubo, Sungki Chung, and Hikaru Kawamura. Multiple-q states and the skyrmion lattice of the triangular-lattice heisenberg antiferromagnet under magnetic fields. Physical review letters, 108(1):017206, 2012.

[139] Jeroen B Oostinga, Hubert B Heersche, Xinglan Liu, Alberto F Morpurgo, and Lieven MK Vandersypen. Gate-induced insulating state in bilayer graphene devices. Nature materials, 7(2):151–157, 2008.

[140] Bart Partoens and FM Peeters. From graphene to graphite: Electronic structure around the k point. Physical Review B, 74(7):075404, 2006.

[141] Andrew T Pierce, Yonglong Xie, Jeong Min Park, Eslam Khalaf, Seung Hwan Lee, Yuan Cao, Daniel E Parker, Patrick R Forrester, Shaowen Chen, Kenji Watanabe, et al. Unconventional sequence of correlated chern insulators in magic-angle twisted bilayer graphene. Nature Physics, 17(11):1210–1215, 2021.

[142] Aleksandr Michajlovič Polyakov. Gauge fields and strings. Taylor & Francis, 1987.

[143] Ulrich K Roessler, AN Bogdanov, and C Pfleiderer. Spontaneous skyrmion ground states in magnetic metals. Nature, 442(7104):797–801, 2006.

[144] Asaf Rozen, Jeong Min Park, Uri Zondiner, Yuan Cao, Daniel Rodan-Legrain, Takashi Taniguchi, Kenji Watanabe, Yuval Oreg, Ady Stern, Erez Berg, et al. Entropic evidence for a pomeranchuk effect in magic-angle graphene. Nature, 592(7853):214–219, 2021.

[145] Amartya Saha, Suman Jyoti De, Sumathi Rao, Yuval Gefen, and Ganpathy Murthy. Emergence of spin-active channels at a quantum hall interface. Physical Review B, 103(8):L081401, 2021.

[146] Yu Saito, Fangyuan Yang, Jingyuan Ge, Xiaoxue Liu, Takashi Taniguchi, Kenji Watanabe, JIA Li, Erez Berg, and Andrea F Young. Isospin pomeranchuk effect in twisted bilayer graphene. Nature, 592(7853):220–224, 2021.

[147] Jun John Sakurai and Eugene D Commins. Modern quantum mechanics, revised edition, 1995.

[148] HJ Schulz. Effective action for strongly correlated fermions from functional integrals. Physical review letters, 65(19):2462, 1990.

[149] Tomek Schulz, R Ritz, Andreas Bauer, Madhumita Halder, Martin Wagner, Chris Franz, Christian Pfleiderer, Karin Everschor, Markus Garst, and Achim Rosch. Emergent electrodynamics of skyrmions in a chiral magnet. Nature Physics, 8(4):301–304, 2012.

[150] Anna M Seiler, Fabian R Geisenhof, Felix Winterer, Kenji Watanabe, Takashi Taniguchi, Tianyi Xu, Fan Zhang, and R Thomas Weitz. Quantum cascade of correlated phases in trigonally warped bilayer graphene. Nature, 608(7922):298–302, 2022.

[151] Shinichiro Seki, XZ Yu, S Ishiwata, and Yoshinori Tokura. Observation of skyrmions in a multiferroic material. Science, 336(6078):198–201, 2012.

[152] Kangjun Seo, Valeri N Kotov, and Bruno Uchoa. Ferromagnetic mott state in twisted graphene bilayers at the magic angle. Physical review letters, 122(24):246402, 2019.

[153] M Serlin, CL Tschirhart, H Polshyn, Y Zhang, J Zhu, K Watanabe, T Taniguchi, L Balents, and AF Young. Intrinsic quantized anomalous hall effect in a moiré heterostructure. Science, 367(6480):900–903, 2020.

[154] Aaron L Sharpe, Eli J Fox, Arthur W Barnard, Joe Finney, Kenji Watanabe, Takashi Taniguchi, MA Kastner, and David Goldhaber-Gordon. Emergent ferromagnetism near three-quarters filling in twisted bilayer graphene. Science, 365(6453):605–608, 2019.

[155] Junren Shi, Giovanni Vignale, Di Xiao, and Qian Niu. Quantum theory of orbital magnetization and its generalization to interacting systems. Physical review letters, 99(19):197202, 2007.

[156] Ryuichi Shindou, Ryo Matsumoto, Shuichi Murakami, and Jun-ichiro Ohe. Topological chiral magnonic edge mode in a magnonic crystal. Physical Review B, 87(17):174427, 2013.

[157] Ryuichi Shindou, Jun-ichiro Ohe, Ryo Matsumoto, Shuichi Murakami, and Eiji Saitoh. Chiral spin-wave edge modes in dipolar magnetic thin films. Physical Review B, 87(17):174402, 2013.

[158] J Sichau, M Prada, T Anlauf, TJ Lyon, B Bosnjak, L Tiemann, and RH Blick. Resonance microwave measurements of an intrinsic spin-orbit coupling gap in graphene: A possible indication of a topological state. Physical Review Letters, 122(4):046403, 2019.

[159] John C Slater. Cohesion in monovalent metals. Physical Review, 35(5):509, 1930.

[160] Shivaji Lal Sondhi, A Karlhede, SA Kivelson, and EH Rezayi. Skyrmions and the crossover from the integer to fractional quantum hall effect at small zeeman energies. Physical Review B, 47(24):16419, 1993.

[161] Justin CW Song and Mark S Rudner. Chiral plasmons without magnetic field. Proceedings of the National Academy of Sciences, 113(17):4658–4663, 2016.

[162] Justin CW Song, Polnop Samutpraphoot, and Leonid S Levitov. Topological bloch bands in graphene superlattices. Proceedings of the National Academy of Sciences, 112(35):10879–10883, 2015.

[163] IB Spielman, JP Eisenstein, LN Pfeiffer, and KW West. Resonantly enhanced tunneling in a double layer quantum hall ferromagnet. Physical review letters, 84(25):5808, 2000.

[164] T Stauber, Eduardo V Castro, NAP Silva, and NMR Peres. First-order ferromagnetic phase transition in the low electronic density regime of a biased graphene bilayer. Journal of Physics: Condensed Matter, 20(33):335207, 2008.

[165] Edmund Clifton Stoner. Collective electron specific heat and spin paramagnetism in metals. Proceedings of the Royal Society of London. Series A-Mathematical and Physical Sciences, 154(883):656–678, 1936.

[166] Edmund Clifton Stoner. Collective electron ferromagnetism. Proceedings of the Royal Society of London. Series A. Mathematical and Physical Sciences, 165(922):372–414, 1938.

[167] Edmund Clifton Stoner. Collective electron ferromagnetism ii. energy and specific heat. Proceedings of the Royal Society of London. Series A. Mathematical and Physical Sciences, 169(938):339–371, 1939.

[168] P Streda. Theory of quantised hall conductivity in two dimensions. Journal of Physics C: Solid State Physics, 15(22):L717, 1982.

[169] Y Taguchi, Y Oohara, H Yoshizawa, N Nagaosa, and Y Tokura. Spin chirality, berry phase, and anomalous hall effect in a frustrated ferromagnet. Science, 291(5513):2573–2576, 2001.

[170] Y Taguchi, T Sasaki, S Awaji, Y Iwasa, T Tayama, T Sakakibara, S Iguchi, T Ito, and Y Tokura. Magnetic field induced sign reversal of the anomalous hall effect in a pyrochlore ferromagnet n d 2 m o 2 o 7: Evidence for a spin chirality mechanism. Physical review letters, 90(25):257202, 2003.

[171] Gen Tatara and Noriyuki Nakabayashi. Emergent spin electromagnetism induced by magnetization textures in the presence of spin-orbit interaction. Journal of Applied Physics, 115(17):172609, 2014.

[172] Timo Thonhauser, Davide Ceresoli, David Vanderbilt, and Raffaele Resta. Orbital magnetization in periodic insulators. Physical review letters, 95(13):137205, 2005.

[173] DJ Thouless. Quantization of particle transport. Physical Review B, 27(10):6083, 1983.

[174] Robert E. Throckmorton and S. Das Sarma. Quantum multicriticality in bilayer graphene with a tunable energy gap. Phys. Rev. B, 90:205407, Nov 2014.

[175] Pavel Tikhonov, Efrat Shimshoni, HA Fertig, and Ganpathy Murthy. Emergence of helical edge conduction in graphene at the $\nu = 0$ quantum hall state. Physical Review B, 93(11):115137, 2016.

[176] CL Tschirhart, M Serlin, H Polshyn, A Shragai, Z Xia, J Zhu, Y Zhang, K Watanabe, T Taniguchi, ME Huber, et al. Imaging orbital ferromagnetism in a moiré chern insulator. Science, 372(6548):1323–1327, 2021.

[177] H-J Van Leeuwen. Problemes de la théorie électronique du magnétisme. J. phys. radium, 2(12):361–377, 1921.

[178] JH Van Vleck. The theory of electric and magnetic susceptibilities, clarendon, 1932.

[179] JH Van Vleck. Quantum mechanics: the key to understanding magnetism. Nobel Lectures in Physics (1971–1980), pages 353–369, 1992.

[180] Jr Velasco, Lei Jing, Wenzhong Bao, Yongjin Lee, Philip Kratz, Vivek Aji, Marc Bockrath, CN Lau, Chandra Varma, Ryan Stillwell, et al. Transport spectroscopy of symmetry-broken insulating states in bilayer graphene. Nature nanotechnology, 7(3):156–160, 2012.

[181] Pierre Weiss. La variation du ferromagnétisme avec la température. Comptes Rendus, 143:1136–1139, 1906.

[182] Pierre Weiss. La constante du champ moléculaire. equation d'état magnétique et calorimétrie. Journal de Physique et le Radium, 1(5):163–175, 1930.

[183] PB Wiegmann. Superconductivity in strongly correlated electronic systems and confinement versus deconfinement phenomenon. Physical review letters, 60(9):821, 1988.

[184] Dillon Wong, Kevin P Nuckolls, Myungchul Oh, Biao Lian, Yonglong Xie, Sangjun Jeon, Kenji Watanabe, Takashi Taniguchi, B Andrei Bernevig, and Ali Yazdani. Cascade of electronic transitions in magic-angle twisted bilayer graphene. Nature, 582(7811):198–202, 2020.

[185] Fengcheng Wu and Sankar Das Sarma. Collective excitations of quantum anomalous hall ferromagnets in twisted bilayer graphene. Physical review letters, 124(4):046403, 2020.

[186] Fengcheng Wu and Sankar Das Sarma. Ferromagnetism and superconductivity in twisted double bilayer graphene. Physical Review B, 101(15):155149, 2020.

[187] Di Xiao, Ming-Che Chang, and Qian Niu. Berry phase effects on electronic properties. Reviews of modern physics, 82(3):1959, 2010.

[188] Di Xiao, Junren Shi, and Qian Niu. Berry phase correction to electron density of states in solids. Physical review letters, 95(13):137204, 2005.

[189] Di Xiao, Wang Yao, and Qian Niu. Valley-contrasting physics in graphene: magnetic moment and topological transport. Physical review letters, 99(23):236809, 2007.

[190] Ming Xie and Allan H MacDonald. Nature of the correlated insulator states in twisted bilayer graphene. Physical review letters, 124(9):097601, 2020.

[191] Cenke Xu and Leon Balents. Topological superconductivity in twisted multilayer graphene. Physical review letters, 121(8):087001, 2018.

[192] Kun Yang, S Das Sarma, and AH MacDonald. Collective modes and skyrmion excitations in graphene s u (4) quantum hall ferromagnets. Physical Review B, 74(7):075423, 2006.

[193] XZ Yu, Yoshinori Onose, Naoya Kanazawa, Joung Hwan Park, JH Han, Yoshio Matsui, Naoto Nagaosa, and Yoshinori Tokura. Real-space observation of a two-dimensional skyrmion crystal. Nature, 465(7300):901–904, 2010.

[194] J Zak. Berry's phase for energy bands in solids. Physical review letters, 62(23):2747, 1989.

[195] Jiadong Zang, Maxim Mostovoy, Jung Hoon Han, and Naoto Nagaosa. Dynamics of skyrmion crystals in metallic thin films. Physical review letters, 107(13):136804, 2011.

[196] Fan Zhang, Jeil Jung, Gregory A Fiete, Qian Niu, and Allan H MacDonald. Spontaneous quantum hall states in chirally stacked few-layer graphene systems. Physical review letters, 106(15):156801, 2011.

[197] LM Zhang, ZQ Li, Dimitri N Basov, MM Fogler, Zhao Hao, and Michael C Martin. Determination of the electronic structure of bilayer graphene from infrared spectroscopy. Physical Review B, 78(23):235408, 2008.

[198] Yuhui Zhang and Kun Yang. Edge spin excitations and reconstructions of integer quantum hall liquids. Physical Review B, 87(12):125140, 2013.

[199] NB Zhitenev, RJ Haug, K v Klitzing, and K Eberl. Time-resolved measurements of transport in edge channels. Physical review letters, 71(14):2292, 1993.

[200] H Zhou, H Polshyn, T Taniguchi, K Watanabe, and AF Young. Solids of quantum hall skyrmions in graphene. Nature Physics, 16(2):154–158, 2020.

[201] Haoxin Zhou, Ludwig Holleis, Yu Saito, Liam Cohen, William Huynh, Caitlin L. Patterson, Fangyuan Yang, Takashi Taniguchi, Kenji Watanabe, and Andrea F. Young. Isospin magnetism and spin-polarized superconductivity in bernal bilayer graphene. Science, 375(6582):774–778, 2022.

[202] Haoxin Zhou, Tian Xie, Areg Ghazaryan, Tobias Holder, James R Ehrets, Eric M Spanton, Takashi Taniguchi, Kenji Watanabe, Erez Berg, Maksym Serbyn, and Andrea F. Young. Half-and quarter-metals in rhombohedral trilayer graphene. Nature, 598(7881):429–433, 2021.

[203] Haoxin Zhou, Tian Xie, Takashi Taniguchi, Kenji Watanabe, and Andrea F Young. Superconductivity in rhombohedral trilayer graphene. Nature, 598(7881):434–438, 2021.

[204] Uri Zondiner, Asaf Rozen, Daniel Rodan-Legrain, Yuan Cao, Raquel Queiroz, Takashi Taniguchi, Kenji Watanabe, Yuval Oreg, Felix von Oppen, Ady Stern, et al. Cascade of phase transitions and dirac revivals in magic-angle graphene. Nature, 582(7811):203–208, 2020.